

Observational Analysis of Small-Scale Structures Across the Earth's Bow Shock

Rebecca Harvey

A DISSERTATION

**Submitted in partial fulfillment of the requirements
for the degree of Doctor of Philosophy
in
The Department of Space Science
to
The Graduate School
of
The University of Alabama in Huntsville**

June 2025

Approved by:

- Dr. Qiang Hu, Research Advisor/Committee Chair
- Dr. Gary Zank, Committee Member
- Dr. Linling Zhao, Committee Member
- Dr. Jakobus le Roux, Committee Member
- Dr. Laxman Adhikari, Committee Member
- Dr. Vladimir Florinski, Department Chair
- Dr. Rainer Steinwandt, College Dean
- Dr. Jon Hakkila, Graduate Dean

Abstract

Observational Analysis of Small-Scale Structures Across the Earth's Bow Shock

Rebecca Harvey

**A dissertation submitted in partial fulfillment of the requirements
for the degree of Doctor of Philosophy**

Space Science

**The University of Alabama in Huntsville
June 2025**

This work identifies and characterizes magnetic structures in the solar wind and magnetosheath across the Earth's bow shock. I investigate the differences between the properties of small-scale flux rope (SFR) structures immediately upstream and downstream of the bow shock by employing two data analysis methods: one based on wavelet transforms and the other based on the Grad-Shafranov (GS) detection and reconstruction techniques. 676 hours in the solar wind, and 1051 hours in the magnetosheath, of in situ magnetic field and plasma data from the Magnetospheric Multiscale (MMS) and Time History of Events and Macroscale Interactions during Substorms (THEMIS) missions were used to identify these coherent structures.

I investigate the difference between the properties of the magnetic structures in different near-Earth regions. The magnetic structures with varying degrees of Alfvénicity are characterized in a systematic manner as they move across boundaries in near-Earth space. I identified thousands of SFR event intervals in each region, and established an inventory of events with high magnetic helicity. I report the parameters associated with the SFRs such as scale size, duration, and magnetic helicity density, and a direct comparison of the statistical properties of the structures from these two

regions is performed. The GS-based method is extended to identify structures with significant remaining plasma flow aligned with the local magnetic field, and yielded a unique set of additional parameters that allowed us to evaluate the distributions of the Walén test slope, magnetic flux, and the orientation of the z -axes of the structures.

In general, it is found that the distributions of various parameters follow power laws. The SFR structures seem to be compressed in the magnetosheath, as compared with their counterparts in the solar wind. A significant rotation in the z -axis defining the orientation of the structures is also seen across the bow shock. The implications for the elongation of the SFRs in the magnetosheath along one spatial dimension are also discussed.

Acknowledgements

I would like to express my gratitude to my advisor, Qiang Hu. He has guided and supported me along my PhD journey. I would also like to thank my committee members: Drs. Gary Zank, Lingling Zhao, Jakobus le Roux, and Laxman Adhikari, for their effort in helping me successfully complete this work. Further more, I would also like to acknowledge the assistance and encouragement given to me by Yu Chen, who has graciously assisted me with the GS-based reconstruction code.

This work was funded by NASA Grants 80NSSC21K0003, 80NSSC21K1763, 80NSSC21K1319, and NSF Grant AGS-2229065. I acknowledge NASA contract NAS5-02099 and V. Angelopoulos for use of data from the THEMIS Mission. Specifically: K. H. Glassmeier, U. Auster and W. Baumjohann for the use of FGM data (Auster et al., 2008) provided under the lead of the Technical University of Braunschweig and with financial support through the German Ministry for Economy and Technology and the German Center for Aviation and Space (DLR) under contract 50 OC 0302, and C. W. Carlson and J. P. McFadden for use of ESA (McFadden et al., 2008) data. I thank the individuals who support the MMS mission, specifically that of the FIELDS team (Torbert et al., 2016) and the FPI team (Pollock et al., 2016), as well as those who make the data readily available. The data used in this study was retrieved from the NASA Science Data Center via the PySPEDAS software, which is open source and publicly available at <https://github.com/spedas/pyspedas> under an MIT license. I would like to gratefully acknowledge Wenli Mo and Savvas Raptis for their correspondence providing the MMS data set¹ classified in different magnetospheric regions Toy-Edens et al. (2024a).

¹<https://zenodo.org/records/11032322>

I would also like to acknowledge the people who have supported me in my personal (and also professional) endeavors. Words can't even describe how grateful I am for the unwavering support that partner Clayton has given me. I would not be where I am today without his dedication to being there for me. I would also like to say thank you to my friends and co-workers for helping me talk through coding issues, going to conferences together, and just making each day in the office entertaining.

I would like to dedicate this work to my two best work-from-home buddies, Dorrine and Konrad, who were supposed to be here but life had other plans. To my baby girl Dorrine: thank you for your many, loud suggestions and for also trying to help type some of this document. To Konrad: I wrote the bulk of this while waiting for updates about you, or while visiting you, or while thinking of you. Thanks for all the moral support, baby man.

Table of Contents

Abstract	ii
Acknowledgements	v
Table of Contents	ix
List of Figures	x
List of Tables	xiii
List of Symbols	xv
Epigraph	xvii
Organization	xviii
Chapter 1. Introduction	1
1.1 Space Environment	1
1.1.1 Interplanetary magnetic field and near-Earth solar wind	1
1.1.2 Bow shock	3
1.1.3 Magnetosheath	4
1.1.4 Magnetopause	5

1.1.5	Magnetosphere	7
1.2	Turbulence & coherent structures	7
1.2.1	Interplanetary flux ropes	8
1.2.2	Alfvénic structures	10
1.3	Objectives	12
Chapter 2.	Data sets and pre-processing	14
2.1	THEMIS data set	14
2.2	MMS data set	15
2.3	Data selection and pre-processing	21
Chapter 3.	Wavelet analysis as a single-spacecraft method	27
3.1	Wavelet transforms	27
3.2	MHD quantities	30
3.3	Algorithm for identification of magnetic structures	34
3.4	Event categorization	38
Chapter 4.	Grad-Shafranov reconstruction and automated identification algorithm	44
4.1	The Grad-Shafranov equation	44
4.1.1	Derivation of the original GS equation	44
4.1.2	Derivation of the extended GS equation	46

4.2	Automated GS-based detection of SFRs	53
4.3	2D reconstructions of cross-sections	60
4.4	Analysis results	63
4.5	Walén test and Alfvénicity	71
4.6	Flow velocities and orientation of SFRs	77
Chapter 5.	Combined analysis results	82
Chapter 6.	Coordinated analysis of simultaneous observations	88
Chapter 7.	Conclusions and Future Work	96
References	100
Appendix A:	Summary of observation intervals	109
Appendix B:	Flow chart of the GS-based automated detection algorithm	119
Appendix C:	Supplemental results	121

List of Figures

1.1	Diagram of the interplanetary magnetic field	2
1.2	Diagram of the Earth’s magnetopause and magnetic field lines.	6
1.3	Diagram of a magnetic cloud, with twisted magnetic field lines in a tube-like formation around a central axis (Feng et al., 2020).	9
1.4	Distributions of scale-size of SFRs from Helios 1 and 2 (Chen and Hu, 2020)	10
2.1	Configuration of instruments on a singular THEMIS probe	16
2.2	MMS FIELDS suite	19
2.3	MMS FPI instrument suite	19
2.4	Orbits for all observation periods	20
2.5	Time series data observed in the magnetosheath on 9 November 2019	23
2.6	Time series data observed in the magnetosheath during 19-20 June 2009	24
2.7	Time series data observed in the solar wind during 19-20 June 2009	25
3.1	Time and frequency resolutions of different transforms	30
3.2	Time series data and spectrograms of MHD quantities for 9 November 2019	35
3.3	Diagram of wavelet analysis identification algorithm via spectrograms of MHD quantities	37
3.4	Time series and spectrogram for 9 November 2019 with identified events overlaid	39
3.5	Reduced cross helicity and reduced residual energy for all events identified via wavelet analysis	43
4.1	Representation of a 2D cross-sectional view of a magnetic cloud .	55

4.2	2D reconstruction of a magnetic cloud using the GS-reconstruction algorithm	56
4.3	P'_t versus A' plot for 22:15:35-22:17:05 UT on 19 June 2009	58
4.4	GS-based event reconstruction for 9 November 2019	61
4.5	GS-based event reconstruction for 19 June 2009	62
4.6	GS-based event reconstruction for 15 November 2017	64
4.7	Distributions of the axial flux and poloidal flux per unit length	69
4.8	Histograms for the approximation to the helicity density per unit length	70
4.9	2D distributions of various parameters vs. $ A_m $ in the solar wind	72
4.10	2D distributions of various parameters vs. $ A_m $ in the magnetosheath	73
4.11	Plot of Walén slope for 9 November 2019 9:53:10 - 9:54:36 UT	74
4.12	Reduced cross helicity and reduced residual energy for all events identified via GS-based reconstruction algorithm	75
4.13	Histograms for proportionality constant $\alpha = \langle M_A \rangle^2$	76
4.14	Walén test slope vs. reduced cross helicity	78
4.15	Orbit plot of flow vectors associated with the SFRs	79
4.16	Distributions of the azimuthal and polar angles that define the z -axis of SFR structures	81
5.1	Histograms of duration for identified events	83
5.2	Histograms of scale size for identified events	84
5.3	Cumulative distribution function of scale sizes for the identified events	86
6.1	Orbits for coordinated observation intervals	89
6.2	Histogram of duration from coordinated analysis	93
6.3	Histogram of scale size from coordinated analysis	94

6.4	Histogram of poloidal magnetic flux per unit length from coordinated analysis	95
B.1	Flowchart of GS-reconstruction based automated detection algorithm	120
C.1	Histogram of average magnetic field for identified events	122
C.2	Histogram of velocity for identified events	123
C.3	Histogram of beta for identified events	124
C.4	Histogram of temperature for identified events	125

List of Tables

2.1	Data products from THEMIS and MMS	18
3.1	Summary table for identified events in the solar wind and magnetosheath via wavelet analysis as described in Section 3.3.	40
3.2	Statistical values for the physical quantities of structures identified with wavelet analysis	41
3.3	Summary table of events meeting certain MHD criteria for events identified via wavelet analysis in the magnetosheath and solar wind. .	42
4.1	Threshold conditions for GS algorithm	59
4.2	Summary table for identified events in the solar wind and magnetosheath via the GS-based reconstruction identification algorithm. .	65
4.3	Statistical values for the physical quantities of structures identified with GS-based analysis analysis	66
4.4	Statistical values for the physical quantities of SFR structures identified solely via the GS-based method	68
4.5	Events identified with the GS-based method meeting different Walén test slope criteria.	75
6.1	Summary table for events identified via wavelet analysis and the GS reconstruction algorithm during the simultaneous observation intervals.	90
6.2	Events meeting certain MHD quantity (top) and Walén test slope (bottom) criteria.	91
A.1	Periods of data across 1051 hours in the magnetosheath from THEMIS and MMS probes	110
A.2	Periods of data across 676 hours in the solar wind from THEMIS and MMS probes	115

A.3 Observations intervals across 260 hours of simultaneous measurements from THEMIS and MMS probes in the magnetosheath and solar wind.	118
--	-----

List of Symbols

Symbol	Description
A	magnetic flux function
A'	modified magnetic flux function
$P'_t(A')$	transverse pressure as a function of the modified magnetic flux function
R_E	Radius of the Earth, 6372 km
R_{diff}	point-wise difference residue between the two parts
R_{fit}	residue of the fitting function $P'_t(A')$
Φ_z	approximate axial magnetic flux
α	average Alfvén Mach number squared
ϕ	azimuthal angle between the GSE X -direction and the projection of the z -axis onto the XY -plane
σ_c	normalized cross helicity
σ_m	normalized magnetic helicity
σ_r	normalized residual energy
θ	polar angle between the SFR z -axis and the GSE Z -direction
w	Walén test slope
$ A_m $	poloidal magnetic flux per meter

Symbol	Description
AU	Astronomical unit: distance between the Earth and the sun, 1.4959×10^8 km
GS	Grad-Shafranov
GSE	Geocentric Solar Ecliptic coordinate system
IMF	Interplanetary magnetic field
MMS	Magnetospheric Multiscale mission
SFR	small-scale flux rope
THEMIS	Time History of Events and Macroscale Interactions during Substorms mission

*Ask me what I learned from all those years,
Ask me what I earned from all those tears,
Ask me why so many fade, but I'm still here*

- “Karma” by Taylor Swift (Midnights)

Organization

Chapter 1: Introduction This chapter presents the background knowledge needed to set up this work in the context of near-Earth space. The Earth’s magnetosphere is described, with detail being given to the magnetosheath. The concept of turbulence in interplanetary space is introduced, as well as the coherent structures that turbulence can produce. These coherent structures identified in the solar wind and magnetosheath are the focus of this work.

Chapter 2: Data sets and pre-processing The time series magnetic field and plasma data sets from the Magnetospheric Multiscale (MMS) and Time History of Events and Macroscale Interactions during Substorms (THEMIS) missions are used in this work to identify these coherent structures. Chapter 2 describes the two missions, their instrumentation for observing magnetic fields and plasma data, and the resolution of the data products. Also described are the observation periods from MMS and THEMIS that are used to select data in the solar wind and magnetosheath.

Chapter 3: Wavelet analysis as a single-spacecraft method This chapter first defines wavelet transforms and their mathematical properties. Then, it connects the theory of the wavelet power spectrum with magnetohydrodynamic quantities that are used to characterize different magnetic structures, using single-spacecraft measurements. The chapter then outlines the criteria to identify and categorize magnetic structures using wavelet transforms of the magnetic field and plasma data of the observation periods. Lastly, a statistical analysis of the physical quantities of events identified with this method is presented.

Chapter 4: Grad-Shafranov reconstruction and automated identification algorithm The Grad-Shafranov chapter derives the Grad-Shafranov (GS) equation, which can be used to reconstruct two-dimensional cross-sections of magnetic structures. The GS equation is then expanded to include structures with a velocity flow remaining in the frame of reference of the moving structure. This chapter outlines the detailed basis of the reconstruction and criteria for identification of such structures. 2D reconstructions of selected events are presented, and an analysis of the physical quantities (including those unique to the GS-based method) is given.

Chapter 5: Combined analysis This chapter delivers the results of the wavelet analysis and GS-based algorithm in relation to one another. While not directly

comparable, the two methods yield complementary results that are used to interpret the analysis results in relation to turbulence.

Chapter 6: Coordinated analysis results The subsection of observation periods with simultaneous observations in the magnetosheath and solar wind are discussed. These unique observations allow for a more direct comparison of the magnetic structures identified in these two regions. A statistical analysis of structures identified by both wavelet analysis and GS-based reconstruction, using the coordinated observation intervals, is presented.

Chapter 7: Conclusions and Future Work The final chapter includes a summary of the work done in this dissertation, the major findings of this study, and future work to be done. The observation intervals of in situ data, the identification methods, and their results are summarized and interpreted.

Appendices The appendices provide supplemental information to Chapters 2 and 4. Appendix A lists the observation periods from MMS and THEMIS used in the study. Appendix B displays a flow chart of the GS-based automated reconstruction and identification algorithm as implemented by Hu et al. (2018) and Zheng and Hu (2018). Appendix C contains supplemental results.

Chapter 1. Introduction

1.1 Space Environment

1.1.1 Interplanetary magnetic field and near-Earth solar wind

It was proposed by Parker (1958) that there was gas pushed radially outward from the sun, called solar wind, reaching typical speeds of 400-800 km/s. As a spacecraft traverses near-Earth space, it moves from the solar wind through the different regimes of the terrestrial magnetosphere, which is the spatial domain of the magnetic-field lines that connect to the Earth (Borovsky and Valdivia, 2018). Before experiencing the near-Earth regime, the particles emitted from the sun move through the interplanetary medium, and are subject to the magnetic field of the sun. The interplanetary magnetic field (IMF) is the magnetic field of the sun that is carried out in the solar system by the solar wind. The IMF takes the shape of an Archimedean spiral due to the rotation of the sun, as seen in Figure 1.1.

The charged particles in the solar wind, primarily electrons and protons (ionized hydrogen), stream outward from the sun with the spiral field lines of the IMF. When the IMF meets the Earth's magnetic field, these particles can enter the magnetosphere and cause phenomena such as auroras and geomagnetic storms.

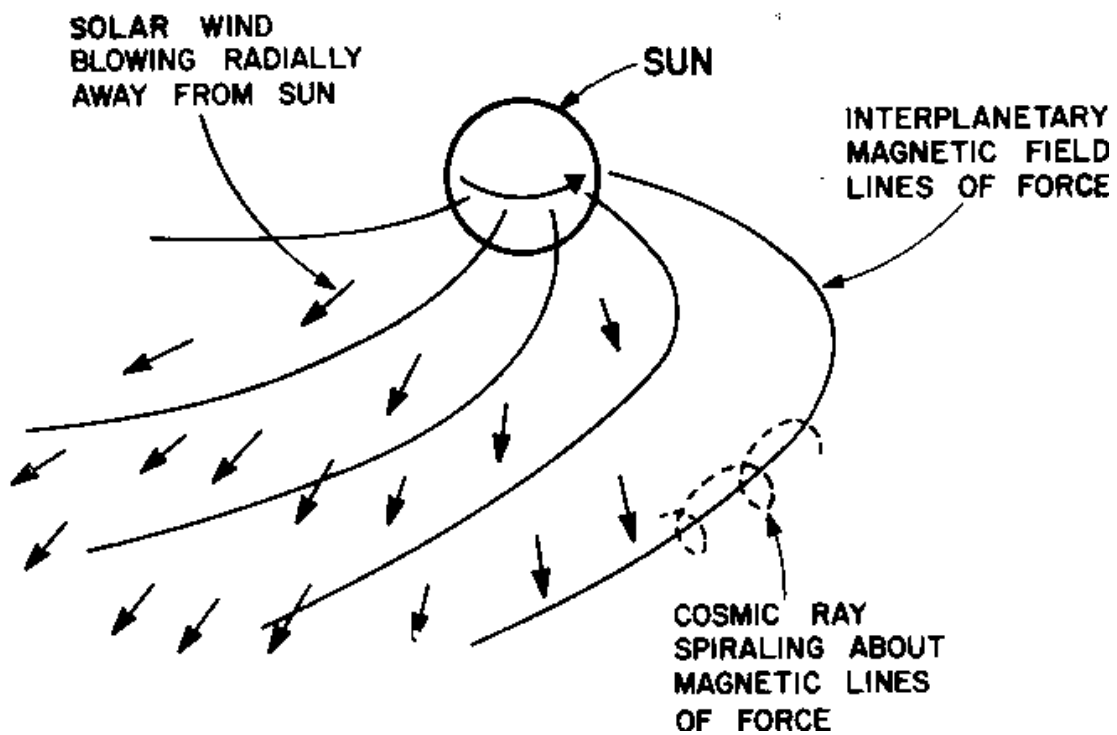


Figure 1.1: The IMF is carried away from the sun by the solar wind in an Archimedean spiral (McCracken, 1967).

In general, solar wind streams can be divided into the fast and slow solar wind. Fast solar wind originates from coronal holes, while slow solar wind originates near the solar equator from coronal streamers. Other variations in solar wind properties can be caused by solar wind transients, such as coronal mass ejections. Coronal mass ejections release energetic plasma from the sun into interplanetary space, and this release can perturb the solar wind. In near-Earth space (~ 1 AU), the solar wind velocity is observed to be approximately 200-800 km/s. As the solar wind encounters the magnetic field of Earth, it is mostly deflected around the Earth's magnetosphere. The solar wind that enters the magnetosphere sees a significant drop in velocity, but an increase in density.

1.1.2 Bow shock

The magnetosphere presents an obstacle to the flow of the solar wind, and as the solar wind rapidly decelerates from supersonic flow into a subsonic flow, a standing fast shock is formed upstream of Earth (Dimmock and Nykyri, 2013). The plasma is deflected around the magnetosphere as it reaches the bow shock. The bow shock is a collisionless shock that forms from the interaction of the solar wind with Earth's magnetic field. It forms a parabolic boundary around the Earth, with the nose being approximately $15 R_E$ in distance in the sunward direction. However, this boundary is constantly moving due to changing solar wind properties. Many studies have used statistics (Kruparova et al., 2019), machine learning techniques (Lalti et al., 2022), or empirical models (Chapman and Cairns, 2003) to identify and locate bow shock crossings of different space-

craft. The interaction of the solar wind with the bow shock can generate magnetic islands and other structures (Karimabadi et al., 2014) in the downstream magnetosheath, and interactions within the magnetosheath lead to wave generation and dissipation, magnetic reconnection, and turbulence (Shaikh and Raghav, 2022).

1.1.3 Magnetosheath

The magnetosheath is a region of shocked, turbulent, highly magnetized plasma that forms directly downstream of the bow shock. The flow of the solar wind is impeded by the Earth's magnetic field; therefore, the compressed, heated, and turbulent solar wind gets wrapped around Earth's magnetic field. This interface between Earth's terrestrial magnetosphere and the solar wind plays a significant role in the flow of particles across these boundaries. Plasma in the magnetosheath experiences large fluctuations, and Hadid et al. (2018) estimates that the average energy cascade rate within the magnetosheath is approximately two orders of magnitude larger than the solar wind. The geometry of the bow shock and the interplanetary magnetic field determines the plasma dynamics of the magnetosheath (Yordanova et al., 2020). Under a quasi-perpendicular angle of the shock normal ($> 45^\circ$), the plasma experiences a sharp decrease in the velocity and sharp increase in the magnitude of the magnetic field. The temperature anisotropy is typically larger in the quasi-perpendicular region, and the quasi-perpendicular region has lower energy flux than the quasi-parallel region (Gurchumelia et al., 2022). This turbulent layer of plasma is bounded by the

magnetopause, which is the outer boundary that separates the solar wind from the magnetosphere.

1.1.4 Magnetopause

The magnetopause is the boundary at which the solar wind dynamic pressure is approximately equal to the pressure of Earth's magnetic field (Shue et al., 1997). Because the pressure is not static, the magnetopause boundary moves in relation to the solar wind properties. The standoff distance of the magnetopause nose can be estimated by taking the solar wind ram pressure and setting it equal to the magnetic pressure of Earth's magnetic field. This distance is typically 6-15 R_E , based on solar wind conditions (Collado-Vega et al., 2023). Figure 1.2 shows an overview of the bow shock and magnetopause boundaries, as well as a representation of the flow of plasma (black arrows).

The magnetopause acts as a sieve, allowing charged particles to enter the magnetosphere. Energetic particles entering the terrestrial magnetosphere leads to geomagnetic activity and has implications for space weather. Positive (negative) ions (electrons) that drift westward (eastward) contribute to the ring current, which affects the strength of a geomagnetic storm (Williams, 1981). Magnetic reconnection at the magnetopause injects magnetic flux into the tail region of the magnetosphere (Tsurutani et al., 1990). Vortices at the edges of the magnetopause, e.g. Kelvin-Helmholtz vortices which occur from a shear due to the velocity difference of the magnetosphere and solar wind plasmas across the mag-

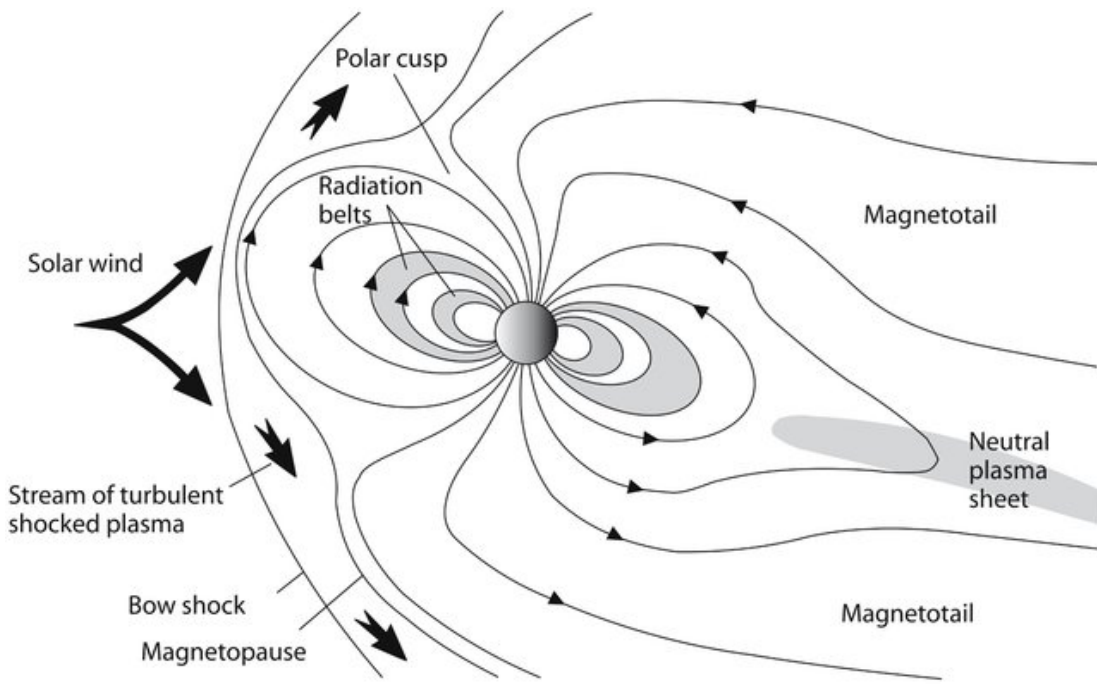


Figure 1.2: Diagram of the magnetopause and Earth's magnetic field lines (Andersen, 2018). The thick arrows show the direction of the flow of plasma as it enters the magnetosheath and is wrapped around the magnetosphere. The non-uniform shape of the magnetopause can be seen.

netopause interface (Nykyri and Otto, 2001), can also act as a method of two-way transport of energetic particles.

1.1.5 Magnetosphere

The magnetopause is the boundary at which the Earth's magnetic field becomes the dominant magnetic field in the region. This region, the magnetosphere, is highly dynamic due the influx of mass, momentum, and energy from the solar wind. As can be seen in Figure 1.2, the Earth's magnetosphere is a dipole; however, it is stretched by the solar wind from the dayside out to several Earth radii in the nightside, forming an elongated tail (Borovsky and Valdivia, 2018).

1.2 Turbulence & coherent structures

As energy cascades through a system, it is transferred to increasingly smaller scales, and is eventually dissipated. This turbulent process leads to numerous physical effects, including the formation of structures caused by fluctuations in the velocities, magnetic field, and density of plasmas (Matthaeus et al., 2015). Since these various quantities are transported along the direction of the magnetic field lines, the stagnation of these quantities leads to an accumulation of gradients. Neutral points and points of stagnation therefore play a key role in coherent structure formation (Matthaeus et al., 2015). “Cellularization”, which is when relatively relaxed regions separated by strong gradients occur, due to the combined effects of this transport and the concentration of gradients (Matthaeus

et al., 2015). Self-organization such as a cellularization is associated with turbulence, specifically in which one quantity is dissipated while the other quantities are held constant. Rapid relaxation of self-organized cells happens differently for distinct cells: stress accumulates along boundaries with other cells as each region relaxes to a maximal extent. As these boundaries experience higher stress, they become concentrated and form small-scale coherent structures, for example current sheets. Larger scale cells are then formed from the partially relaxed regions. These cells form structures such as flux tubes, flux ropes, and current sheets (Matthaeus et al., 2015). Alfvénic structures, along with current sheets, flux tubes, and/or magnetic flux ropes, occur on a wide range of spatial scales that are increasingly resolved by modern spacecraft measurements (Greco et al., 2018; Pecora et al., 2019; Zheng and Hu, 2018; Artemyev et al., 2019).

1.2.1 Interplanetary flux ropes

In magnetohydrodynamics, the magnetic field geometry influences the direction in which various quantities (energy, plasma quantities, etc.) are transported. When the magnetic field lines are twisted such that they preside in a distinctive tube-like volume with a coherent helical configuration, they are often characterized as a flux rope. These magnetic structures have a high magnetic field, which experiences a rotation (change in sign), and low plasma pressure sometimes (Cartwright and Moldwin, 2008). The spiral tube-like magnetic field lines in a small-scale flux ropes (SFR) wrap around a central axis, as shown in Figure 1.3, which leads to a strong axial core magnetic field.

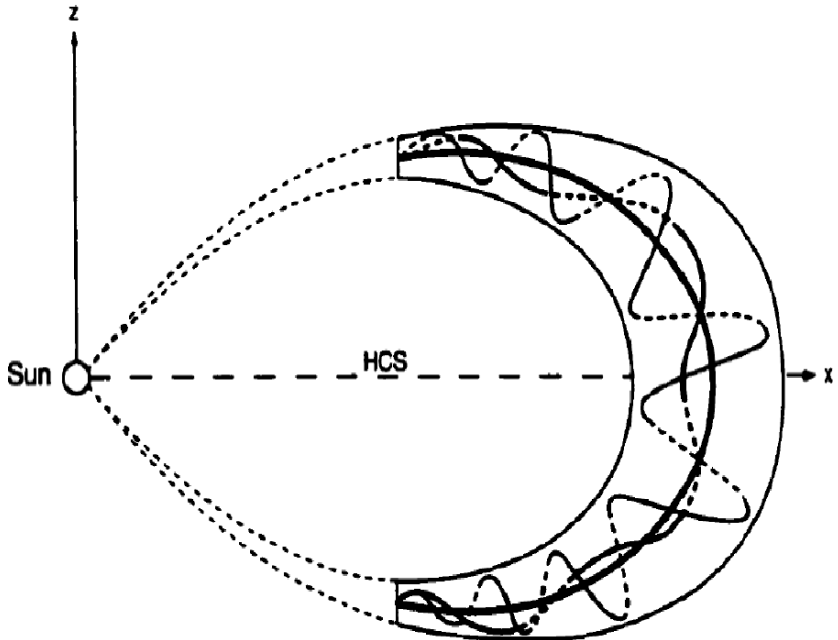


Figure 1.3: Diagram of a magnetic cloud, with twisted magnetic field lines in a tube-like formation around a central axis (Feng et al., 2020).

In situ observations show that a continuous distribution of flux ropes sizes is present in the solar wind (Feng et al., 2007; Hu et al., 2018), but large-scale structures tend to be more easily identifiable and are better understood than small-scale flux ropes. Large-scale structures, also known as magnetic clouds, originate from the sun as a subset of interplanetary coronal mass ejections, and as such have distinguishable features. SFRs have a more ambiguous origin, and typically exhibit spatial scales $\lesssim 0.01$ AU and time scales from less than a few minutes to a few hours based on in situ spacecraft measurements and analysis in the solar wind near Earth (Cartwright and Moldwin, 2010; Feng et al., 2007; Hu et al., 2018). Figure 1.4 shows the distributions of duration and scale size of

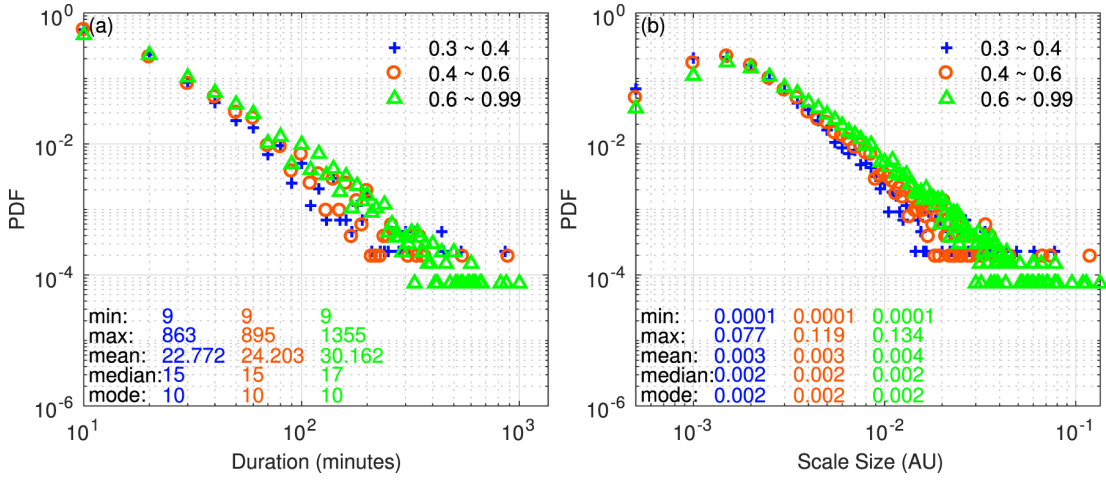


Figure 1.4: Distributions of (a) duration and (b) scale size of SFRs from Helios 1 and 2, grouped by radial distances from Chen and Hu (2020).

SFRs, grouped by heliocentric radial distances between ~ 0.3 and 0.99 AU, from Chen and Hu (2020).

1.2.2 Alfvénic structures

This twisted magnetic field topology is not unique to static flux rope structures in the interplanetary medium. Static SFRs are convected with the solar wind (Cartwright and Moldwin, 2008). Alfvénic structures have similar magnetic field topology as flux ropes, but they propagate in the direction of the magnetic field. Alfvén waves are electromagnetic waves in which ions oscillate along a magnetic field line at the Alfvén speed. The restorative force comes from background magnetic field providing an effective tension while the inertia comes from the mass of the ions (Alfvén, 1942). These structures have significant field-aligned (parallel or anti-parallel) flow, which is characterized by Alfvénicity, the alignment between

the velocity and magnetic field components. The Alfvénicity of a structure can be evaluated with the Walén test, a linear regression between the remaining flow, $\mathbf{V}_{\text{sw}} - \mathbf{V}_{\text{HT}}$, and the Alfvén velocity \mathbf{V}_A . The physical properties of a moving structure are best evaluated in the co-moving frame, for which the de Hoffmann-Teller frame (de Hoffmann and Teller, 1950) is the simplest to apply. Thus, we subtract the de Hoffmann-Teller velocity \mathbf{V}_{HT} from the bulk flow velocity \mathbf{V}_{sw} in order to evaluate the field-aligned flow in magnetic structures.

Like SFRs, the helical structure of Alfvénic structures leads to high levels of magnetic helicity H_m ¹, a measure of twisted-ness of the field lines. Another quantity that can be used to distinguish static structures and Alfvénic structures is residual energy, E_r ¹, which characterizes the imbalance between magnetic and kinetic energy. Level of Alfvénicity, is also characterized by the correlation between velocity and magnetic field fluctuations which can be represented by cross helicity H_c ¹. Alfvénic structures are structures that exhibit high levels of Alfvénic characteristics. The latter two parameters have been widely adopted as a way to describe the degree of Alfvénicity based on time-series analysis. For Alfvénic structures, the absolute value of the normalized cross helicity $|\sigma_c|$ is close to 1, and the normalized residual energy σ_r is close to 0. For pure Alfvén waves, these two quantities are suggested to be 1 and 0, respectively (Bruno and Carbone, 2013). Flux ropes in the traditional view are supposed to have low Alfvénicity, i.e, being static. Considering the crossing of the boundary between the solar wind and the magnetosheath, I adopt a broad definition of SFRs in this study, by in-

¹defined in Section 3.3

cluding both quasi-static structures and those possessing significant field-aligned flows with modest to high levels of Alfvénicity (Chen and Hu, 2022).

1.3 Objectives

Previous studies of SFRs such as Chen and Hu (2022) have used the extended Grad-Shafranov (GS) based techniques for the solar wind plasma; however, this algorithm was not used in other regions of near-Earth space such as the magnetosheath. Furthermore, many studies regarding flux ropes and other magnetic structures (Zhao et al., 2020; Chen et al., 2021) focus on events identified during specific periods of time, instead of using multiple spacecraft for a coordinated study in the regions immediately upstream and downstream of the bow shock. In this study, I seek to identify magnetic structures via both the wavelet analysis and the extended GS-based algorithm in a systematic manner. This work characterizes magnetic structures with varying degrees of Alfvénicity as they move across boundaries in near-Earth space, and describe the characteristics and changes that magnetic structures exhibit as they occur in the solar wind and the magnetosheath, respectively.

The identification and analysis of structures moving across boundaries such as the Earth’s bow shock will give insight into how their properties change across this boundary as well as further our understanding of the interrelation between these structures. This study is observational and data-focused, with the specific goal to collect an inventory of events with high magnetic helicity.

Another objective is to interpret and inter-compare the statistical properties of the structures, largely the SFRs, from the upstream solar wind and magnetosheath.

Chapter 2. Data sets and pre-processing

The data in this study are time series measurements from the Time History of Events and Macroscale Interactions during Substorms-Acceleration, Reconnection, Turbulence and Electrodynamics of the Moon’s Interaction with the Sun (THEMIS-ARTEMIS) mission and the Magnetospheric Multiscale (MMS) mission. The former mission seeks to investigate substorms in the Earth’s magnetosphere, observe the Earth’s radiation belts, and examine solar wind-magnetosphere interaction on the day-side.

2.1 THEMIS data set

The THEMIS spacecraft are optimized for observing different regions of the magnetosphere and near-Earth solar wind. The five THEMIS probes (THM A-E) are traversing near-Earth space in different regions and orbits according to the science phases. THEMIS-B and THEMIS-C were reassigned as ARTEMIS-P1 and ARTEMIS-P2, respectively, in 2009 to facilitate observations at lunar Lagrange points 1 and 2. The separation between the probes, specifically during the mission phases in which simultaneous observation between the solar wind and magnetosheath are available, makes this mission ideal for use in this study.

Aboard each of the five THEMIS probes, identical Electrostatic Analyzer (ESA) instruments measure ion and electron distribution functions in three dimensions via spherical top-hat electrostatic analyzers (McFadden et al., 2008). The observable range of energy fluxes of the ESA instrument is approximately 1.6-25 keV for ions and 2-32 keV for electrons. The Fluxgate Magnetometers (FGM) on each THEMIS probe (Auster et al., 2008) are single digital fluxgate magnetometers with a sensor at the end of a 2 meter boom. Because of the mission goals related to magnetic reconnection during substorms, the fluxgate magnetometers are very sensitive, with precision down to 0.1 nT, and operate in the range of 0.1-25000 nT (Auster et al., 2008). Figure 2.1 displays the arrangement of the instruments on a singular THEMIS probe. The FGM is located on the end of the boom, with the ESA and other instruments placed around the body of the spacecraft.

2.2 MMS data set

The MMS mission, comprised of four identical probes in a tetrahedral formation, also moves through the solar wind and magnetosheath. The magnetic field data from MMS come from the Fluxgate Magnetometer (FGM), which is part of the FIELDS suite on MMS (Torbert et al., 2016). The MMS FIELDS suite is responsible for measuring the magnetic and electric fields. The FGM is comprised of two magnetometers on each spacecraft, one analog (AFG) and one digital (DFG). The magnetometers measure the magnetic field components with three-axis sensors (Torbert et al., 2016). The two magnetometers are located

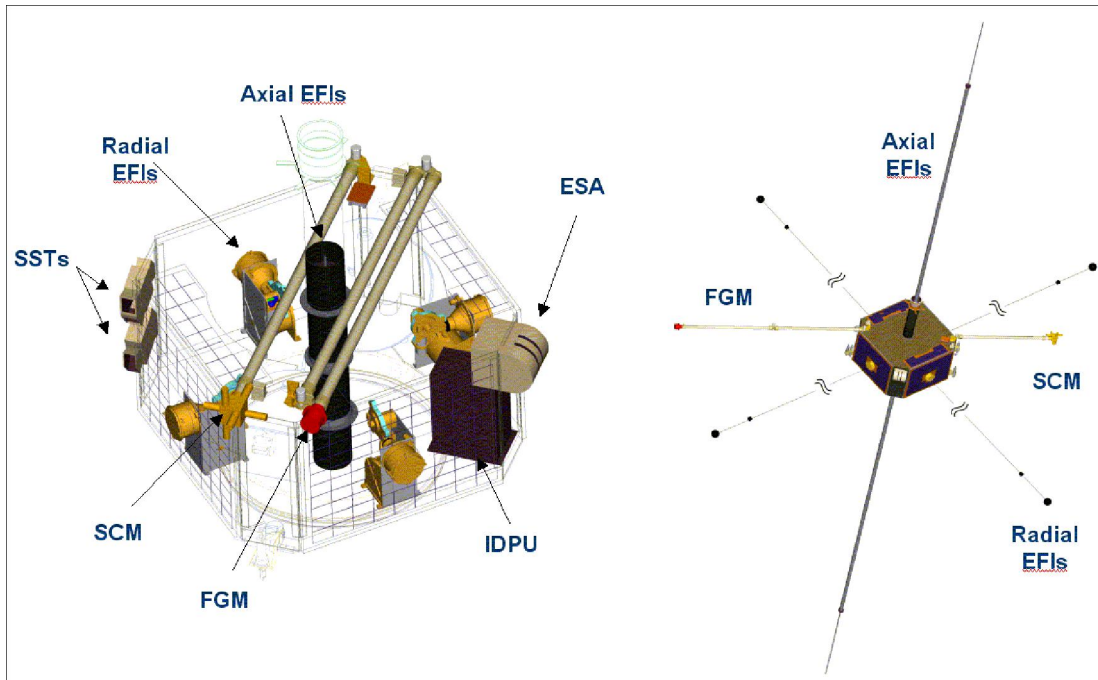


Figure 2.1: Configuration of instruments on a singular THEMIS probe. On the left, all of the instruments are shown, including the FGM and ESA. On the right, the Fluxgate Magnetometer (FGM) can be seen at the end of its 2 meter long boom, along with the Search Coil magnetometer (SCM) and Electric Field Instrument (EFI) (University of California, Berkeley; NASA, 2012).

on opposite sides of the spacecraft, each at the end of a five meter long boom (see Figure 2.2). Because there are two magnetometers on each spacecraft, they provide redundant data which is used to cross-calibrate the AFG and DFG instruments (Torbert et al., 2016). The other instruments of the FIELDS suite are the Search Coil Magnetometer (SCM), which measures the magnetic field fluctuations over 1 Hz-6 kHz. The Spin-plane Double-Probes (SDP) and the Axial Double Probe (ADP) measure the electric field in the spin plane and along the spin axis, respectively. The Electron Drift Instrument measures ambient electron flux, and the EDI is used to conduct geometric measurements of the electric field and time-of-flight measurements for the magnetic field. Table 2.1 displays the data products used in this work.

The Fast Plasma Investigation (FPI) (Pollock et al., 2016) instrument on MMS measures the velocity-space distribution of ions and electrons in the plasma in near-Earth space, from which their energy and velocity can be ascertained. Four dual electron spectrometers (DES) and four dual ion spectrometers (DIS) are evenly placed around each of the four probes, which are then connected to individual (IDPU) and central (CDPU) data processing units (Pollock et al., 2016). The spectrometers measure the energy of the ions and electrons from 10 eV to 30 keV by measuring their differential directional flux distributions at a time resolution of 150 ms (for ions) and 30 ms (for electrons). Figure 2.3 displays the layout of the FPI spectrometers aboard each MMS spacecraft.

Data product	Instrument	Symbol	Units	Cadence [s]
Magnetic field vector	FGM	B_X, B_Y, B_Z	nT	2.74 - 4.295
Flow velocity vector	ESA	V_X, V_Y, V_Z	km/s	2.74 - 360 ^a
Proton number density	ESA	N_p	cm ⁻³	2.74 - 4.295
Proton temperature	ESA	T	eV	2.74 - 4.295
Ion energy spectra	ESA		eV/(cm ² s sr eV)	2.74 - 4.295
<hr/>				
Magnetic field vector	FGM	B_x, B_y, B_z	nT	4.5
Flow velocity vector	FPI	V_x, V_y, V_z	km/s	4.5
Proton number density	FPI	N_p	cm ⁻³	4.5
Proton temperature	FPI	T	eV	4.5
Ion energy spectra	FPI		eV/(cm ² s sr eV)	4.5

Table 2.1: Data products from THEMIS (top) and MMS (bottom) used in this study.

^aFor the flow velocity vector from THEMIS, there are some periods in which 6-minute data was up-sampled to match the ~3-second magnetic field data.

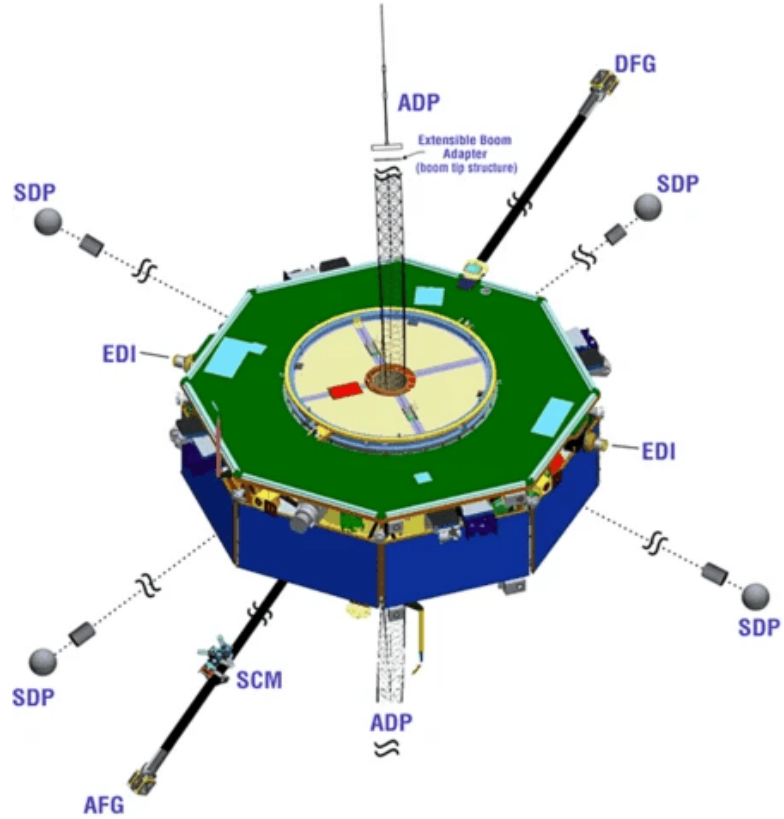


Figure 2.2: The MMS FIELDS suite on an individual probe, which measures magnetic and electric fields. The analog fluxgate magnetometer (AFG) and digital fluxgate magnetometer (DFG) are located at the ends of the two five meter booms, in the bottom left corner and top right corner. The Search Coil Magnetometer (SCM), Electron Drift Instrument (EDI), Spin-plane Double-Probes (SDP), and the Axial Double-Probes (ADP) complete the FIELDS suite aboard each MMS spacecraft (Burch et al., 2024).

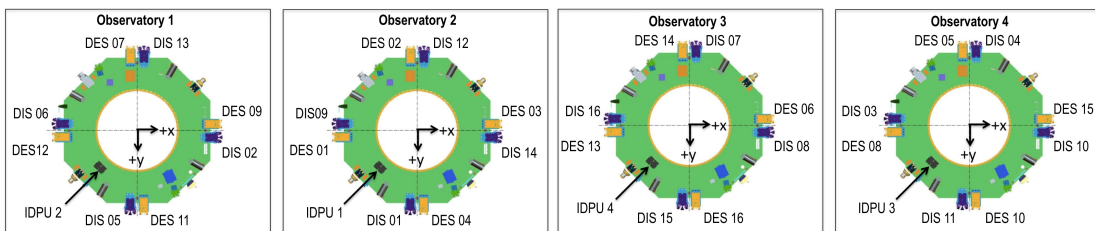


Figure 2.3: Diagram showing the full FPI instrument suite across each of the MMS spacecraft (Pollock et al., 2016).

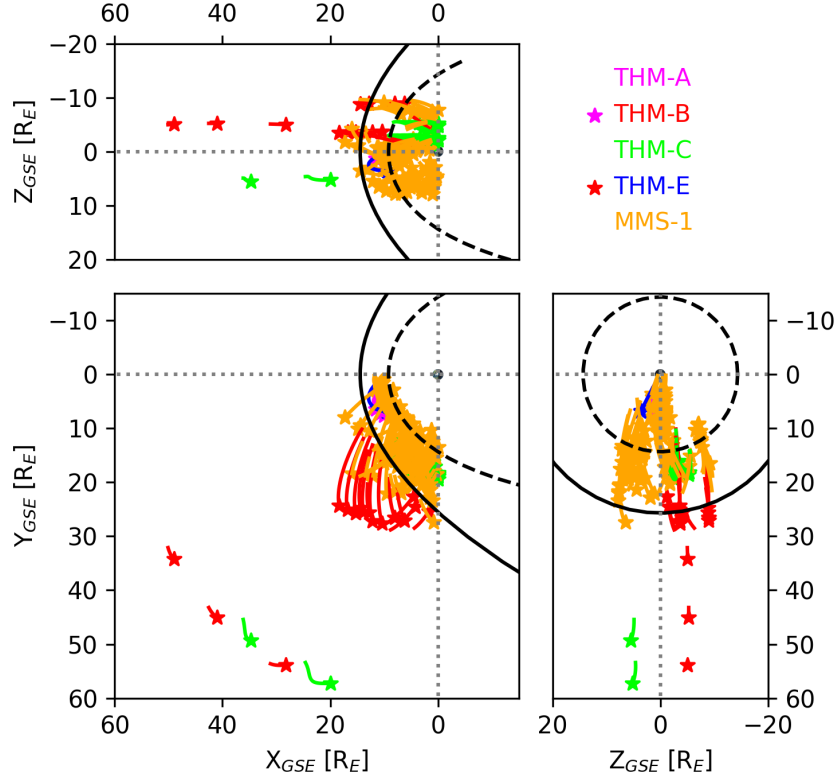


Figure 2.4: Orbits for all analysis time periods are shown in the Geocentric Solar Ecliptic (GSE) coordinates for THEMIS probes A, B, C, and E (THM-A, THM-B, THM-C, THM-E) and MMS-1 probe (see legend), with the stars marking the end of each orbit period. The approximate nominal locations of the magnetopause (dashed black line) modeled using the Shue et al. (1997) model and bow shock (solid black line) modeled using Slavin et al. (1984) are shown, based on the IMF data obtained for one period in 2015 only.

2.3 Data selection and pre-processing

Hours-long periods of THEMIS data with cadence $\Delta t \sim 3$ seconds and MMS data with $\Delta t = 4.5$ seconds in the magnetosheath and near-Earth solar wind are chosen such that each analysis interval is entirely contained in one region to avoid transition regions. Figure 2.4 shows the orbit segments of the THEMIS and MMS-1 probes for the selected time periods. The orange orbit lines display portions of the MMS-1 orbits from 2015-2023. The pink, red, green, and blue orbit lines show the THEMIS orbits in 2008, 2009, 2018, and 2022. The solid curve and dashed curve are the estimated bow shock and magnetopause boundaries (Slavin et al., 1984; Shue et al., 1997). These time periods, ranging in lengths from approximately 6 hours to 26 hours, are identified by looking at time series data and finding data segments bounded by simultaneous changes in magnetic field, plasma density, velocity, and ion spectra. Short instances of possible bow shock crossings (including multiple crossings) are identified in certain time periods, and the events identified in these crossing periods are removed from the final lists.

Figures 2.5 and 2.6 are examples of two observed time periods in the magnetosheath from MMS-1 and THM-C, respectively. Figure 2.7 shows the same observation period as Figure 2.6, but in the solar wind as observed by THM-B. These figures show the time series of magnetic field, plasma velocity, proton density, temperature, and ion energy spectra, as well as calculated values such as Alfvén velocity and proton beta. These quantities are used in our analysis, and also to identify the region in which the spacecraft was located. During the

19-20 June 2009 time period, THM-C experienced a bow shock crossing, which is denoted by the grey-shaded interval in Figure 2.6. By looking at the time series data during the whole period, and identifying changes in the data such as magnetic field and ion spectra that were consistent with bow shock crossings (Lalti et al., 2022; Trotta et al., 2022), periods where the spacecraft were experiencing a bow shock crossing were identified. The events in the bow shock crossing periods are removed from the final event list.

In addition to manually identifying periods in the solar wind and the magnetosheath, the published list of MMS data periods in the magnetosheath and solar wind from Toy-Edens et al. (2024a) was also used. Their work focused on using unsupervised clustering to classify plasma regions in 8 years' worth of dayside MMS data (Toy-Edens et al., 2024b). The 1-minute resolution data was classified into the following regions: solar wind, ion foreshock, magnetosheath, and magnetosphere. The Toy-Edens et al. (2024a) list contains over 9000 time periods in which MMS-1 to MMS-4 probes were identified to be solidly in the magnetosheath, with the minimum period being 15 minutes in length. The list of Toy-Edens et al. (2024a) was refined by taking time periods with a duration longer than 5 hours for both the solar wind and magnetosheath regions, which is comparable to the shortest identified time period of THEMIS data. After further refining their magnetosheath list to the region downstream of the quasi-perpendicular bow shock (corresponding to a condition that the spacecraft location of $Y_{GSE} > 0$), one-hundred and seven time periods were obtained to be used in this study. Fifty-eight periods, in which MMS traversed the solar wind up-

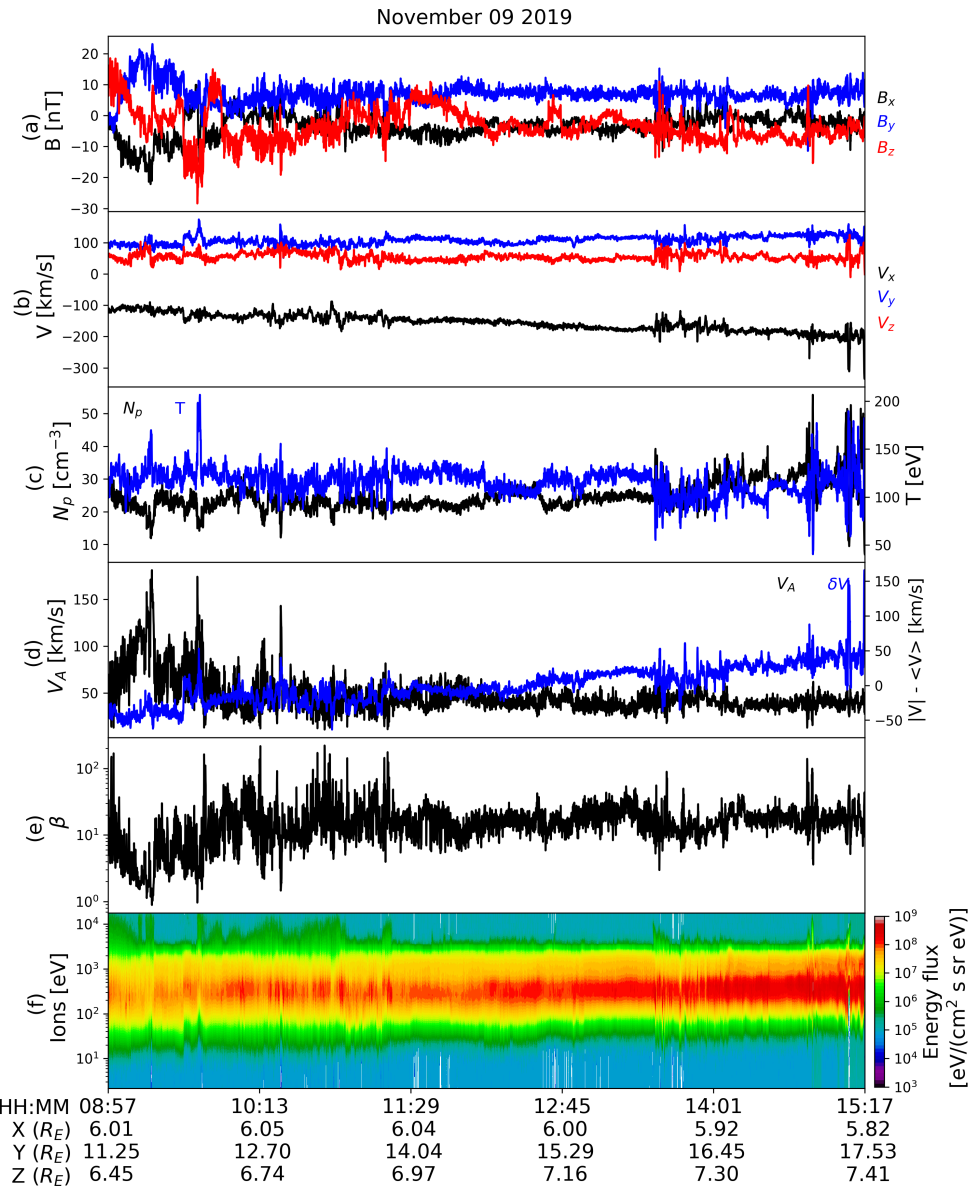


Figure 2.5: Time series data observed by MMS-1 for \sim 6 hours in the magnetosheath on 9 November 2019, with supplementary ephemeris data in GSE coordinates. The panels show a) magnetic field components, b) the components of flow velocity \mathbf{V}_{sw} , c) proton density and temperature, d) Alfvén speed and fluctuations of the magnitude of the velocity, e) proton beta, and f) ion spectra.

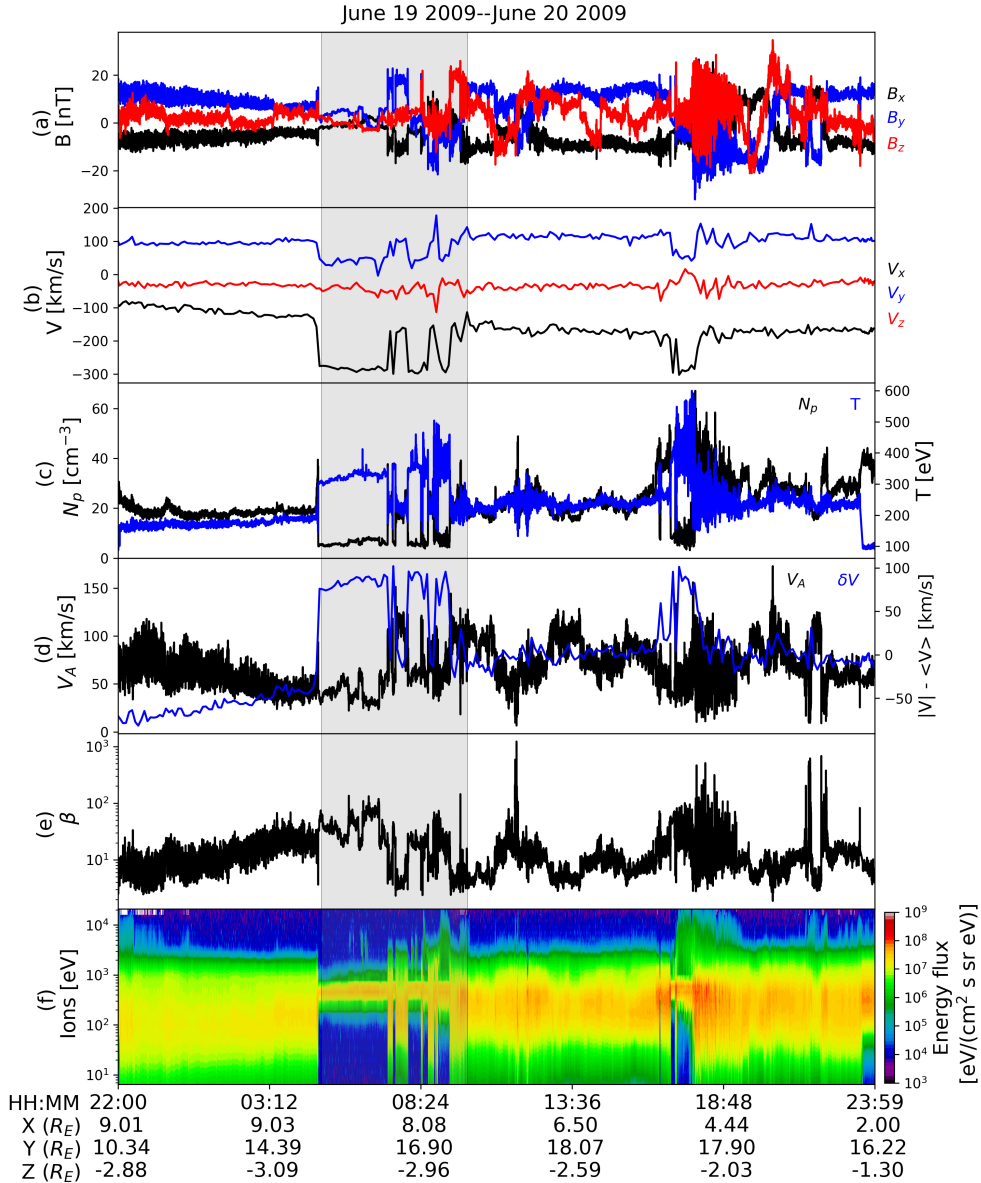


Figure 2.6: Time series data observed on 19-20 June 2009 by THM-C. This observation period spans ~ 26 hours in the magnetosheath, with a bow shock crossing (grey region) identified during 5:00-10:00 UT on 20 June 2009. Similar to Figure 2.5, the panels show the a) magnetic field, b) velocity, c) proton density and temperature, d) Alfvén speed and fluctuations of the magnitude of the velocity, e) proton beta, and f) ion spectra.

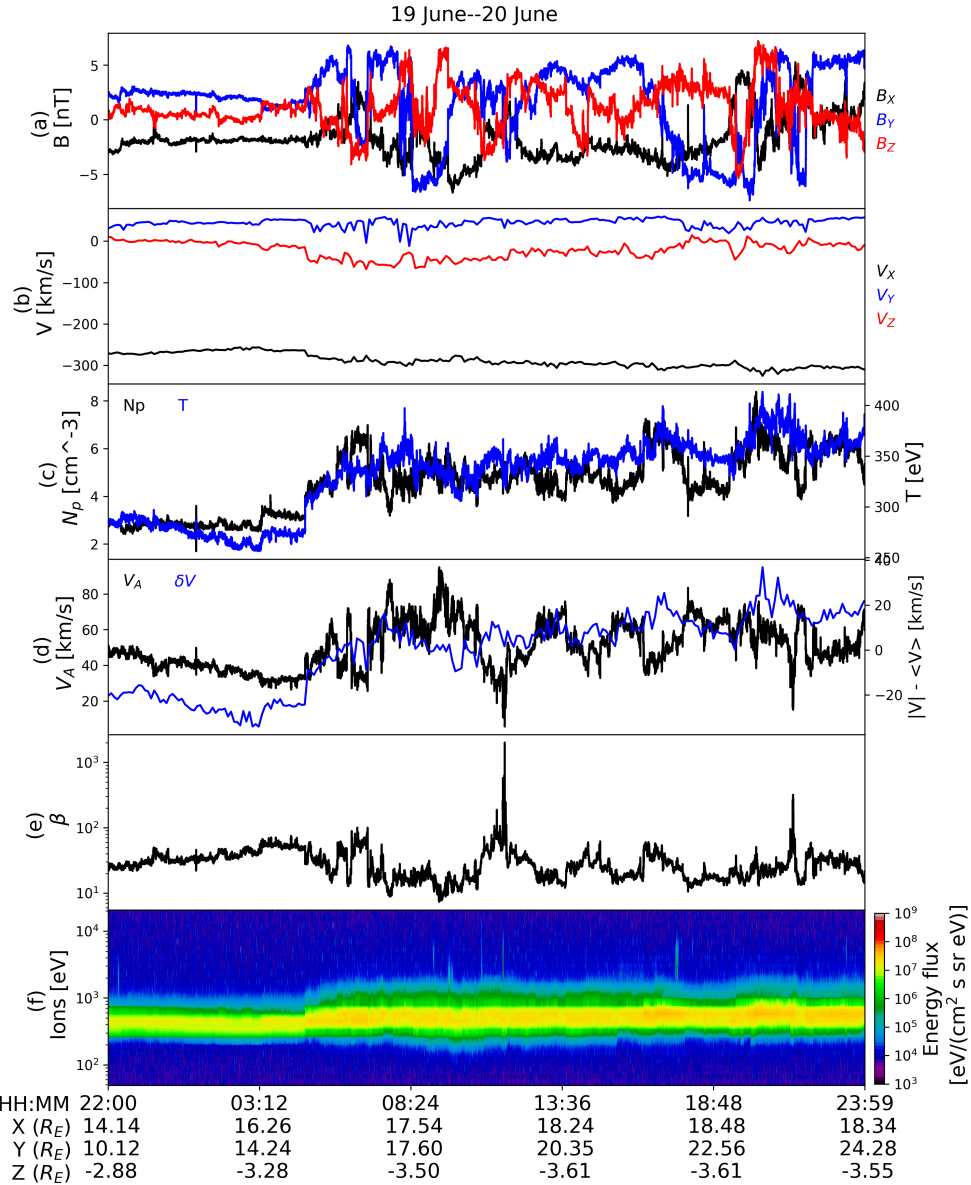


Figure 2.7: Time series data observed on 19-20 June 2009 by THM-B. This observation period spans ~ 26 hours in the solar wind. Similar to Figure 2.5, the panels show the a) magnetic field, b) velocity, c) proton density and temperature, d) Alfvén speed and fluctuations of the magnitude of the velocity, e) proton beta, and f) ion spectra.

stream of the quasi-perpendicular bow shock, were obtained from the Toy-Edens et al. (2024a) solar wind list. Toy-Edens et al. (2024b) include all MMS probes in their analysis; however, only MMS-1 is considered since presumably the other 3 MMS probes are in the same region; therefore, only the results from MMS-1 are reported. In total, from the Toy-Edens et al. (2024a) list and from our own identification, there were 130 time periods of data identified in the magnetosheath from THM-A, THM-C, THM-E, and MMS-1; and 77 periods identified in the solar wind from THM-B, THM-C, and MMS-1. The total lengths of the search time periods for our study are 1051 hours in the magnetosheath and 676 hours in the solar wind. Summary tables of the observation search intervals in the magnetosheath and solar wind can be found in Appendix A.

Chapter 3. Wavelet analysis as a single-spacecraft method

Single-spacecraft measurements have been used in the identification of small-scale magnetic structures (Pecora et al., 2019; Telloni et al., 2012; Hu et al., 2018; Zheng and Hu, 2018; Zhao et al., 2020). The time series data can be treated as a spatial snapshot due to the effective stationary state of the plasma medium traversed by a spacecraft relative to the fast-moving solar wind. Time series data are transformed directly to spatial distributions (Taylor, 1938). Therefore, time-frequency transforms, such as wavelet transforms, are conceivably useful for analyzing features of in situ spacecraft time series at different frequencies over time (Torrence and Compo, 1998). Specifically the power spectra associated with a number of selected MHD quantities are derived to characterize the underlying magnetic structures.

3.1 Wavelet transforms

Wavelet transforms are used to analyze time series with non-stationary power at different frequencies (Torrence and Compo, 1998) using non-orthogonal wavelet basis functions. Assuming a continuous signal as a function of time t ,

$x = x(t)$, the continuous wavelet transform is defined as

$$W(s, \tau) = \frac{1}{|s|^{1/2}} \int_{-\infty}^{\infty} x(t) \psi^* \left(\frac{t - \tau}{s} \right) dt. \quad (3.1)$$

Here ψ^* is the complex conjugate of the wavelet basis function $\psi(t)$, which is a function that must be localized in time and frequency space, and has zero mean (Torrence and Compo, 1998).

As usual, with a discrete set of data points $x_n = x(t_n)$ with time resolution δt , the continuous wavelet transform takes the discrete form

$$W_n(s, t) = \sum_{n'=0}^{N-1} x_{n'} \psi^* \left[\frac{(n' - n) \delta t}{s} \right]. \quad (3.2)$$

In practice, discrete wavelet transforms are implemented for time series data by dilating the scale s and translating along the time index n . This results in a two dimensional array of the wavelet transform. The scales are chosen such that

$$J = \frac{\log_2 \left(\frac{N \delta t}{s_0} \right)}{d_j} \quad (3.3)$$

$$s_j = s_0 2^{j d_j}, \quad j = 0, \dots, J \quad (3.4)$$

where $s_0 = 2\delta t$ and the choice of d_j is sufficiently small for the width of the wavelet basis function in spectral space. The Morlet wavelet given in Equation (3.5) is a good wavelet base because it is complex and has good frequency resolution, thus it is frequently used in small-scale flux rope identification (Telloni et al., 2012,

2013; Zhao et al., 2020; Farge, 1992):

$$\psi_0(\eta) = \pi^{-1/4} e^{i\omega_0\eta} e^{-\eta^2/2}. \quad (3.5)$$

Figure 3.1 visually demonstrates the typical transform of a time series data set from the time domain to a time-frequency domain, including the Fourier transform and the wavelet transform. Wavelet transforms take a one-dimensional time series (top left corner of Figure 3.1) and transform it into a two-dimensional series (bottom right corner of Figure 3.1), whereas the Fourier transform applied to a one-dimensional time series yields a one-dimensional series in the frequency domain (top right corner of Figure 3.1). The Fourier transform decomposes a time series function into a combination of the frequencies present in the data set (Farge, 1992). The Fourier transform of a time series $x(t)$ into its frequency domain (index k) is

$$F(k) = \int_{-\infty}^{\infty} x(t) e^{-2\pi i k t / N} dt, \quad (3.6)$$

and with discrete data $x_n = x(t_n)$, it takes the form

$$F_n(k) = \frac{1}{N} \sum_{n=0}^{N-1} x_n e^{-2\pi i k n / N}. \quad (3.7)$$

A short time Fourier transform (bottom left corner of Figure 3.1) can produce a two-dimensional time-frequency domain, but by segmenting the time series and performing a Fourier transform over the segments, the method only yields identical time-frequency domains, for each respective time segment. Fourier transforms

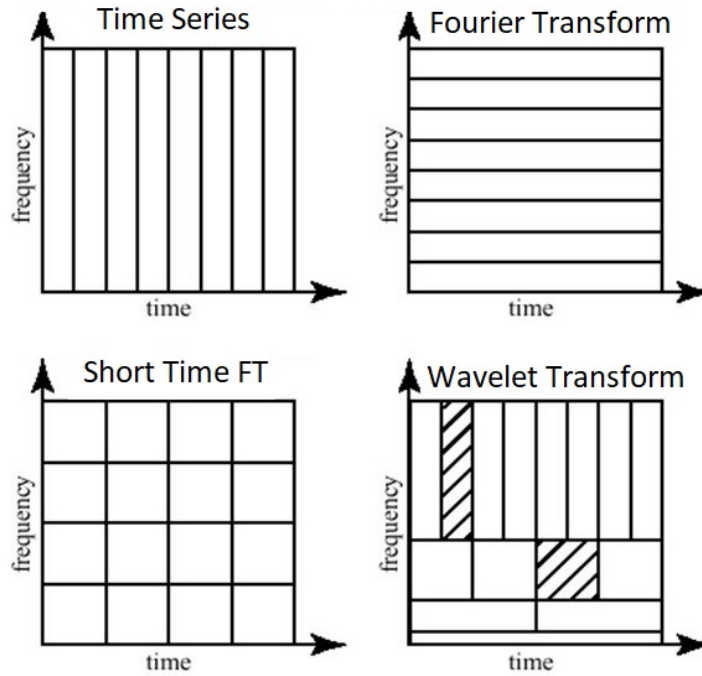


Figure 3.1: Time and frequency resolutions of different transforms applied to a one-dimensional time series dataset. The wavelet transform (bottom right) has non-uniform frequency and time resolution.

theoretically retain all the ‘information’ about an equation, but discrete Fourier transforms are a summation over a finite set and therefore are not as accurate.

3.2 MHD quantities

The magnetic field lines in flux ropes are twisted such that they preside in a tube-like configuration. Thus, flux ropes carry magnetohydrodynamic (MHD) quantities such as cross helicity H_c and magnetic helicity H_m , as well as residual

energy E_r , defined as

$$H_c = \frac{1}{2} \int \mathbf{v} \cdot \mathbf{b} \, d^3\mathbf{r} \quad (3.8)$$

$$H_m = \int \mathbf{A} \cdot \mathbf{B} \, d^3\mathbf{r} \quad (3.9)$$

$$E_r = \frac{1}{2} [\langle \mathbf{v}^2 \rangle - \langle \mathbf{b}^2 \rangle], \quad (3.10)$$

where $\mathbf{B}(\mathbf{x}, t)$ is the magnetic field, $\mathbf{A}(\mathbf{x}, t)$ is the magnetic vector potential, and $\mathbf{v}(\mathbf{x}, t)$ and $\mathbf{b}(\mathbf{x}, t)$ are the fluctuating velocity and magnetic field in Alfvén units. Cross helicity describes the measure of alignment between magnetic and velocity fluctuations, while magnetic helicity describes the “knottedness” of the magnetic field lines (Matthaeus and Goldstein, 1982). High magnetic helicity is a signature of flux ropes, and often accompanied by low cross helicity (Zhao et al., 2020). Residual energy describes the imbalance between magnetic and kinetic energy, and thus according to (3.10), a negative residual energy will characterize an event with higher magnetic energy.

Normalized MHD quantities give insight into the nature of magnetic field structures, and allow us to identify and characterize these events. Approximated in the time domain, the normalized cross helicity and residual energy can be calculated using

$$\sigma_c = \frac{2\langle \mathbf{v} \cdot \mathbf{b} \rangle}{\langle \mathbf{v}^2 \rangle + \langle \mathbf{b}^2 \rangle} \quad (3.11)$$

$$\sigma_r = \frac{\langle \mathbf{v}^2 \rangle - \langle \mathbf{b}^2 \rangle}{\langle \mathbf{v}^2 \rangle + \langle \mathbf{b}^2 \rangle} \quad (3.12)$$

where \mathbf{v} is the remaining flow in the de Hoffman-Teller frame. Single spacecraft measurements cannot be used directly calculate reduced magnetic helicity, therefore other methods are required to approximate this quantity. The power spectral density of a time series describes the distribution of the energy across the frequency components of a signal. Matthaeus and Goldstein (1982) showed that a form of the magnetic helicity can be calculated using single spacecraft measurements by utilizing the power spectral density. This can often be done in a similar fashion using wavelet transforms (Telloni et al., 2012, 2013). The continuous wavelet transform of a one-dimensional time series yields the two-dimensional time-scale spectrogram for a finite time period. This shows how the amplitude of a feature versus the scale varies with time, therefore making it useful in studying the features associated with multi-scale structures. The so-called reduced form of the magnetic helicity gives quantitative information about the magnetic helicity density along the radial dimension, X , and is calculated with Fourier transforms of the Y - and Z -components of the magnetic field, $\tilde{F}(B_Y)$ and $\tilde{F}(B_Z)$,

$$H_m(k) = \frac{2\text{Im}[S_{YZ}(k)]}{k} = \frac{2\text{Im}\left[\tilde{F}^*(B_Y)\tilde{F}(B_Z)\right]}{k}, \quad (3.13)$$

where $S_{YZ}(k)$ is one element of the reduced magnetic power spectral density tensor (Matthaeus and Goldstein, 1982). Telloni et al. (2012) showed that taking X along the radial direction from the sun, wavelet transforms of the magnetic field Y - and Z -components, the Elsässer variables Z^\pm , and kinetic and magnetic energies enable an efficient way to calculate the reduced normalized magnetic

helicity σ_m , cross helicity σ_c , and residual energy σ_r , corresponding to equations (3.8)-(3.10):

$$\sigma_m(k, t) = 2 \frac{\text{Im} [W_Y(k, t) W_Z^*(k, t)]}{|W_X(k, t)|^2 + |W_Y(k, t)|^2 + |W_Z(k, t)|^2}, \quad (3.14)$$

$$\sigma_c(k, t) = \frac{W^+(k, t) - W^-(k, t)}{W^+(k, t) + W^-(k, t)}, \quad (3.15)$$

$$\sigma_r(k, t) = \frac{W_{kin}(k, t) - W_{mag}(k, t)}{W_{kin}(k, t) + W_{mag}(k, t)}. \quad (3.16)$$

Here $W_X(k, t)$, $W_Y(k, t)$, $W_Z(k, t)$, $W^+(k, t)$, and $W^-(k, t)$ are the wavelet transforms of B_X , B_Y , B_Z , Z^+ , and Z^- , respectively. The Elsässer variables, $Z^\pm = \mathbf{v} \pm \mathbf{b}$, are the combination of the velocity and magnetic field fluctuations in Alfvén units. $W_{kin}(k, t)$ and $W_{mag}(k, t)$ are the sums of the power of the wavelet transforms of the components of the velocity and magnetic field (in Alfvén units). Equations (3.14)-(3.16) can also be written in terms of scale and time :

$$\sigma_m(s, t) = 2 \frac{V_{X0} \text{Im} [W_Y(s, t) W_Z^*(s, t)]}{V_0 (|W_X(s, t)|^2 + |W_Y(s, t)|^2 + |W_Z(s, t)|^2)}, \quad (3.17)$$

$$\sigma_c(s, t) = \frac{W^+(s, t) - W^-(s, t)}{W^+(s, t) + W^-(s, t)}, \quad (3.18)$$

$$\sigma_r(s, t) = \frac{W_{kin}(s, t) - W_{mag}(s, t)}{W_{kin}(s, t) + W_{mag}(s, t)}. \quad (3.19)$$

since $\mathbf{k} \parallel \mathbf{V}_0$ (Zhao, L.-L. et al., 2021; Horbury et al., 2008; Taylor, 1938), where \mathbf{V}_0 is the average plasma velocity. Equation 3.17 only shows the first term of the

trace of the power spectrum because the radial component is dominant over the tangential component at 1 AU.

3.3 Algorithm for identification of magnetic structures

In Figure 3.2, the time series of the magnetic field and plasma parameters from 10:20-13:30 UT on 9 November 2019 are shown. Panels (a) and (b) show the magnetic field and velocity components of the time period, with magnetic field magnitude reaching a maximum of about 20 nT and a flow velocity deflected from the Sun-Earth direction. Panel (c) shows relatively high proton density, varying from 20 to 30 cm^{-3} , and proton temperature of $1\text{-}2\times 10^6 \text{ K}$, which is typical for magnetosheath plasma. Panel (d) shows the Alfvén speed and the bulk plasma speed with a mean value for this 3 hour period (193 km/s) subtracted. Panel (e) shows the proton beta, which is between approximately 1-100. Panel (f) of Figure 3.2 displays the spectrogram reduced magnetic helicity, which describes the “knottedness” of the magnetic field lines. Panel (g) shows the normalized measure of alignment between magnetic and velocity fluctuations, reduced cross helicity, and panel (h) shows the imbalance between magnetic and kinetic energy, or reduced residual energy (Matthaeus and Goldstein, 1982). These spectrograms show how the reduced MHD quantities vary in time and frequency, thus allowing us to search them for characteristics that are distinctive to different types of magnetic structures.

Structures with local enhanced magnetic helicity are identified with specific criteria: (i) magnetic helicity with absolute values greater than 0.75, (ii)

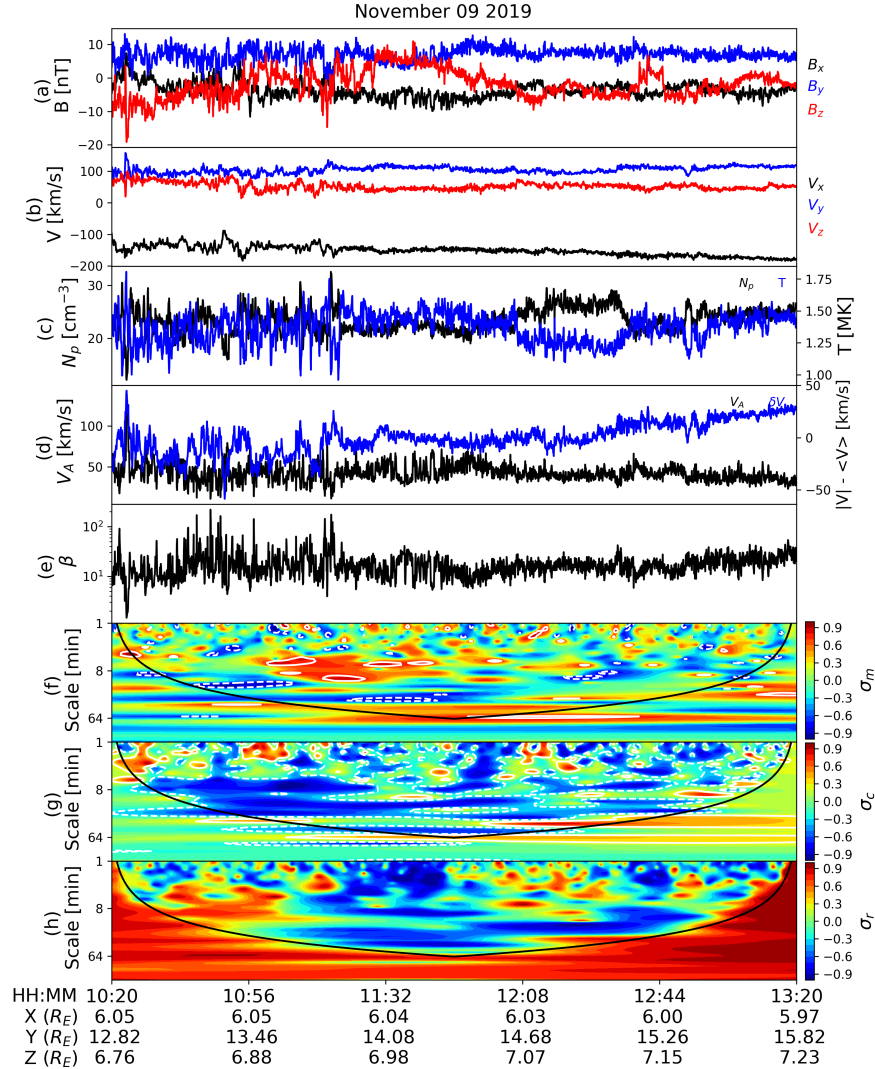


Figure 3.2: Time series of (a) magnetic field, (b) velocity, (c) plasma density and temperature, (d) Alfvén speed and velocity fluctuations, (e) plasma beta, and spectrograms of the normalized (f) reduced magnetic helicity, (g) cross helicity, and (h) residual energy found by wavelet analysis, across multiples scales (as indicated by the vertical axes), during a 3 hour period that MMS-1 was in the magnetosheath on 9 November 2019. White contours in panel (f) and (g) represent regions of high reduced magnetic helicity ($|\sigma_m| \geq 0.75$) and regions of low reduced cross helicity ($|\sigma_c| \leq 0.3$), respectively. The black curved line in panels (f)-(h) is the cone of influence.

duration between 30 seconds and 3 hours, and (iii) if the event was within the cone of influence, which arises because of finite data segment length (Torrence and Compo, 1998). I calculate reduced, normalized forms of magnetic helicity σ_m , cross helicity σ_c , and residual energy σ_r in 2400-point windows (~ 3 hours for MMS and ~ 2 hours for THEMIS) across the hours-long periods identified in the solar wind and magnetosheath. Figure 3.3 displays the spectrograms of reduced magnetic helicity from 10:20-13:30 UT and 11:05-14:05 UT on 9 November 2019. These intervals are calculated from the time series in Figure 3.2. Events identified with the wavelet analysis method are marked with a grey interval. The black contours represent event candidates with $|\sigma_m| \geq 0.75$ whereas the white contours indicate events that were established in the final event list. Inside the white contours, a white “X” marks the absolute local maximum, and the yellow annotations and dashed lines indicate the scale corresponding to a maximum. This scale is taken as the duration of the event, and the time of the peak in reduced σ_c is taken to the time-wise midpoint of the event. Therefore, the event interval start time will be the time of the peak in $|\sigma_m|$ minus half of the scale size of the peak. The events identified from this wavelet analysis can be further characterized by implementing the criteria that the events have (iv) corresponding cross helicity with absolute value less than 0.3, to ensure that there is low level of velocity fluctuations and/or (v) negative residual energy, which indicates that the magnetic energy is dominant.

It can be seen that not all grey event intervals have a white contour and marker for the maximum σ_c . This is because of the windowed analysis: as the

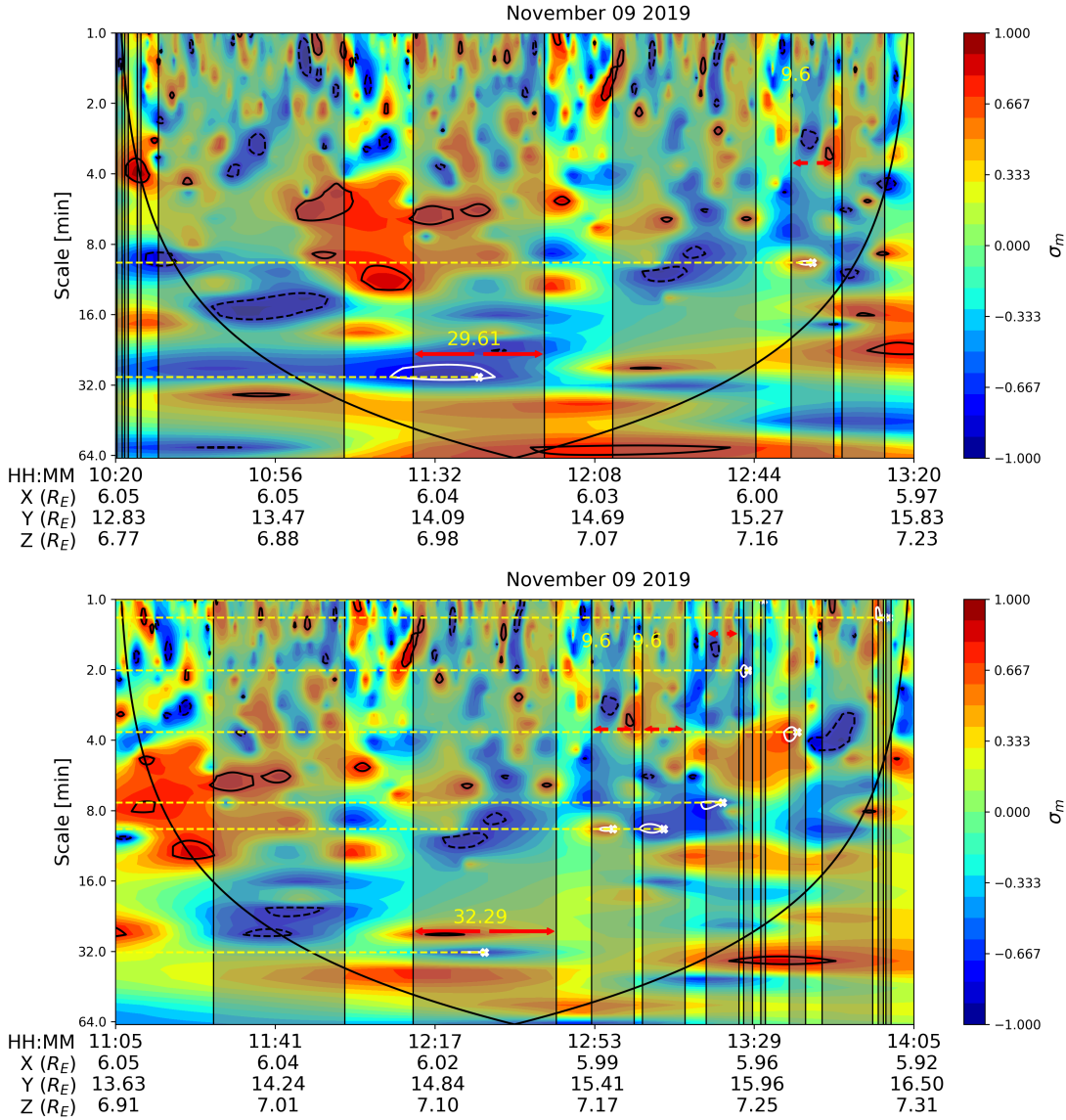


Figure 3.3: Spectrograms of reduced magnetic helicity over two overlapping 3-hour period from MMS-1 data on 9 November 2019. Demarcated intervals are identified events via wavelet analysis. Black contours represent regions of high reduced magnetic helicity ($|\sigma_m| \geq 0.75$). White contours represent regions of $|\sigma_m| \geq 0.75$ where the maximum inside the contour is an established event. Yellow dashed lines connect the maximum of the contour to the x-axis (scale) of the maximum. Red arrows indicate half of the scale (duration) on either side of the peak of σ_c . The black curved line is the cone of influence.

maxima in reduced magnetic helicity are recorded in each window, there will be overlapping events identified. The intervals in Figure 3.3 are overlapping by 600 data points (45 minutes for MMS data). After all the windows are searched, the compiled event list is then processed to eliminate overlapping events. By comparing two adjacently overlapping events and keeping the one with the highest maximum $|\sigma_m|$, this is repeated until there are no overlapping events left. Figure 3.4 shows an example of event intervals identified via the wavelet algorithm (with the criteria $|\sigma_m| \geq 0.75$) overlaid the corresponding time series and spectrogram of the reduced magnetic helicity in the magnetosheath during 9 November 2019. There are 11 events identified by the wavelet algorithm during this 3 hour period. The duration of these events range from 1 minute to 32.29 minutes, with an average duration of 9.913 minutes. The average maximum magnetic field of the events is 12.23 nT. The average absolute maximum (normalized) magnetic helicity of these 11 events is 0.83. 6 events in this period have $|\sigma_c| \leq 0.3$, and one of those events has $\sigma_r < 0$. Of remaining 5 events, none have $\sigma_r < 0$.

3.4 Event categorization

There were 4260 events identified from the wavelet analysis in the magnetosheath across 1051 hours. For the solar wind, there were 3193 events identified across 676 hours via wavelet analysis. The occurrence rate for events in the solar wind from the wavelet method is about 4.7 events/hour and for the magnetosheath the corresponding rate is about 4.0 events/hour. Table 3.1 summarizes the events identified with the wavelet analysis algorithm.

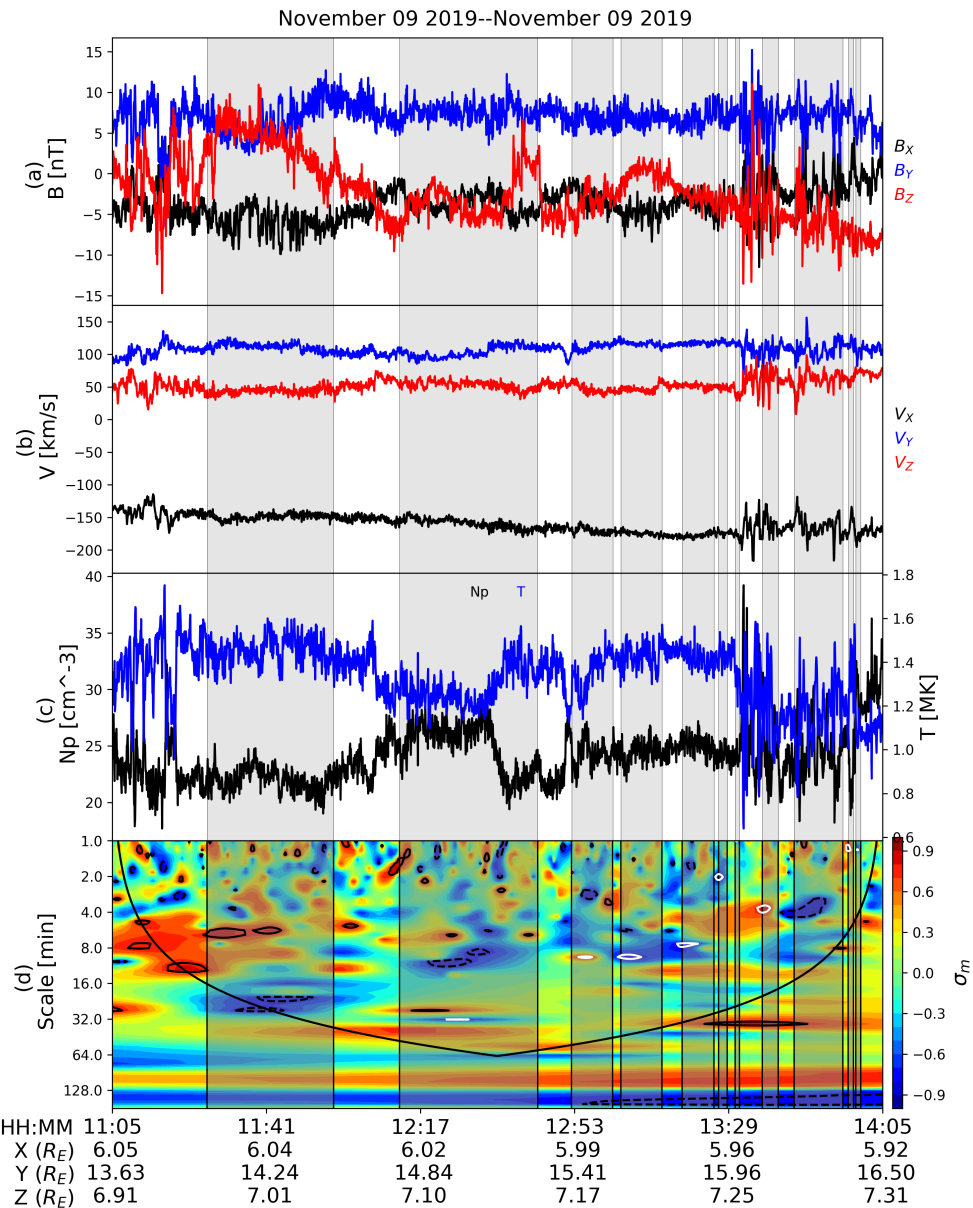


Figure 3.4: Portion of the 9 November 2019 time series and reduced magnetic helicity spectrogram. The grey intervals representing events identified with wavelet analysis meeting the criteria $|\sigma_m| \geq 0.75$.

Table 3.1: Summary table for identified events in the solar wind and magnetosheath via wavelet analysis as described in Section 3.3.

	Observation period [hrs]	Events	Event rate [#/hour]
<i>Solar wind</i>	676	3193	4.723
<i>Magnetosheath</i>	1051	4260	4.053

Properties of the magnetic structures are recorded during the identification process. Table 3.2 summarizes the statistical values for the identified events. The average duration of the events is 7.40 and 8.76 minutes for the solar wind and magnetosheath, respectively. In the solar wind, there are a large number of events with an average magnetic field of less than 10 nT, whereas in the magnetosheath there are relatively much fewer events with $\langle B \rangle < 10$ nT. The median magnetic field magnitude in the solar wind is 4.6 nT for events identified with wavelet analysis, and in the magnetosheath this number is 16.5 nT. As shown in Table 3.2, the duration of the events has similar ranges for the two regions. However, for the scale sizes of the events in the magnetosheath, they range from ~ 1507 km to 1.287×10^6 km, with a median and mean of 3.441×10^4 km, $\sim 5.4 R_E$ and 1.108×10^5 km, $\sim 17.4 R_E$, respectively. In the solar wind, the corresponding values are from 8975.2 km to 2.107×10^6 km, and a median (mean) of 5.444×10^5 (1.612×10^5) km, ~ 8.5 (25.3) R_E . It is important to note that the calculations of scale size cannot be considered as physically reliable as the calculations from the GS-based method since the specificity of the wavelet analysis identification

Table 3.2: Statistical values for the physical quantities of the structures identified in the magnetosheath (top) and solar wind (bottom) with wavelet analysis.

	Minimum	Maximum	Mean	Median	Std. Dev.
Duration [min]	0.517	59.221	8.761	2.617	12.6
Velocity [km/s]	13.653	567.539	220.381	214.361	75.4
Temperature [10^6 K]	0.601	31.611	2.908	2.200	2.3
$\langle B \rangle$ [nT]	2.344	85.790	20.213	16.473	12.2
Scale size [km]	1506.944	1.287×10^6	1.108×10^5	3.441×10^4	1.6×10^5
Duration [min]	0.560	59.221	7.402	2.400	10.6
Velocity [km/s]	235.264	664.001	367.580	342.591	87.4
Temperature [10^6 K]	0.114	16.946	2.600	0.685	3.4
$\langle B \rangle$ [nT]	0.543	29.372	4.935	4.576	2.5
Scale size [km]	8975.252	2.107×10^6	1.612×10^5	5.444×10^4	2.4×10^5

method relies on factors such as data segment length and choice of wavelet basis, in addition to the calculations being done in the spacecraft frame of reference.

Table 3.3 categorizes the events identified via wavelet analysis based on meeting certain MHD criteria. Over half of the events in the solar wind have characteristics of static flux ropes ($|\sigma_m| \geq 0.75$, $|\sigma_c| \leq 0.3$, $\sigma_r < 0$), whereas in the magnetosheath there are fewer events (approximately one-third) that meet these criteria. The distribution of the reduced cross helicity and residual energy

Table 3.3: Summary table of events meeting certain MHD criteria for events identified via wavelet analysis in the magnetosheath and solar wind.

	Solar wind	Magnetosheath
$ \sigma_m \geq 0.75$	3193	4260
$ \sigma_m \geq 0.75, \sigma_c \leq 0.3$	1821	2490
$ \sigma_m \geq 0.75, \sigma_r < 0$	2156	2468
$ \sigma_m \geq 0.75, \sigma_c \leq 0.3, \sigma_r < 0$	1144	1567

for all identified events in the solar wind and magnetosheath is shown in Figure 3.5. The histogram shows the averaged, reduced MHD quantities of the events identified by the wavelet method. Figure 3.5 shows flatter distributions of reduced cross helicity σ_c in the magnetosheath than in the solar wind. The reduced cross helicity distribution maintains a peak around $\sigma_c = 0$ in both regions in Figure 3.5, with the solar wind having a steeper shape. The reduced residual energy has a peak at $\sigma_r = -1$, with values that are nearly evenly distributed between $(-1, 1)$.

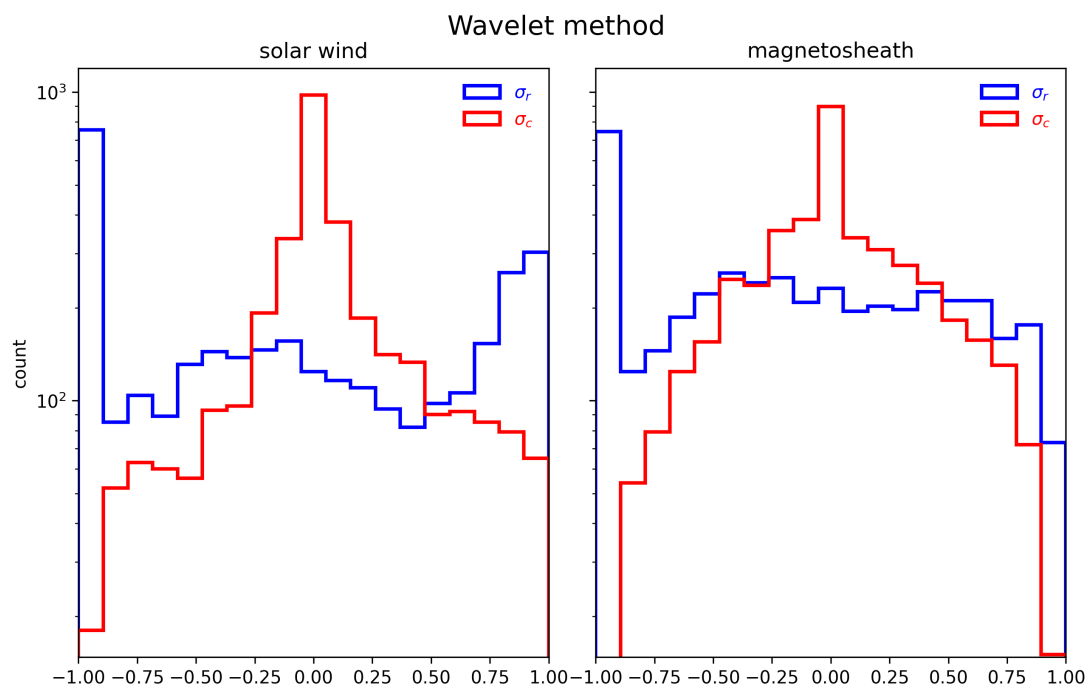


Figure 3.5: Histograms of reduced cross helicity σ_c (red) and reduced residual energy σ_r (blue) for all solar wind (left) and magnetosheath events (right) identified via the wavelet method.

Chapter 4. Grad-Shafranov reconstruction and automated identification algorithm

4.1 The Grad-Shafranov equation

The Grad-Shafranov (GS) equation describes the force balance between the Lorentz force and the gradient of the thermal pressure p (Sonnerup and Guo, 1996; Hau and Sonnerup, 1999) in two spatial dimensions (x, y) with $\frac{\partial}{\partial z} = 0$, as given below,

$$\nabla^2 A = \frac{\partial^2 A}{\partial x^2} + \frac{\partial^2 A}{\partial y^2} = -\mu_0 \frac{dP_t}{dA} = -\mu_0 \frac{d}{dA} \left(p + \frac{B_z^2}{2\mu_0} \right). \quad (4.1)$$

Here, A is the magnetic scalar potential, or the magnetic flux function, B_z is the z -component of the magnetic field, and P_t is the transverse pressure (thermal plus axial magnetic pressure).

4.1.1 Derivation of the original GS equation

Starting with the magnetic field expressed by the magnetic vector potential and balancing the gradient of the pressure with the Lorentz force in 2D ($\frac{\partial}{\partial z} = 0$),

$$\mathbf{B} = \nabla \times \mathbf{A} = \nabla A_z \times \hat{z} + B_z \hat{z} \quad (4.2)$$

$$\nabla p = \mathbf{j} \times \mathbf{B} = j_z \hat{z} \times \mathbf{B}_\perp + \mathbf{j}_\perp \times B_z \hat{z} \quad (4.3)$$

Using Ampere's law to determine the components of the current density \mathbf{j} ,

$$\begin{aligned} \nabla \times \mathbf{B} &= \mu_0 \mathbf{j} \\ \nabla \times (\nabla \times \mathbf{A}) &= \mu_0 \mathbf{j} \\ \nabla \times [\nabla A_z \times \hat{z} + B_z \hat{z}] &= \mu_0 [j_z \hat{z} + \mathbf{j}_\perp] \end{aligned} \quad (4.4)$$

The \hat{z} and perpendicular components of the current density are then found by,

$$\begin{aligned} \mu_0 j_z \hat{z} &= \nabla \times (\nabla A_z \times \hat{z}) \\ &= (\nabla \cdot \hat{z}) \nabla A_z - (\nabla \cdot \nabla A_z) \hat{z} \\ j_z \hat{z} &= -\frac{1}{\mu_0} \nabla^2 A_z \hat{z} \end{aligned} \quad (4.5)$$

$$\begin{aligned} \mu_0 \mathbf{j}_\perp &= \nabla \times B_z \hat{z} \\ \mathbf{j}_\perp &= \frac{1}{\mu_0} \nabla B_z \times \hat{z} \end{aligned} \quad (4.6)$$

Simplifying the \hat{z} and perpendicular terms of the pressure gradient (4.3),

$$\begin{aligned} j_z \hat{z} \times \mathbf{B}_\perp &= -\frac{1}{\mu_0} \nabla^2 A_z \hat{z} \times (\nabla A_z \times \hat{z}) \\ &= -\frac{1}{\mu_0} [(\nabla^2 A_z \hat{z} \cdot \hat{z}) \nabla A_z - (\nabla^2 A_z \hat{z} \cdot \nabla A_z) \hat{z}] \\ &= -\frac{1}{\mu_0} (\nabla^2 A_z) \nabla A_z \end{aligned} \quad (4.7)$$

$$\begin{aligned}
\mathbf{j}_\perp \times B_z \hat{z} &= \left(\frac{1}{\mu_0} \nabla B_z \times \hat{z} \right) \times B_z \hat{z} \\
&= \frac{1}{\mu_0} [(B_z \hat{z} \cdot \nabla B_z) \hat{z} - (B_z \hat{z} \cdot \nabla B_z) \hat{z}] \\
&= -\frac{1}{\mu_0} B_z \nabla B_z
\end{aligned} \tag{4.8}$$

and substituting them into the respective right hand side of (4.3):

$$\begin{aligned}
\nabla p &= -\frac{1}{\mu_0} (\nabla^2 A_z) \nabla A_z - \frac{1}{\mu_0} B_z \nabla B_z \\
(\nabla^2 A_z) \nabla A_z &= -\mu_0 \left(\nabla p + \frac{1}{\mu_0} B_z \nabla B_z \right) \\
(\nabla^2 A_z) \nabla A_z &= -\mu_0 \left(\frac{dp}{dA_z} \nabla A_z + \frac{1}{\mu_0} B_z \frac{dB_z}{dA_z} \nabla A_z \right) \\
\nabla^2 A_z &= -\mu_0 \left(\frac{dp}{dA_z} + \frac{1}{\mu_0} \frac{dB_z}{dA_z} \right)
\end{aligned}$$

Replacing A with A_z for the sake of simplicity, we arrive at the form for the Grad-Shafranov equation (4.1),

$$\nabla^2 A = -\mu_0 \frac{d}{dA} \left(p + \frac{B_z^2}{2\mu_0} \right). \tag{4.9}$$

4.1.2 Derivation of the extended GS equation

The implementation by Chen et al. (2021) utilizes the extended GS method, which still seeks to find the double-folding pattern between two $P'_t(A')$ versus A' curves, but with $A' = (1 - \alpha)A$ and $P'_t = (1 - \alpha)p + (1 - \alpha)^2 \frac{B_z^2}{2\mu_0} + \alpha(1 - \alpha) \frac{B^2}{2\mu_0}$. The factor α is a proportionality constant, which for a field-aligned flow is the average Alfvén Mach number squared, $\alpha = \langle M_A \rangle^2 \approx \text{const}$ in a frame of reference

moving with the structure governed by the GS equation. The extended GS (or GS-type) equation (Teh, 2018; Sonnerup et al., 2006) is:

$$\nabla^2 A' = -\mu_0 \frac{d}{dA'} \left[(1-\alpha)p + (1-\alpha)^2 \frac{B_z^2}{2\mu_0} + \alpha(1-\alpha) \frac{B^2}{2\mu_0} \right] \quad (4.10)$$

which simplifies to the original GS equation (4.1) when $\alpha \equiv 0$. The extended GS method allows us to identify structures with significant remaining plasma flow aligned with the local magnetic field in a proper frame of reference (Chen and Hu, 2022). For a structure with a field-aligned flow, the momentum equation is

$$\begin{aligned} -\nabla p \times \mathbf{j} \times \mathbf{B} &= \rho \left[\frac{\nabla v^2}{2} - \mathbf{v} \times (\nabla \times \mathbf{v}) \right] \\ \rho (\nabla \times \mathbf{v}) \times \mathbf{v} - \mathbf{j} \times \mathbf{B} &= -\nabla p - \rho \frac{\nabla v^2}{2}. \end{aligned} \quad (4.11)$$

Expanding the left hand side of (4.11), it becomes

$$\begin{aligned} &\rho (\nabla \times \mathbf{v}) \times \mathbf{v} - \frac{1}{\mu_0} (\nabla \times \mathbf{B}) \times \mathbf{B} \\ &\rho [-\nabla \mathbf{v} \cdot \mathbf{v} + (\mathbf{v} \cdot \nabla) \mathbf{v}] + \frac{1}{\mu_0} [\nabla \mathbf{B} \cdot \mathbf{B} - (\mathbf{B} \cdot \nabla) \mathbf{B}] \\ &\rho [-\nabla \mathbf{v} \cdot \mathbf{v} + \nabla \cdot (\mathbf{v} \mathbf{v}) - (\nabla \cdot \mathbf{v}) \mathbf{v}] + \frac{1}{\mu_0} [\nabla \mathbf{B} \cdot \mathbf{B} - \nabla \cdot (\mathbf{B} \mathbf{B}) + (\nabla \cdot \mathbf{B}) \mathbf{B}] \\ &\rho [-\nabla \mathbf{v} \cdot \mathbf{v} + \nabla \cdot (\mathbf{v} \mathbf{v})] + \frac{1}{\mu_0} [\nabla \mathbf{B} \cdot \mathbf{B} - \nabla \cdot (\mathbf{B} \mathbf{B})] \end{aligned}$$

since $(\nabla \cdot \mathbf{B}) = 0$ and $(\nabla \cdot \mathbf{v}) = 0$. Substituting $v^2 = \frac{M_A B^2}{\rho \mu_0}$ into $\rho \nabla \mathbf{v} \cdot \mathbf{v}$, we get

$$\begin{aligned}\rho \nabla \mathbf{v} \cdot \mathbf{v} &= \rho \nabla \left(\frac{M_A \mathbf{B}}{\sqrt{\mu_0 \rho}} \right) \cdot \left(\frac{M_A \mathbf{B}}{\sqrt{\mu_0 \rho}} \right) \\ &= \frac{1}{\mu_0} [(M_A \nabla \mathbf{B} + \mathbf{B} \nabla M_A) \cdot \mathbf{B} M_A] \\ &= \frac{1}{\mu_0} (M_A^2 \nabla \mathbf{B} \cdot \mathbf{B} + B^2 M_A \nabla M_A).\end{aligned}$$

The left hand side of (4.11) then becomes

$$\begin{aligned}\nabla \cdot (\rho \mathbf{v} \mathbf{v}) - \frac{1}{\mu_0} (M_A^2 \nabla \mathbf{B} \cdot \mathbf{B} + \mathbf{B} M_A^2 \cdot \nabla M_A) + \frac{1}{\mu_0} (\nabla \mathbf{B} \cdot \mathbf{B}) - \frac{1}{\mu_0} \nabla \cdot (\mathbf{B} \mathbf{B}) \\ &= \nabla \cdot \left(\rho \mathbf{v} \mathbf{v} - \frac{\mathbf{B} \mathbf{B}}{\mu_0} \right) + \frac{1}{\mu_0} (1 - M_A^2) (\nabla \mathbf{B} \cdot \mathbf{B}) - \frac{1}{\mu_0} B^2 M_A \nabla M_A \\ &= \nabla \cdot \left(\frac{M_A^2}{\mu_0} \mathbf{B} \mathbf{B} - \frac{1}{\mu_0} \mathbf{B} \mathbf{B} \right) + \frac{1}{\mu_0} (1 - M_A^2) (\nabla \mathbf{B} \cdot \mathbf{B}) - \frac{1}{\mu_0} B^2 M_A \nabla M_A \\ &= \frac{1}{\mu_0} \nabla \cdot [(M_A^2 - 1) \mathbf{B} \mathbf{B}] + \frac{1}{\mu_0} (1 - M_A^2) (\nabla \mathbf{B} \cdot \mathbf{B}) - \frac{1}{\mu_0} B^2 M_A^2 \nabla M_A.\end{aligned}$$

Making the same substitution of $v^2 = \frac{M_A B^2}{\rho \mu_0}$ on the right hand side of (4.11),

$$\begin{aligned}-\nabla p - \rho \frac{\nabla v^2}{2} &= -\nabla p - \frac{\rho}{2} \nabla \left(\frac{M_A^2 B^2}{\rho \mu_0} \right) \\ &= -\nabla p - \frac{1}{2 \mu_0} (M_A^2 \nabla B^2 + B^2 \nabla M_A^2),\end{aligned}$$

and combining all of the terms yields

$$\begin{aligned}
& \frac{1}{\mu_0} \nabla \cdot [(M_A^2 - 1) \mathbf{B} \mathbf{B}] + \frac{1}{\mu_0} (1 - M_A^2) (\nabla \mathbf{B} \cdot \mathbf{B}) - \frac{1}{\mu_0} B^2 M_A \nabla M_A \\
&= -\nabla p - \frac{1}{2\mu_0} (M_A^2 \nabla B^2 + B^2 \nabla M_A^2) \\
& \frac{1}{\mu_0} \nabla \cdot [(M_A^2 - 1) \mathbf{B} \mathbf{B}] + \frac{1}{2\mu_0} (1 - M_A^2) \nabla B^2 - \frac{1}{2\mu_0} B^2 \nabla M_A^2 \\
&= -\nabla p - \frac{1}{2\mu_0} (M_A^2 \nabla B^2 + B^2 \nabla M_A^2) \\
& \frac{1}{\mu_0} \nabla \cdot [(M_A^2 - 1) \mathbf{B} \mathbf{B}] = -\nabla p - \frac{1}{2\mu_0} \nabla B^2.
\end{aligned}$$

The Alfvén Mach number squared can be simplified to $\alpha = M_A^2$:

$$\nabla \cdot [(1 - \alpha) \mathbf{B} \mathbf{B}] = \mu_0 \nabla \left(p + \frac{B^2}{2\mu_0} \right). \quad (4.12)$$

Taking another substitution, $\mathbf{C} = (1 - \alpha) \mathbf{B}$, the right hand side of (4.12) is expanded to

$$\begin{aligned}
\mu_0 \nabla \left(p + \frac{B^2}{2\mu_0} \right) &= \nabla \cdot (\mathbf{C} \mathbf{B}) \\
&= (\nabla \cdot \mathbf{C}) \mathbf{B} + (\mathbf{B} \cdot \nabla) \mathbf{C} \\
&= (\nabla \mathbf{C}) \cdot \mathbf{B} - \mathbf{B} \times (\nabla \times \mathbf{C}) \\
&= \nabla [(1 - \alpha) \mathbf{B}] \cdot \mathbf{B} - \mathbf{B} \times (\nabla \times \mathbf{C}) \\
&= -\nabla \alpha (\mathbf{B} \cdot \mathbf{B}) + (1 - \alpha) \nabla \mathbf{B} \cdot \mathbf{B} - \mathbf{B} \times (\nabla \times \mathbf{C}) \\
&= (1 - \alpha) \nabla \left(\frac{B^2}{2} \right) - B^2 \nabla \alpha - \mathbf{B} \times (\nabla \times \mathbf{C}) \\
&= \nabla \left[(1 - \alpha) \frac{B^2}{2} \right] - \frac{B^2}{2} \nabla \alpha - \mathbf{B} \times (\nabla \times \mathbf{C}).
\end{aligned}$$

Therefore, (4.12) becomes

$$\begin{aligned}\mu_0 \left[\nabla \left(p + \frac{B^2}{2\mu_0} - (1-\alpha) \frac{B^2}{2\mu_0} \right) + \frac{B^2}{2\mu_0} \nabla \alpha \right] &= -\mathbf{B} \times (\nabla \times \mathbf{C}) \\ \mu_0 \left[\nabla \left(p + \alpha \frac{B^2}{2\mu_0} \right) + \frac{B^2}{2\mu_0} \nabla \alpha \right] &= -\mathbf{B} \times (\nabla \times \mathbf{C}).\end{aligned}\quad (4.13)$$

By breaking down \mathbf{B} and \mathbf{C} into their components, and noting that $\mathbf{B}_t \times (\nabla \times \mathbf{C})_t = 0$ because there is no z -component of the gradient ($\frac{\partial}{\partial z} = 0$), the triple cross product $\mathbf{B} \times (\nabla \times \mathbf{C})$ becomes

$$\begin{aligned}\mathbf{B} \times (\nabla \times \mathbf{C}) &= (\mathbf{B}_t + B_z \hat{z}) \times [(\nabla \times \mathbf{C})_t + (\nabla \times \mathbf{C})_z] \\ &= \mathbf{B}_t \times (\nabla \times \mathbf{C})_z + B_z \hat{z} \times (\nabla \times \mathbf{C})_t \\ &= (\nabla A_z \times \hat{z}) \times (\nabla \times \mathbf{C})_z + B_z \hat{z} \times (\nabla C_z \times \hat{z}) \\ &= -(\nabla \times \mathbf{C})_z \nabla A_z + B_z \nabla C_z.\end{aligned}$$

Making use of $\nabla \cdot \mathbf{C} = 0$,

$$\begin{aligned}\nabla \cdot \mathbf{C} &= \nabla \cdot [(1-\alpha) (\nabla \times \mathbf{A})] = 0 \\ (1-\alpha) \nabla \cdot (\nabla \times \mathbf{A}) + (\nabla \times \mathbf{A}) \cdot \nabla (1-\alpha) &= 0 \\ -(\nabla A_z \times \hat{z}) \cdot \nabla \alpha &= \nabla A_z \cdot \nabla \alpha = 0\end{aligned}$$

the term $(\nabla \times \mathbf{C})_z$ can be written as

$$\begin{aligned}
(\nabla \times \mathbf{C})_z &= \nabla \times (1 - \alpha) \mathbf{B}_t \\
&= \nabla \times [(1 - \alpha) (\nabla \times \mathbf{A})_t] \\
&= -\nabla \alpha \times (\nabla A_z \times \hat{z}) + (1 - \alpha) \nabla \times (\nabla A_z \times \hat{z}) \\
&= -(\nabla \alpha \cdot \hat{z}) \nabla A_z + (\nabla \alpha \cdot \nabla A_z) \hat{z} + (1 - \alpha) [(\nabla \cdot \hat{z}) \nabla A_z - (\nabla \cdot \nabla A_z) \hat{z}] \\
&= -(1 - \alpha) \nabla^2 A_z \hat{z}.
\end{aligned}$$

The $B_z \nabla C_z$ term can be written as

$$\begin{aligned}
B_z \nabla C_z &= B_z \nabla [(1 - \alpha) B_z] \\
&= B_z [B_z \nabla (1 - \alpha) + (1 - \alpha) \nabla B_z] \\
&= -B_z^2 \nabla \alpha + (1 - \alpha) \nabla \left(\frac{B_z^2}{2} \right) \\
&= -B_z^2 \nabla \alpha + \nabla \left[(1 - \alpha) \frac{B_z^2}{2} \right] + \frac{B_z^2}{2} \nabla \alpha \\
&= \frac{1}{2} \nabla [(1 - \alpha) B_z^2] - \frac{B_z^2}{2} \nabla \alpha,
\end{aligned}$$

which leads to the form of $\mathbf{B} \times (\nabla \times \mathbf{C})$ that we insert into (4.13):

$$-\mathbf{B} \times (\nabla \times \mathbf{C}) = -[(1 - \alpha) \nabla^2 A_z] \nabla A_z - \frac{1}{2} \nabla [(1 - \alpha) B_z^2] + \frac{B_z^2}{2} \nabla \alpha. \quad (4.14)$$

Once again replacing $A = A_z$ for simplicity, (4.13) becomes

$$\begin{aligned}\mu_0 \left[\nabla \left(p + \alpha \frac{B^2}{2\mu_0} \right) + \frac{B^2}{2\mu_0} \nabla \alpha \right] &= - \left[(1 - \alpha) \nabla^2 A \right] \nabla A - \frac{1}{2} \nabla \left[(1 - \alpha) B_z^2 \right] + \frac{B_z^2}{2} \nabla \alpha \\ \mu_0 \nabla \left[p + \alpha \frac{B^2}{2\mu_0} + (1 - \alpha) \frac{B_z^2}{2\mu_0} \right] &= - \left[(1 - \alpha) \nabla^2 A \right] \nabla A + \left(\frac{B_z^2 - B^2}{2} \right) \nabla \alpha \\ \mu_0 \nabla A \frac{d}{dA} \left[p + \alpha \frac{B^2}{2\mu_0} + (1 - \alpha) \frac{B_z^2}{2\mu_0} \right] &= - \left[(1 - \alpha) \nabla^2 A \right] \nabla A + \left(\frac{B_z^2 - B^2}{2} \right) \nabla A \frac{d\alpha}{dA}.\end{aligned}$$

The ∇A term is then eliminated, and both sides are multiplied by $(1 - \alpha)$:

$$\begin{aligned}\mu_0 \frac{d}{dA} \left[p + \alpha \frac{B^2}{2\mu_0} + (1 - \alpha) \frac{B_z^2}{2\mu_0} \right] &= - (1 - \alpha) \nabla^2 A + \left(\frac{B_z^2 - B^2}{2} \right) \frac{d\alpha}{dA} \\ \mu_0 (1 - \alpha) \frac{d}{dA} \left[p + \alpha \frac{B^2}{2\mu_0} + (1 - \alpha) \frac{B_z^2}{2\mu_0} \right] &= - (1 - \alpha)^2 \nabla^2 A + (1 - \alpha) \left(\frac{B_z^2 - B^2}{2} \right) \frac{d\alpha}{dA} \\ \mu_0 \frac{d}{dA} \left[(1 - \alpha) \left(p + \alpha \frac{B^2}{2\mu_0} + (1 - \alpha) \frac{B_z^2}{2\mu_0} \right) \right] + \mu_0 \frac{d\alpha}{dA} \left[p + \alpha \frac{B^2}{2\mu_0} + (1 - \alpha) \frac{B_z^2}{2\mu_0} \right] &= - (1 - \alpha)^2 \nabla^2 A + (1 - \alpha) \left(\frac{B_z^2 - B^2}{2} \right) \frac{d\alpha}{dA} \\ \mu_0 \frac{d}{dA} \left[(1 - \alpha) p + \alpha (1 - \alpha) \frac{B^2}{2\mu_0} + (1 - \alpha)^2 \frac{B_z^2}{2\mu_0} \right] + \mu_0 \frac{d\alpha}{dA} \left[p + \frac{B^2}{2\mu_0} \right] &= - (1 - \alpha)^2 \nabla^2 A.\end{aligned}$$

The transverse pressure P'_t is $(1 - \alpha)p + \alpha(1 - \alpha)\frac{B^2}{2\mu_0} + (1 - \alpha)^2\frac{B_z^2}{2\mu_0}$, therefore substituting $A' = (1 - \alpha)A$ and taking the special case $\alpha \equiv const.$, we arrive at

$$\begin{aligned}\mu_0 \frac{dP'_t}{dA} &= -(1 - \alpha)^2 \nabla^2 A \\ \mu_0 \frac{dP'_t}{dA'} \frac{dA'}{dA} &= -(1 - \alpha) \nabla^2 A' \\ \mu_0 (1 - \alpha) \frac{dP'_t}{dA'} &= -(1 - \alpha) \nabla^2 A' \quad (4.15) \\ \mu_0 \frac{dP'_t}{dA'} &= -\nabla^2 A' \\ \mu_0 \frac{d}{dA'} \left[(1 - \alpha)p + \alpha(1 - \alpha)\frac{B^2}{2\mu_0} + (1 - \alpha)^2\frac{B_z^2}{2\mu_0} \right] &= -\nabla^2 A',\end{aligned}$$

which is the extended form used in the GS-based reconstruction and detection of SFRs with significant remaining flow.

4.2 Automated GS-based detection of SFRs

In both the original and the GS-type equations, the transverse pressure P_t , and its equivalent P'_t , are single variable functions of the magnetic flux function A (A' for the GS-type with $\alpha \equiv const$). With this feature, one can recover the 2D cross-section of a flux rope structure from the 1D spacecraft data by solving the initial value problem based on the GS equation, i.e., by carrying out the GS reconstruction procedures (Hau and Sonnerup, 1999; Hu and Sonnerup, 2002; Hu, 2017). The GS-based techniques in this study consist of the GS-type reconstruction and the extended GS-based automated detection. Considering the complicated environment from the solar wind to the magnetosheath, the GS-type reconstruction is adopted in this study for selected events.

A cross section of a cylindrical flux rope structure is fully characterized by the 2D scalar flux function $A(x, y)$, and the field-line invariants (B_z, J_z, p, P_t) vary among the nested cylindrical flux surfaces while remaining constant on each distinct surface with a distinct A value (Hu et al., 2018). As a spacecraft passes through the cross section of a magnetic flux rope with closed transverse field lines, it crosses the same set of magnetic field lines twice, the second time being in reverse order as the first half of the crossing. Therefore, the measured magnetic flux function A associated with the field lines traversed by the spacecraft is double-folded, meaning there is a turning point at which an extremum in A is reached. These features, especially the double-folding pattern, are the basis for the GS reconstruction-based identification algorithm (Hu et al., 2018). Figure 4.1 shows schematic diagram of a reconstruction of a magnetic cloud event and the associated flux rope structure. Figure 4.2 displays the reconstruction of a magnetic cloud event from spacecraft data using the GS-reconstruction algorithm (Hu et al., 2015, 2018). The cross section and its relation to the magnetic field lines of the flux rope structure. A more detailed description of the implementation (Hu et al., 2018), including a flowchart of the flux rope detection algorithm, can be found in Appendix B, and online¹.

The GS-based algorithm starts by moving a window continually through an entire data segment with variable window sizes in turn, ranging from the minimum duration of approximately 10 data points with cadence Δt , i.e. $10\Delta t$, to the maximum duration of 343 data points to cover a wide range of SFR duration,

¹fluxrope.info/flowchart.html

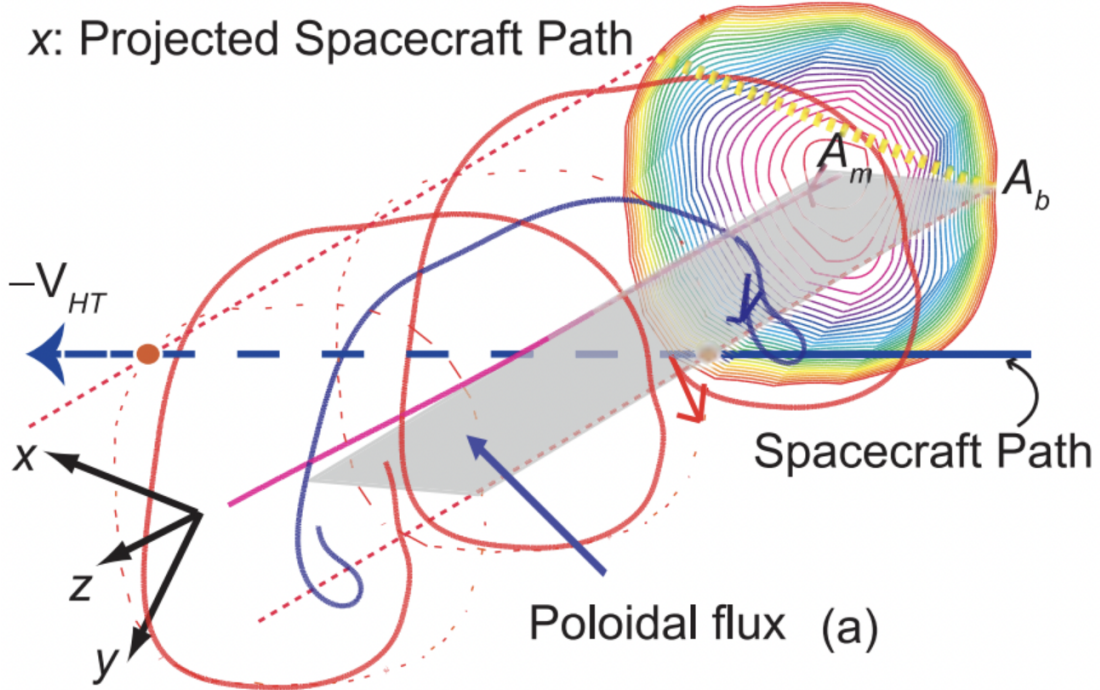


Figure 4.1: View of a reconstruction for a magnetic cloud event as a spacecraft passes through it (Hu, 2017). The 2D cross section and selected associated magnetic field lines (red and blue twisted lines) are shown along the flux rope axis (z -axis). The variables A_m and A_b mark the magnetic flux function A at the center and boundary, respectively, of the reconstruction result. The poloidal flux and axial flux can also be obtained through the reconstruction algorithm.

while taking into account limited computing resources. The maximum duration corresponds to approximately 17 minutes for the THEMIS data, and 25 minutes for the MMS data. The in situ magnetic field and plasma data from a specified window of time are first transformed into the co-moving frame, notably the de Hoffmann-Teller frame (de Hoffmann and Teller, 1950). Through a trial-and-error process, the optimal orientation of the z -axis is determined. A trial z -axis is represented by the azimuthal and polar angles, ϕ and θ , in the GSE coordinate

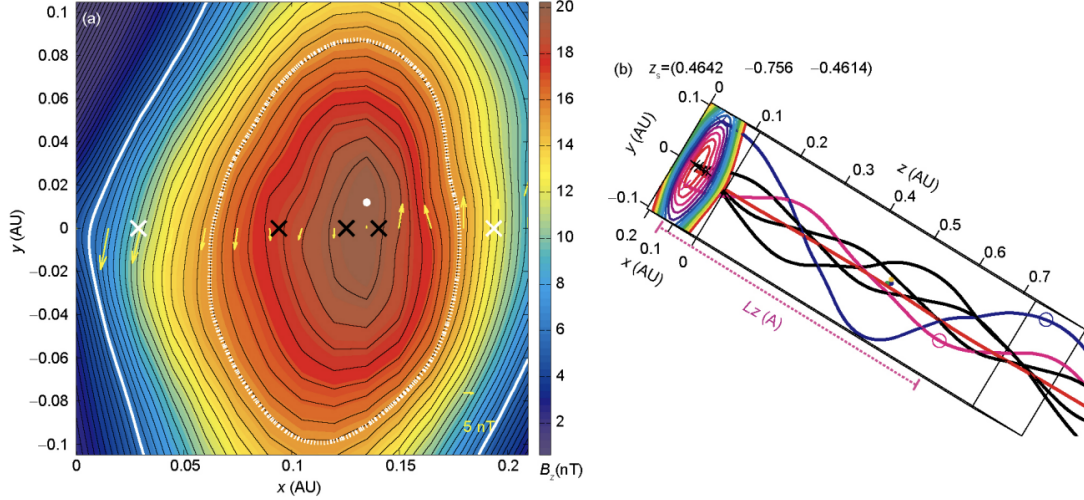


Figure 4.2: Reconstruction of a magnetic cloud (Hu et al., 2015): a) 2D cross section of $A(x, y)$ for a reconstructed magnetic cloud event. The black lines indicate the transverse magnetic field lines, and the color bar indicates the axial field lines B_z . The yellow arrows denote the transverse field lines (B_t) along the path of the spacecraft ($y = 0$). The white contour indicates the area of the reconstruction done from spacecraft data ($A = A_b$), while the area outside the white contour is reconstructed from extrapolation. b) 3D view of a flux rope structure for the magnetic cloud event, showing the 2D cross section (A') and selected associated twisted magnetic field lines along the flux rope axis (denoted at the top). The black field lines rooted at the foot points where the electron onsets were observed. The pink and blue circles denote the locations where the associated field lines complete a full turn around the z -axis.

system. The azimuthal angle ϕ is the longitude of the SFR z -axis, which measures the angle between the GSE X -direction and the projection of the z -axis onto the XY -plane. The polar angle θ is the angle between the SFR z -axis and the Z -direction. The trial values for ϕ and θ are selected, and the transverse pressure P'_t along the spacecraft path is calculated, as shown in Equation (4.10). The plot of P'_t versus A' may have a turning point where P'_t along the spacecraft path splits into two parts, with an extreme A' value near this turning point, typically for an SFR structure. This is where the magnetic field B_y component changes

sign because of the field line geometry of a helical structure. To search for the double-folding of P'_t versus A' , the line integral of B_y along the spacecraft path ($y = 0$) is evaluated:

$$A'(x, 0) = - \int_0^x (1 - \alpha) B_y(x', 0) dx'. \quad (4.16)$$

Figure 4.3 represents such a P'_t versus A' plot, with two distinct portions joining near a turning point with a minimum A' value. The quality of the folding (or overlapping) of the two parts of P'_t versus A' is evaluated by two metrics, R_{diff} (the point-wise difference residue between the two parts) and R_{fit} (a residue of the fitting function $P'_t(A')$ as illustrated by the solid black curve). These metrics are used to check how well the two parts fold onto each other, provided that such a turning point exists. The threshold conditions, $R_{diff} \lesssim 0.2$ and $R_{fit} \lesssim 0.2$ for these metrics, are selected empirically to guarantee good double-folding quality (Hu et al., 2018). The optimal orientation of the z -axis of the SFRs is found by going through iterations of ϕ and θ until the minimum residue values are found. Once the minimum residues satisfying the threshold conditions are found, the corresponding optimal z -axis orientation and event interval are recorded as an SFR candidate.

After the initial detection of SFR candidates, the list of initial candidates is refined. The records are further classified based on the Walén test slope w , which is the slope of the linear regression between $\mathbf{V}_{\text{sw}} - \mathbf{V}_{\text{HT}}$ and $\mathbf{V}_{\mathbf{A}}$. Records with $|w| \leq 0.3$ are quasi-static SFRs and thus saved directly. Records with $|w| > 0.3$, except for when the correlation coefficient r between the aforementioned two

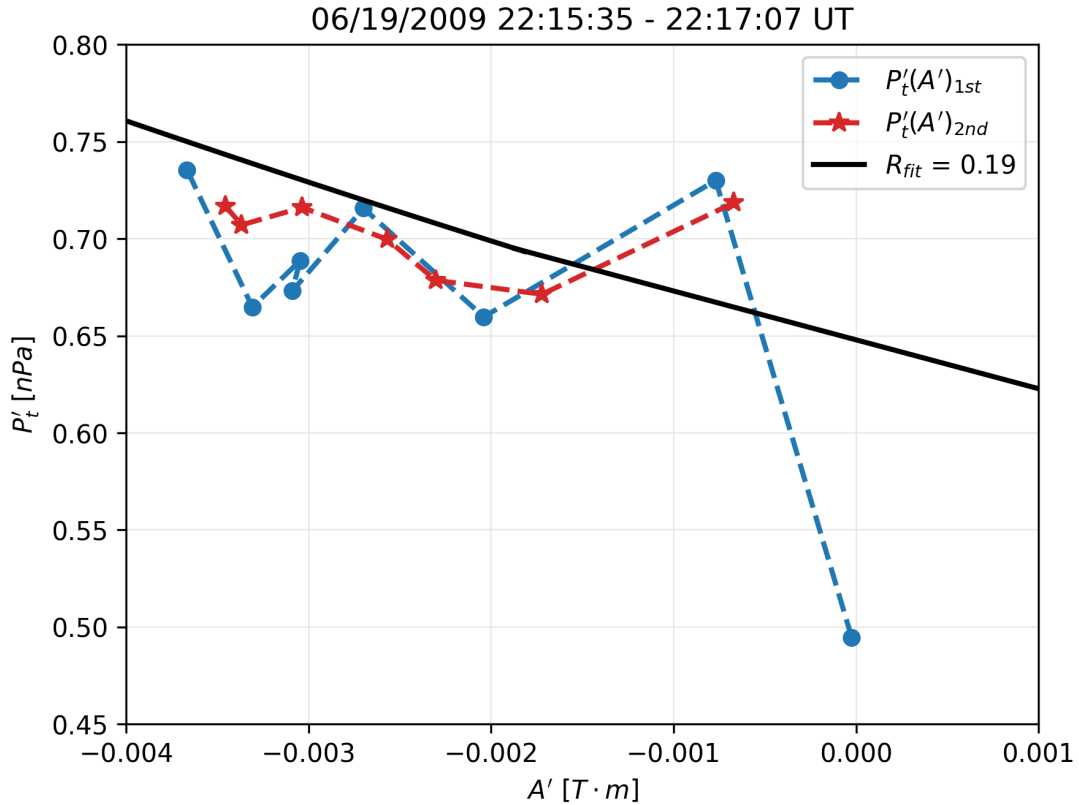


Figure 4.3: The P'_t versus A' plot for an SFR interval from 22:15:35-22:17:05 UT on 19 June 2009 observed by THM-C. The data points are marked by the symbols, and are connected by the blue dashed line and the red dashed line, separated by the turning point at the minimum of A' in this case. The two lines correspond to the first and second parts of the $P'_t(A')$ curve as denoted by the legend. The solid black curve represents a functional fitting to the data points with fitting residue R_{fit} .

velocities ($\mathbf{V}_{\text{sw}} - \mathbf{V}_{\text{HT}}$ and \mathbf{V}_A) is $|r| \geq 0.8$ and $\langle M_A \rangle \leq 0.9$, are removed. These conditions ensure that the remaining plasma flow is aligned with the local magnetic field, and also to avoid a singularity in Equation (4.10) at $\alpha = 1$. Events with $\alpha > 1$ are rare, but they are also removed, so that the events remaining are sub-Alfvénic. The algorithm also removes events from the initial candidate list if the candidates have a turning point within $5\Delta t$ (turn time) of the turning point of another candidate with a smaller R_{diff} , as these could be the same overlapping structures. Table 4.1 lays out the threshold conditions as utilized in the post-processing of the GS-based detection event list (Chen et al., 2020, 2021; Chen and Hu, 2022).

Table 4.1: Table of threshold conditions for GS reconstruction-based algorithm. R_{diff} and R_{fit} are residues which ensure good double-folding quality in the $P'_t(A')$ vs. A' curve..

Duration	R_{diff}	R_{fit}	Turn time	Walén test slope	$ r $	$\langle M_A \rangle$
$10\Delta t$ - $343\Delta t$	< 0.2	< 0.2	$5\Delta t$	$ w \leq 0.3$		
$10\Delta t$ - $343\Delta t$	< 0.2	< 0.2	$5\Delta t$	$ w > 0.3$	≥ 0.8	≤ 0.9

The duration of the search windows does not exceed $343\Delta t$ (~ 25.733 minutes for MMS and ~ 24.553 minutes for THEMIS) due to computational time constraints. The detection algorithm was performed for some time periods with search window size up to 388 points in duration; however, the search yielded very few (generally less than 3) additional event counts after the post-processing steps. This was due to the step of making sure there is no overlap between SFR

candidates, which prioritizes smaller duration candidates. Therefore, with the search algorithm taking a significant amount of time to run for longer search windows and yielding very few results, it was decided to stop the search at the maximum window size of $343\Delta t$.

The PyGS software (Zheng and Hu, 2018; Hu et al., 2018; Chen and Hu, 2022; Sonnerup and Guo, 1996; Hau and Sonnerup, 1999; Hu and Sonnerup, 2002) was used to reconstruct the 2D cross-sections and search for the folding patterns in the P'_t versus A' plot. Some modifications to the post-processing portion of the search algorithm were made in order to adhere to the magnetosheath environment. In one step of the post-processing algorithm, SFR candidates containing shocks (and other discontinuities) identified by various spacecraft (see PyGS documentation at <https://github.com/PyGSDR/PyGS>) are removed. Because the behavior of plasma in the magnetosheath is highly turbulent, removing SFR candidates with discontinuities would not be appropriate.

4.3 2D reconstructions of cross-sections

Figures 4.4 and 4.5 are examples of the reconstruction of 2D cross-sections of selected flux rope events, both in the magnetosheath. The black lines indicate the transverse magnetic field lines, and the color background indicates the axial field B_z with the strength denoted by the color bar. The flux rope structure is confirmed by the closed field lines region and unipolar B_z . The white dot indicates the maximum B_z . The white arrows denote the transverse magnetic field lines (\mathbf{B}_t) along the path of the spacecraft ($y = 0$), and the green arrows along this

path denote the remaining flow velocity. The white contour encloses the area of the reconstruction done from spacecraft data, while the area outside the white contour is reconstructed from extrapolation.

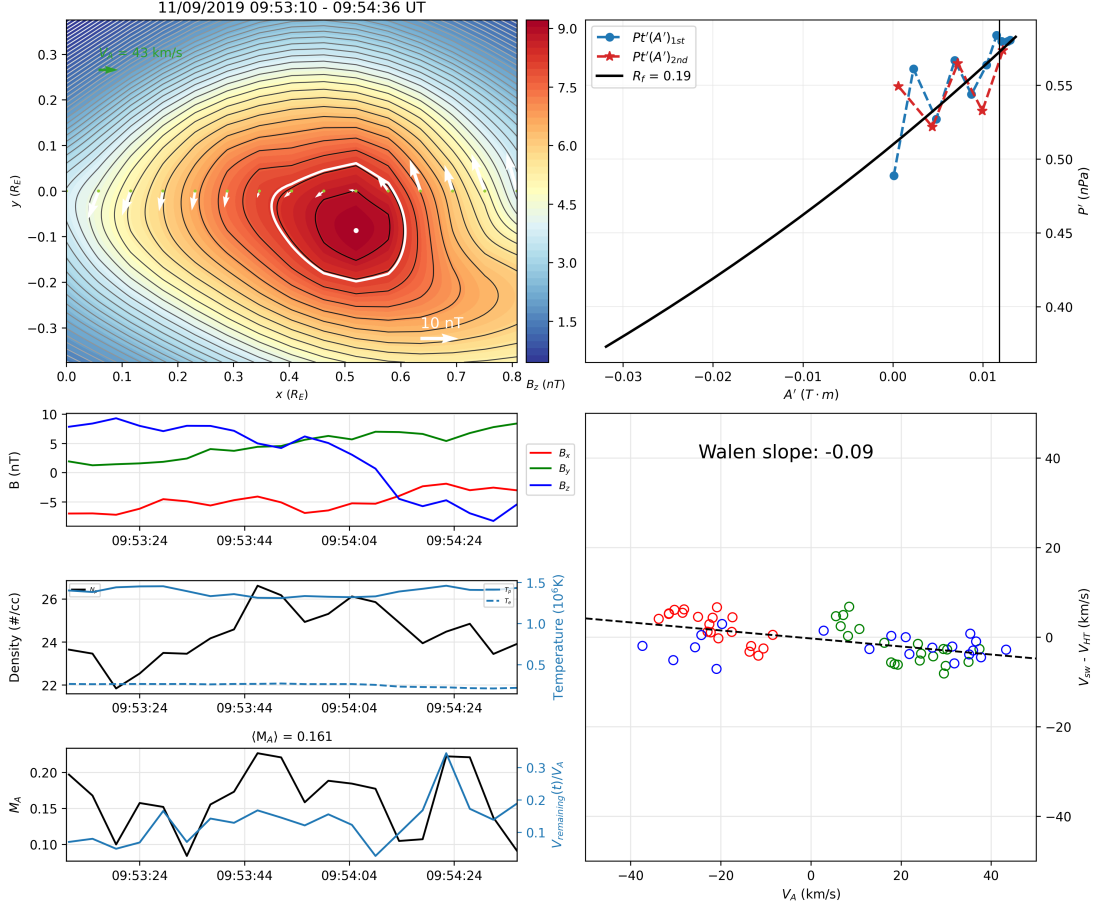


Figure 4.4: GS-based reconstruction of an event 9:53:10-9:54:36 UT on 9 November 2019 in the magnetosheath. Top left: 2D cross-section, with $\hat{x}_{GSE} = [0.890, 0.268, 0.369]$, $\hat{y}_{GSE} = [0.142, 0.605, -0.784]$, $\hat{z}_{GSE} = [-0.433, 0.750, 0.500]$. Bottom left: Associated time series data for MMS-1 in the magnetosheath during this period. Top right: $P'_t(A')$ vs. A' curve for this event. Bottom right: Walén relation for this event.

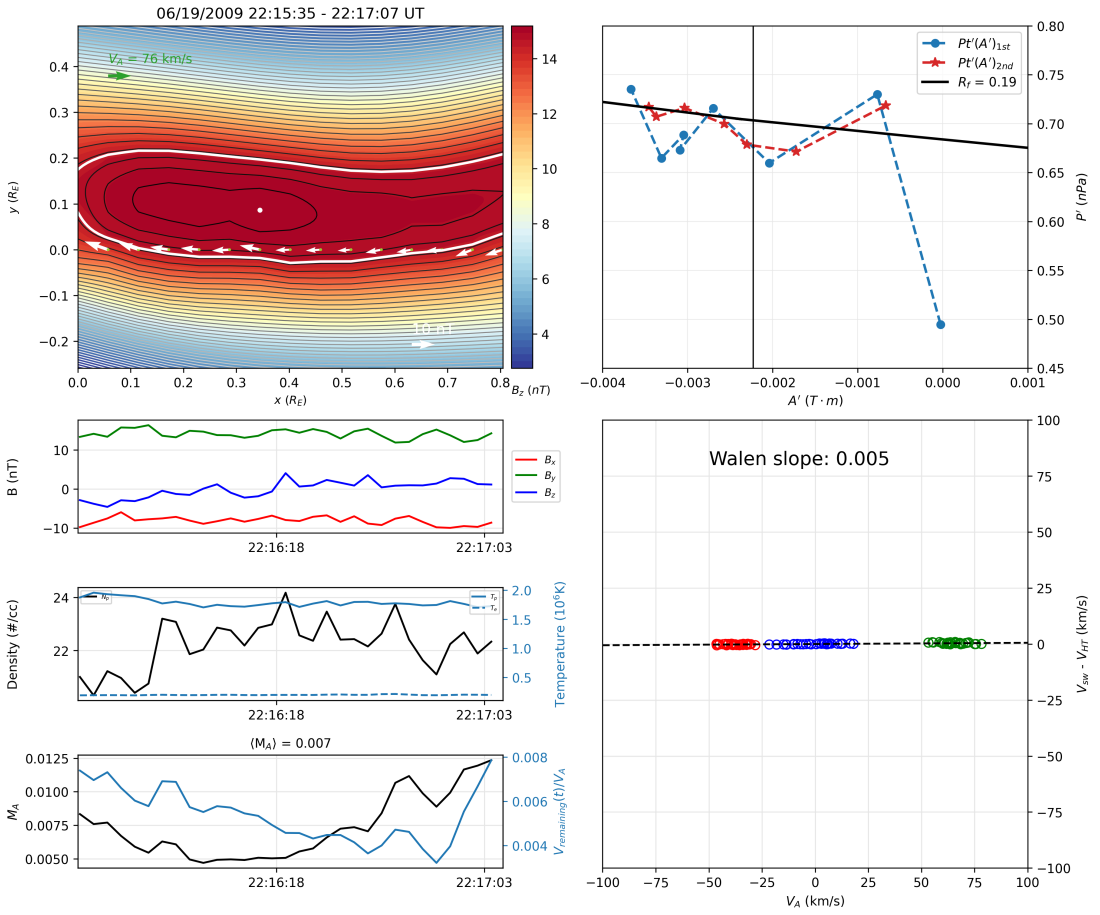


Figure 4.5: GS-based reconstruction of an event from 22:15:35-22:17:07 UT on 19 June 2009 in the magnetosheath. Top left: 2D cross-section, with $\hat{x}_{GSE} = [0.761, -0.103, 0.640]$, $\hat{y}_{GSE} = [0.628, 0.365, -0.688]$, $\hat{z}_{GSE} = [-0.163, 0.925, 0.342]$. Bottom left: Associated time series data for THM-C in the magnetosheath during this period. Top right: $P'_t(A')$ vs. A' curve for this event. Bottom right: Walén relation for this event.

The event in Figure 4.4 has a Walén slope of -0.09, and the event in Figure 4.5 has a Walén test slope of 0.002. This indicates that the structures are static, where the remaining flow vectors (green) along the spacecraft path in the cross-section have little alignment with the transverse magnetic field line vectors

(white arrows). The closed, transverse field lines, and the B_t vectors along the spacecraft path show that the reconstruction in Figure 4.4 is a right-handed event, while the structure in Figure 4.5 is a left-handed flux rope. The maximum B_z of the structure in Figure 4.4 is 11.85 nT, and that of the structure in Figure 4.5 is 18.21 nT. Figure 4.6 shows the reconstruction of a left-handed, quasi-static event in the magnetosheath. It has a much larger scale size ($\sim 5R_E$) than those in the magnetosheath ($\lesssim 1R_E$). The Walén test slope of this event is 0.399, which meets the $|w| > 0.3$ threshold. It can be seen that the structure has a considerable remaining flow, as indicated by the size of the green arrows.

4.4 Analysis results

Table 4.2 summarizes the events identified in the solar wind and magnetosheath across the identified time periods: 19 in the solar wind and 19 in the magnetosheath simultaneously from two spacecraft, and an additional 58 periods in the solar wind and 111 in the magnetosheath (including those from the refined Toy-Edens et al. (2024a) list). The occurrence rate for events in the solar wind from the GS-based is about 5.1 events/hour and for the magnetosheath the corresponding rate is about 7.3 events/hour. SFRs are observed approximately in 43% and 44% of the total observation periods in the solar wind and magnetosheath, respectively. Properties of the magnetic structures are recorded during the identification process. The average duration of the events identified with the GS-based method is 5.03 minutes for the solar wind and 3.57 minutes for the

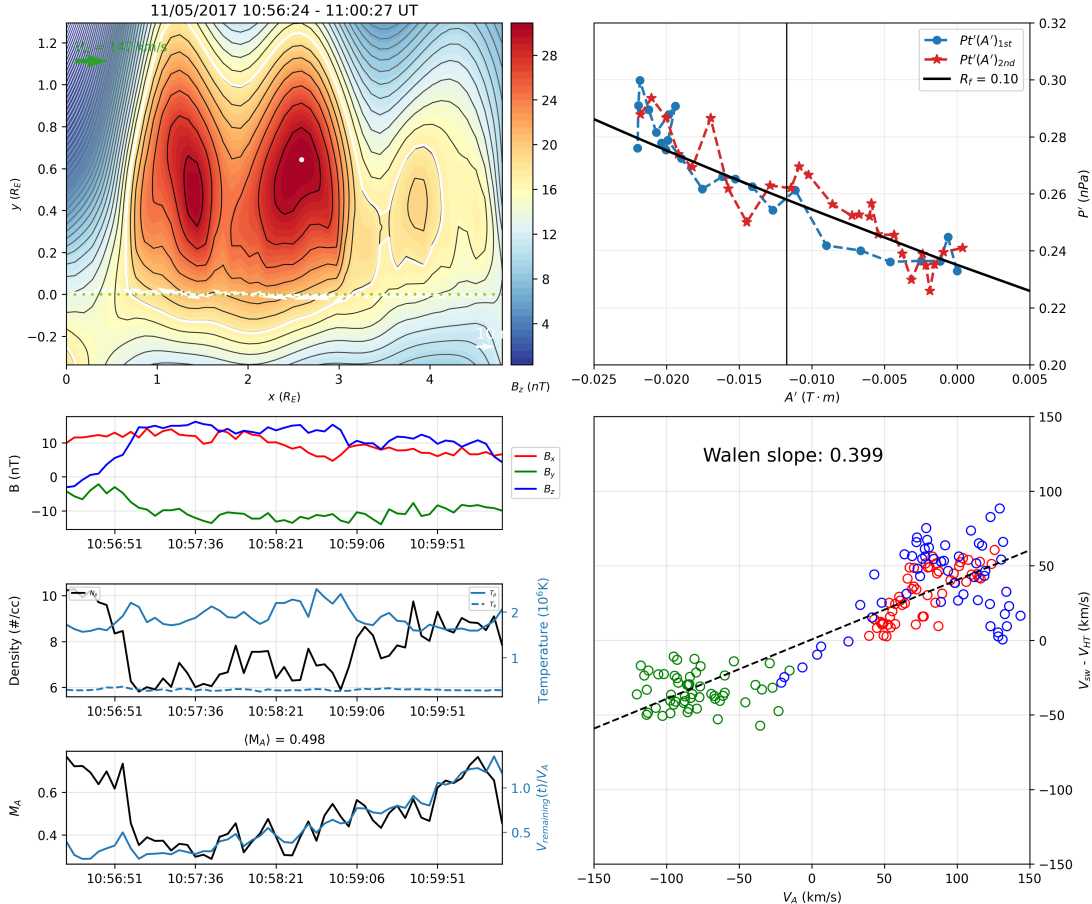


Figure 4.6: GS-based reconstruction of an event on 10:56:24-11:00:27 UT on 5 November 2017 in the magnetosheath. Top left: 2D cross-section, with $\hat{x}_{GSE} = [0.409, -0.029, -0.912]$, $\hat{y}_{GSE} = [0.561, 0.796, 0.226]$, and $\hat{z}_{GSE} = [0.720, -0.604, 0.342]$. Bottom left: Associated time series data for MMS-1 in the magnetosheath during this period. Top right: $P'_t(A')$ vs. A' curve for this event. Bottom right: linear regression of the remaining flow V_{rem} versus the Alfvén velocity V_A , with Walén slope for this event being 0.399.

Table 4.2: Summary table for identified events in the solar wind and magnetosheath via the GS-based reconstruction identification algorithm.

	Observation period [hrs]	Events	Event rate [#/hour]
<i>Solar wind</i>	676 hours	3476	5.1
<i>Magnetosheath</i>	1051 hours	7689	7.3

magnetosheath. The average magnetic field for the identified events is 4.8 nT in the solar wind and 21.6 nT in the magnetosheath.

Table 4.3 summarizes the statistical values for the events identified with the GS-based analysis. In the solar wind, there are a large number of events with an average magnetic field of less than 10 nT, whereas in the magnetosheath there are relatively much fewer events with $\langle B \rangle < 10$ nT. The median magnetic field magnitude in the solar wind is 4.3 nT, and 17.9 nT in the magnetosheath. The mean $\langle B \rangle$ in the magnetosheath is ~ 20 nT for all of the events identified. In the solar wind, this number is much smaller around 4.9 nT. As shown in Table 4.3, the duration of the events has similar ranges for the two regions. However, for the scale sizes of the GS events in the magnetosheath, they range from 251.7 km to 6×10^5 km, with a median and mean of 1.6×10^4 km, $\sim 2.5 R_E$ and 3.8×10^4 km, $\sim 6.0 R_E$, respectively. In the solar wind, the corresponding values are from 1296.1 km to 8.6×10^5 km, and a median (mean) of 2.9×10^4 (9.1×10^4) km, ~ 4.6 (14) R_E .

Table 4.3: Statistical values for the physical quantities of the structures identified with the GS-based analysis. Top: magnetosheath; bottom: solar wind.

	Minimum	Maximum	Mean	Median	Std. Dev.
Duration [min]	0.4	25.7	3.6	1.5	4.8
Velocity [km/s]	12.0	547.8	211.4	203.5	81.1
Temperature [10^6 K]	0.6	29.2	3.2	2.3	2.5
$\langle B \rangle$ [nT]	2.0	95.2	21.6	17.9	12.7
Scale size [km]	251.7	6.0×10^5	3.8×10^4	1.6×10^5	5.6×10^4
<hr/>					
Duration [min]	0.4	25.7	5.0	1.6	6.6
Velocity [km/s]	255.8	666.0	365.7	340.2	87.2
Temperature [10^6 K]	0.1	15.2	3.2	3.1	3.5
$\langle B \rangle$ [nT]	0.7	19.9	4.8	4.3	2.5
Scale size [km]	1296.1	8.6×10^5	9.1×10^4	2.9×10^4	1.3×10^5

The GS-based method can generate a set of unique physical parameters (Hu, 2017) as summarized in Table 4.4. They include the approximate axial magnetic flux, Φ_z , a product of $\langle B_z \rangle$ and $\pi(\text{scale size}/2)^2$, the poloidal magnetic flux per meter, $|A_m| = \max(|A|)$, and the approximate helicity density per meter $\Phi_z|A_m|$ (Hu et al., 2014). In addition, the statistics for the proportionality parameter α are also presented. It generally indicates a modest level of Alfvénicity in both the solar wind and in the magnetosheath. The last two rows in the top and bottom blocks of Table 4.4 provide a proxy to the estimated magnetic helicity per unit volume. No clear differences are seen in the distributions and statistics for Φ_z and $|A_m|$ between the two regions.

Figure 4.7 displays the distributions of the approximation to the axial flux and poloidal flux (per unit length) for events identified via the GS-based automated algorithm. Both distributions follow approximate and similar power laws in both regions. The magnetosheath exhibits events corresponding to the maximum magnitude of $|A_m|$ values larger than that in the solar wind, but these counts are few. The mean $|A_m|$ in the solar wind (0.031 Tm) is only slightly lower than that in the magnetosheath (0.035 Tm), and all corresponding statistical values are of the same orders of magnitude. For completeness, Figure 4.8 shows the distribution of the approximation to the helicity density per unit length. The sample size needs to be enlarged to discern any differences between the two distributions. The statistical values for the helicity density per meter for the events in the magnetosheath are generally of the same orders of magnitude as those in the solar wind, except for the maximum and that the median for

Table 4.4: Statistical values for the physical quantities characterizing the SFR structures identified solely via the GS-based method in the two regions. Top: magnetosheath; bottom: solar wind.

Criteria	Minimum	Maximum	Mean	Median
Φ_z [Tm ²]	403.8	4.8×10^9	4.9×10^7	2.1×10^6
$ A_m $ [Tm]	3.1×10^{-5}	3.6	0.04	9.2×10^{-3}
Helicity Density [T ² m ³]	0.01	1.7×10^{10}	1.4×10^7	1.9×10^4
$\alpha = < M_A >^2$	$ w \leq 0.3$	1.3×10^{-6}	0.99	0.14
	$ w > 0.3$	0.09	0.81	0.37
$\langle A \cdot B_z \rangle$ [T ² m]		4.0×10^{-14}	3.0×10^{-8}	3.1×10^{-10}
				4.7×10^{-11}
$\max(A \cdot B_z)$ [T ² m]		7.4×10^{-14}	1.0×10^{-7}	7.7×10^{-10}
				1.1×10^{-10}
Φ_z [Tm ²]	375.5	4.9×10^9	8.7×10^7	2.1×10^6
$ A_m $ [Tm]	2.3×10^{-5}	1.6	0.03	4.0×10^{-3}
Helicity Density [T ² m ³]	0.01	2.0×10^9	1.9×10^7	6.9×10^3
$\alpha = < M_A >^2$	$ w \leq 0.3$	1.4×10^{-6}	0.81	0.06
	$ w > 0.3$	0.09	0.81	0.34
$\langle A \cdot B_z \rangle$ [T ² m]		1.3×10^{-15}	5.4×10^{-9}	8.8×10^{-11}
				5.3×10^{-12}
$\max(A \cdot B_z)$ [T ² m]		1.9×10^{-15}	1.0×10^{-8}	1.8×10^{-10}
				1.1×10^{-11}

the magnetosheath is ~ 2.5 times larger than that of the solar wind. On the other hand, the statistical values for the helicity density per unit volume in the

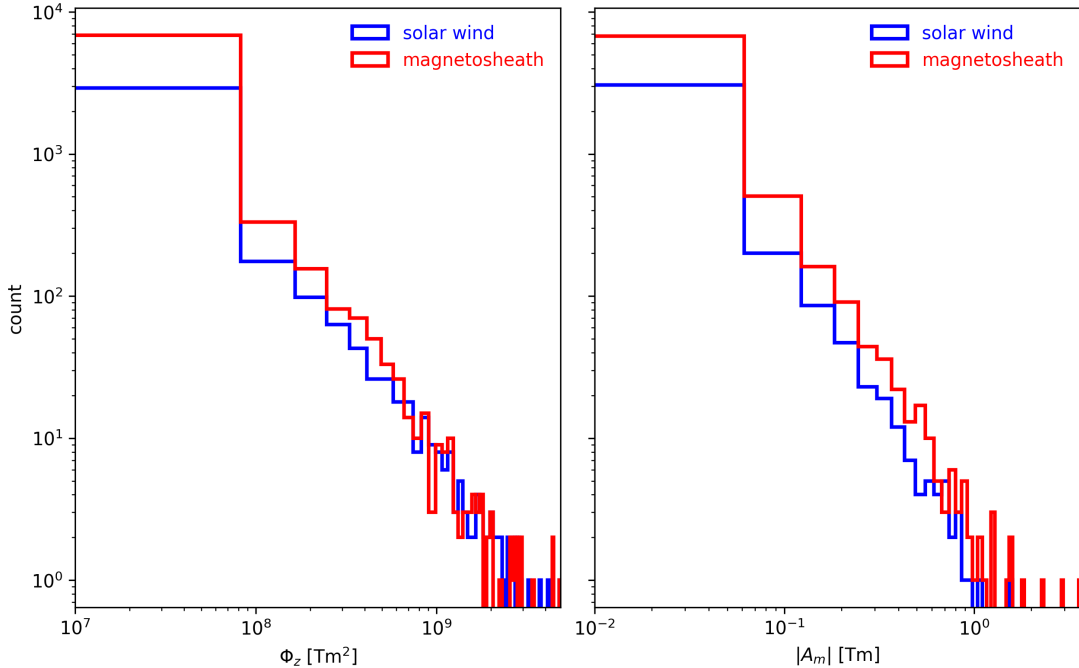


Figure 4.7: Distributions of the axial flux (left panel) and the poloidal flux per unit length (right panel) of events identified via the GS-based analysis. Blue lines are for solar wind events, and red lines for magnetosheath events.

magnetosheath are typically larger than those in the solar wind by one order of magnitude. This is likely an indication of compression of the SFR structures downstream of the bow shock.

Figures 4.9 and 4.10 display the 2D distributions of various parameters vs. the poloidal magnetic flux per unit length $|A_m|$ for events identified with the GS-based method. The distributions of a) average velocity, b) proton β , c) scale size, and d) the product of $\langle |B_y| \rangle$ and one-half of the scale size versus $|A_m|$. The average value of $|A_m|$ in each bin (on the x -axis) are marked by red X's. The peaks in poloidal flux for all distributions in the magnetosheath are centered

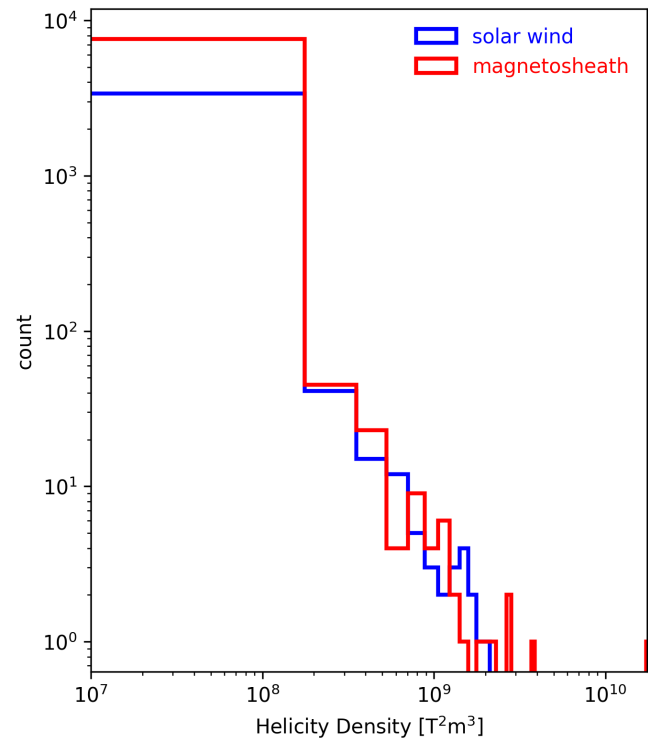


Figure 4.8: Histograms for the approximation to the helicity density per unit length of the events identified via the GS-based analysis for the solar wind (blue) and the magnetosheath (red).

around $|A_m| = 10^{-2}$ Tm, whereas in the solar wind this value is $|A_m| = 10^{-3}$ Tm. For the scale size versus $|A_m|$ distribution, there is a larger range of events with smaller scale size and lower $|A_m|$ in the magnetosheath than in the solar wind. The peak for the distribution in the solar wind is near ($|A_m| = 10^{-3}$ Tm, size= 2×10^4 km), and for the magnetosheath it is close to ($|A_m| = 10^{-2}$ Tm, size= 10^4 km); thus, the magnetosheath is seen to experience larger flux with smaller-sized structures. These results complement the idea that the SFRs experience compression downstream of the bow shock.

4.5 Walén test and Alfvénicity

As described in Section 4.2, the Walén test slope w is used to further distinguish Alfvénic structures. Figure 4.11 shows the linear regression between $\mathbf{V}_{\text{sw}} - \mathbf{V}_{\text{HT}}$ and \mathbf{V}_A during the event on 9 November 2019 during 9:53:10 - 9:54:36 UT. The Walén slope $w = -0.09$ indicates that this event is a static flux rope-like structure, because the magnitude of the slope is less than 0.3.

The distributions of the reduced cross helicity and residual energy for all identified events with the GS-based reconstruction identification algorithm are shown in Figure 4.12. Like Figure 3.5 (in Section 3.4), Figure 4.12 has a flatter distributions of reduced cross helicity σ_c in the magnetosheath than in the solar wind. Unlike the analogous distributions in Figure 3.5, Figure 4.12 shows that for the GS-based analysis result, there are nearly no events with $\sigma_r > 0$. This is likely due to the intrinsic differences between the two methods. With the GS-based method, one can evaluate the Alfvénicity of the structures with the Walén

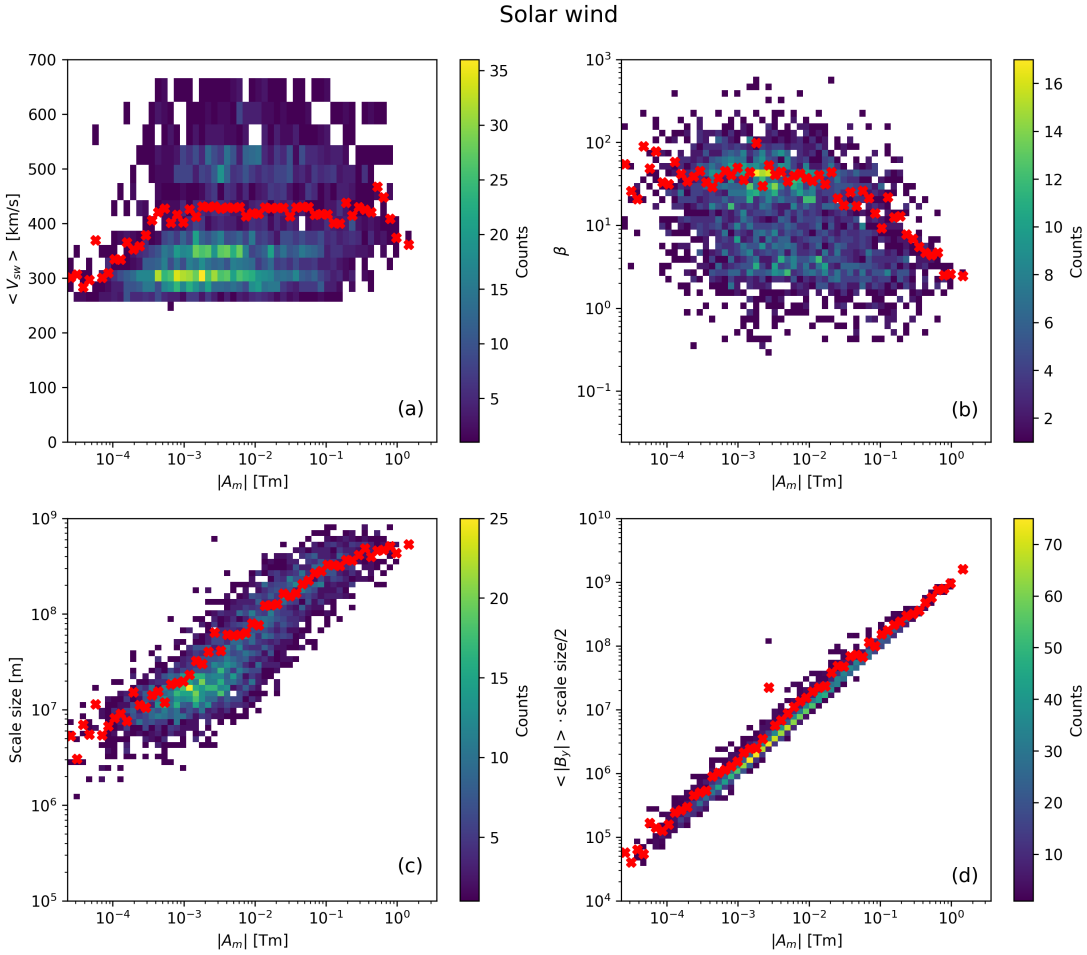


Figure 4.9: 2D distributions of a) average velocity, b) proton β , c) scale size, and d) the product of $<|B_y|>$ and one-half of the scale size versus the poloidal magnetic flux per unit length, for events identified with the GS-based method in the solar wind. The red X's mark the average value in each bin along the x -axis.

test slope. Table 4.5 summarizes the classification of the events with the Walén test slope. There is a slightly higher relative number of events with Walén slope $|w| > 0.3$ in the magnetosheath than in the solar wind. The majority (5088) of the 7689 events from the GS-based algorithm in the magnetosheath have Walén test slopes $|w| \leq 0.3$, and 2601 events have Walén slopes $|w| > 0.3$. 1067 events

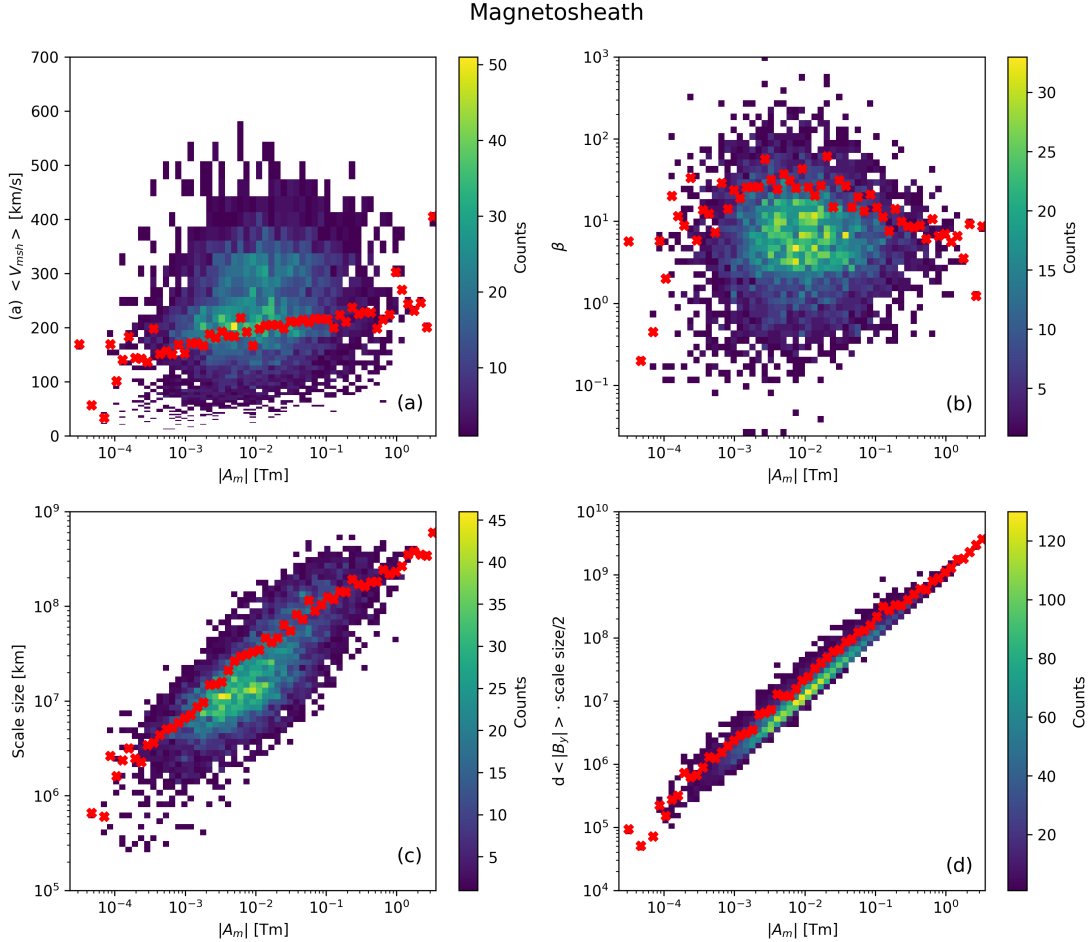


Figure 4.10: 2D distributions of a) average velocity, b) proton β , c) scale size, and d) the product of $<|B_y|>$ and one-half of the scale size versus the poloidal magnetic flux per unit length, for events identified with the GS-based method in the magnetosheath. The red X's mark the average value in each bin along the x -axis.

of the 3476 GS-based algorithm events in the solar wind have $|w| > 0.3$, which is a slightly lower proportion compared to that in the magnetosheath.

It can be seen that events with a high Alfvén Mach number (and thus proportionality constant α) are more prominent in the magnetosheath. The distribution of the proportionality constant α partially represents the data in Tables

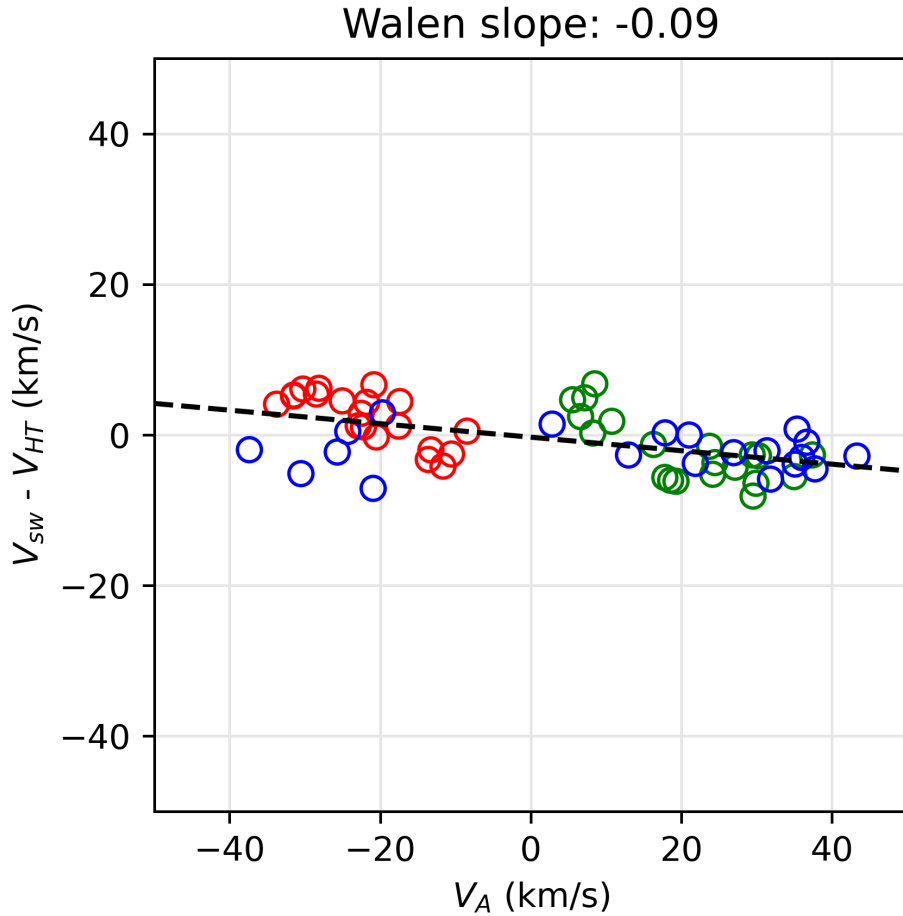


Figure 4.11: Plot of $\mathbf{V}_{sw} - \mathbf{V}_{HT}$ and \mathbf{V}_A for 9 November 2019 during 9:53:10 - 9:54:36 UT. The black dashed line is the linear regression between the two quantities. The slope of the line is the Walén slope, as denoted on top. The red, green, and blue circles represent the x -, y -, and z - components of the velocities, respectively.

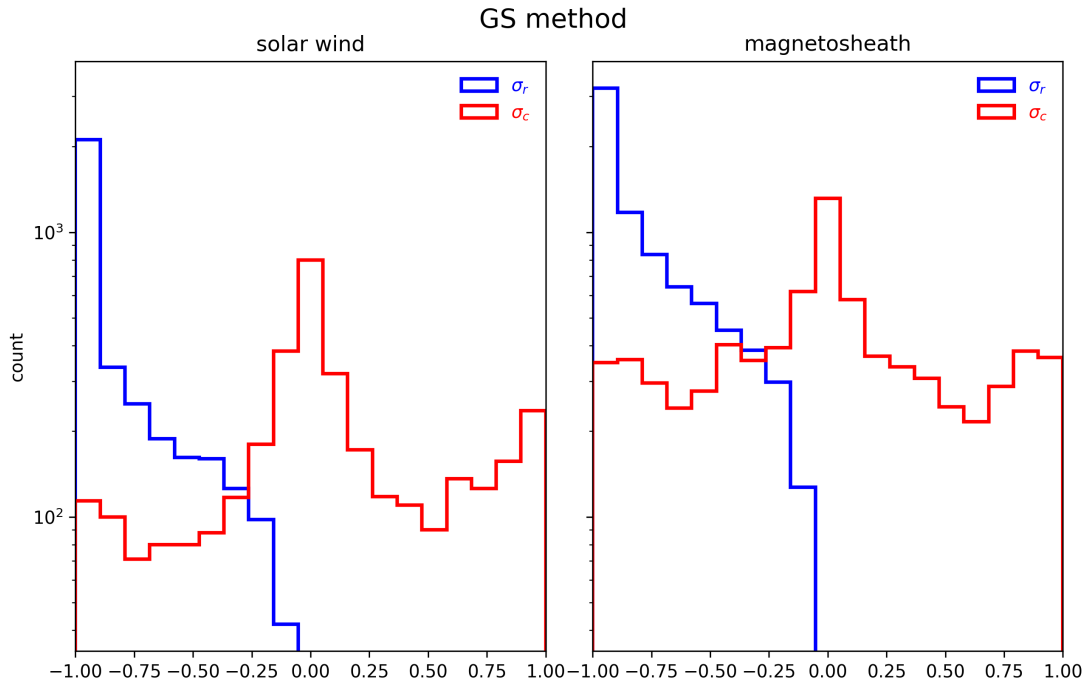


Figure 4.12: Histograms of reduced cross helicity σ_c (red) and reduced residual energy σ_r (blue) for all solar wind (left) and magnetosheath events (right) identified with the GS-based reconstruction identification algorithm.

Table 4.5: Events identified with the GS-based method meeting different Walén test slope criteria.

	Solar wind	Magnetosheath
<i>Total</i>	3476	7689
$ w \leq 0.3$	2409	5088
$ w > 0.3$	1067	2601

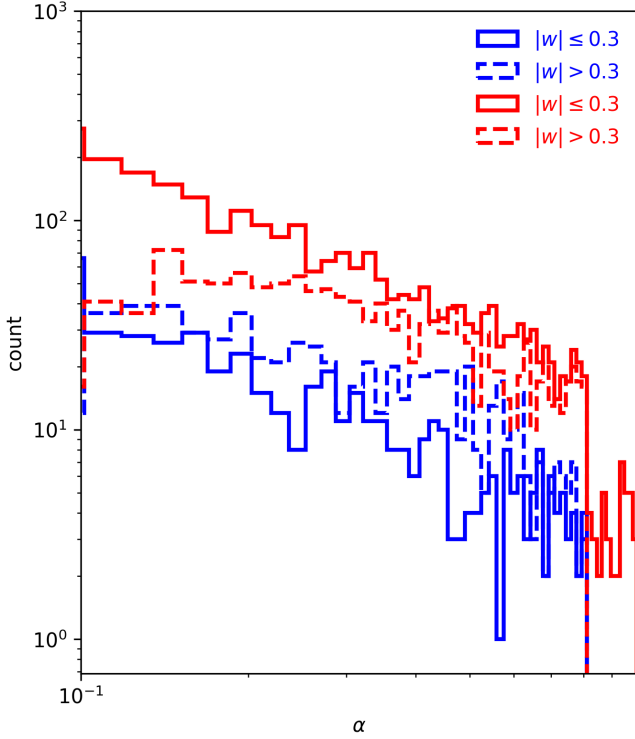


Figure 4.13: Histograms for proportionality constant $\alpha = \langle M_A \rangle^2$ of events identified via GS analysis. For this histogram, blue lines are solar wind events, and red lines are magnetosheath events. Solid lines represent events with a Walén slope $|w| \leq 0.3$ and dashed lines represent events with $|w| > 0.3$.

4.4 and 4.5. The mean α for events with $|w| \leq 0.3$ was 0.337 and 0.366 for the solar wind and magnetosheath, respectively. For $|w| > 0.3$, the means had a greater difference at 0.059 and 0.139 for the respective regions. The median values for α in the solar wind were 7.575×10^{-3} for $|w| \leq 0.3$ and 0.297 for $|w| > 0.3$. In the magnetosheath, the median values for α were 0.055 and 0.323 for $|w| \leq 0.3$ and $|w| > 0.3$, respectively.

Figure 4.14 shows the Walén test slope versus the reduced cross helicity for all of the events identified via GS analysis. Each circle represents an event,

with the size of the circle corresponding to the magnitude of the poloidal flux per unit length. It can be seen that in the solar wind, the events with a larger magnitude of poloidal flux have low cross helicity (close to zero), whereas in the magnetosheath the events with larger poloidal flux are seen closer to ± 1 . The trend between the two quantities appears closely to a diagonal line, indicating that they are inherently related. Chen and Hu (2022) found a similar relation; however, beyond the connection to Alfvénicity, the physical correlation between the Walén test slope and reduced cross helicity has not been determined.

4.6 Flow velocities and orientation of SFRs

Lastly, a representation of the average flow velocities of the identified event intervals, i.e., \mathbf{V}_{HT} vectors, is shown in Figure 4.15. For the identified SFR structures, I find that the corresponding flow velocities in the solar wind are fairly uniform and along the Sun-Earth direction; however, in the magnetosheath the flows appear to be largely deflected toward the dusk-side flank. Therefore the structures near the flanks (downstream of the quasi-perpendicular portion of the bow shock) ought to have elongated cross sections, resulting in large scale sizes. It is likely that while the structures may be compressed by the bow shock in the dimension along the normal direction of the bow shock, they may experience stretching along the dimension in the direction of the bulk flows, i.e., approximately perpendicular to the normal direction. This explains why some structures in the magnetosheath have large scale sizes, for instance, larger than the typical width of the magnetosheath itself.

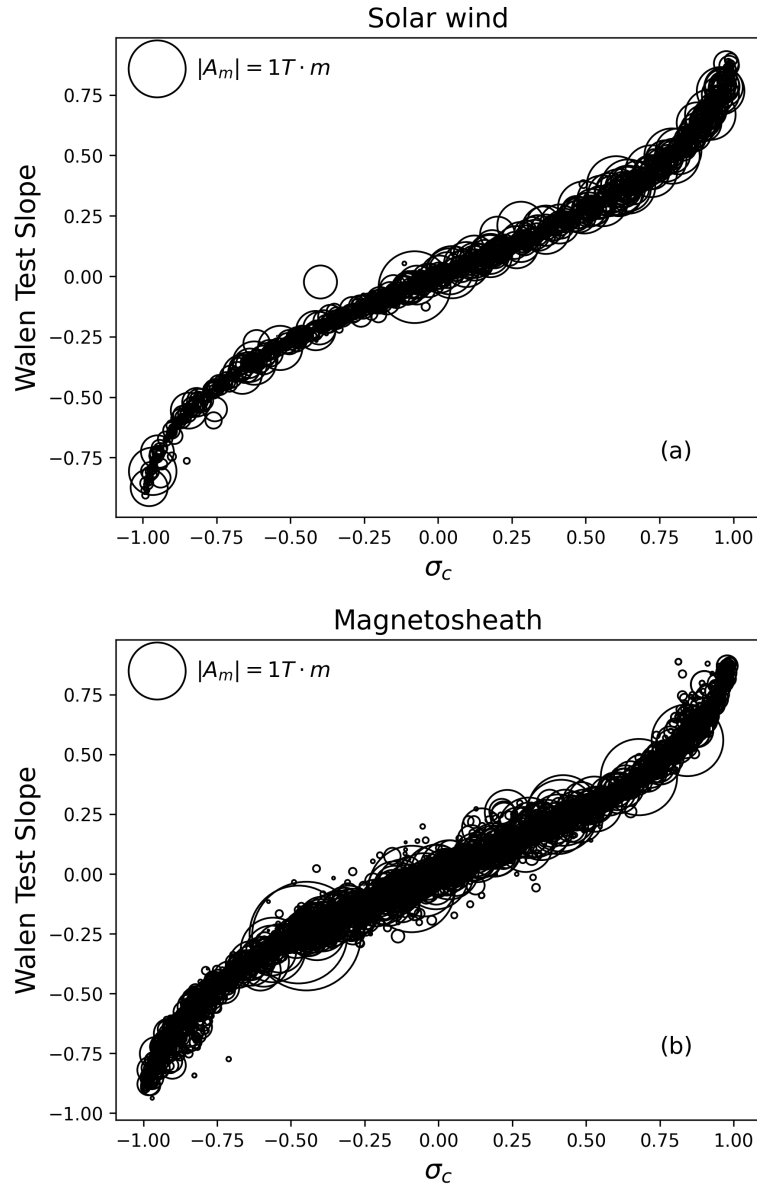


Figure 4.14: Walén test slope versus the reduced cross helicity for all of the events identified via GS analysis in both the solar wind (top) and magnetosheath (bottom). The size of the black circle represents the magnitude of the poloidal flux per unit length of each event. A reference circle of 1 Tm is present.

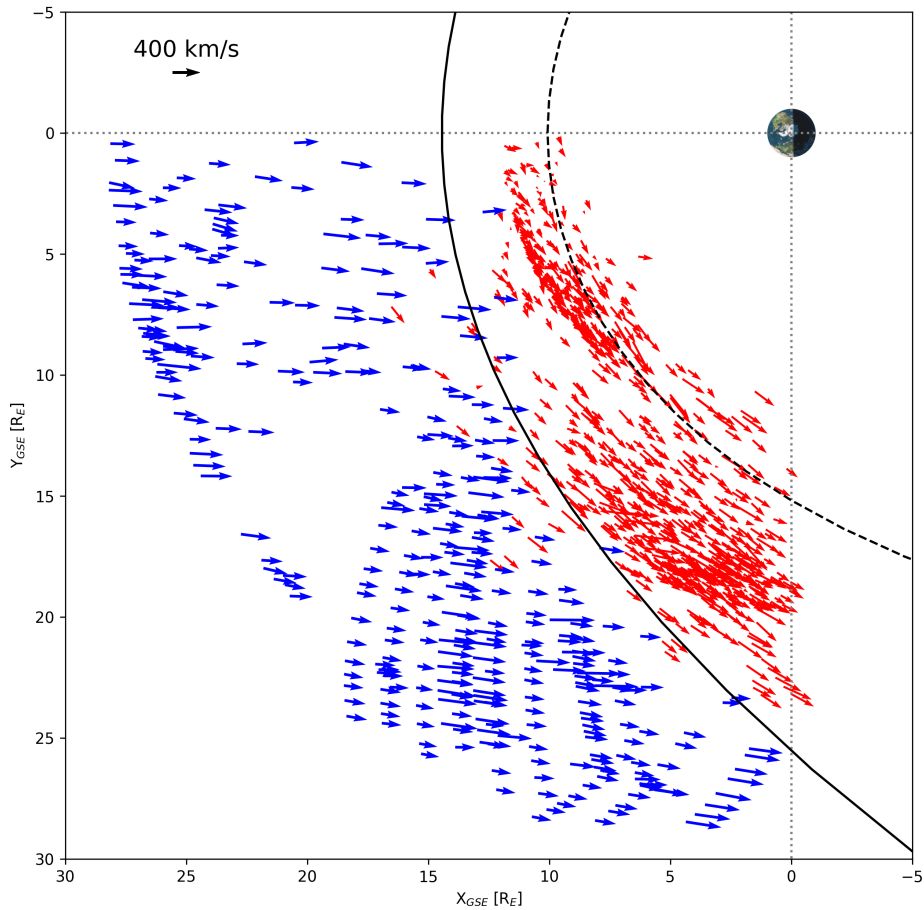


Figure 4.15: Plot showing the \mathbf{V}_{HT} vectors at the locations of one-tenth of the total events identified in the solar wind (blue) and magnetosheath (red) on the GSE- XY plane. The nominal bow shock (solid curve) and magnetopause (dashed curve) locations are drawn based on the models by Shue et al. (1997) and Slavin et al. (1984), respectively. A reference vector of magnitude 400 km/s is shown in the upper left corner.

Figure 4.16 shows the histograms of the z -axis orientation angles of the structures identified from the GS-based algorithm. For the solar wind, there is a single peak in the polar angle distribution centered around 60-70 degrees; however, for the magnetosheath there are two prominent peaks: one around 20-40 degrees and another from around 120-140 degrees. There is a significant trough in the distribution for the magnetosheath events around 80-100 degrees. The azimuthal angle has a flatter distribution in the solar wind than in the magnetosheath. The azimuthal angles in the solar wind show a small dip in the distribution around 170 degrees, and correspondingly there are two narrower peaks for the azimuthal angle in the magnetosheath, around 100 degrees and 260-300 degrees, possibly separated by 180 degrees. The shift in the dip between the two distributions is small, going from about 170 to 200 degrees for the two regions. Overall, the distributions of the azimuthal angle maintain similar shapes in the two regions, except for an additional enhanced peak near $\Phi \approx 0$ in the magnetosheath. The significant change in the polar angle in the magnetosheath indicates that the structures likely experience a rotation in the orientation downstream of the bow shock. It is possible that the interaction with the bow shock forces the change in the orientation of the magnetic structures.

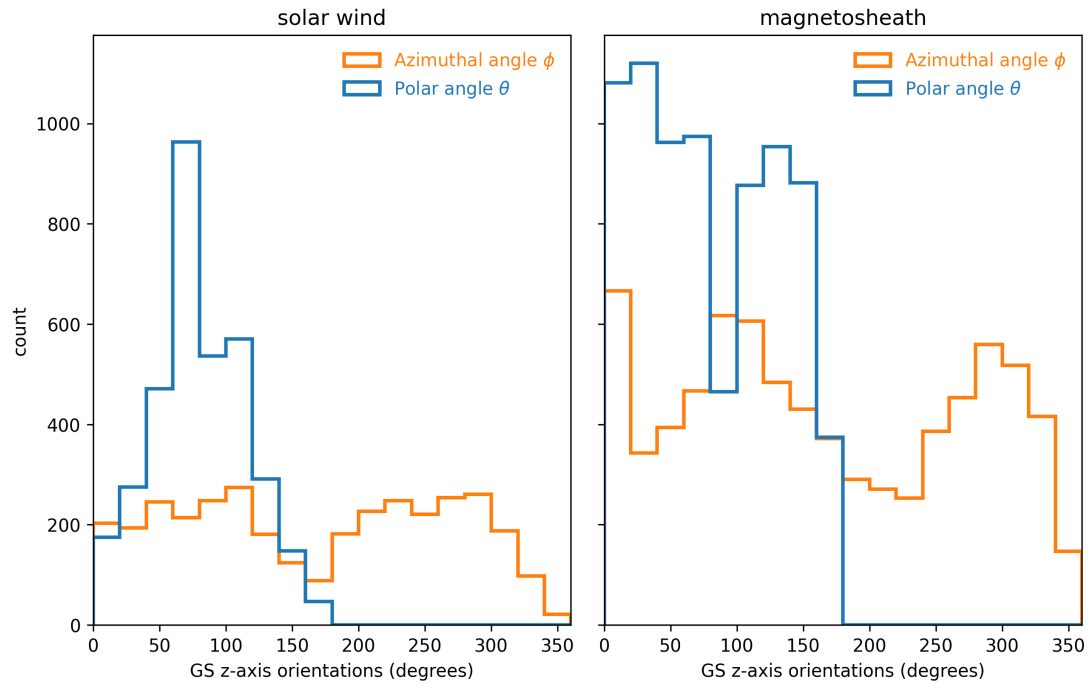


Figure 4.16: Distributions of the azimuthal (orange) and polar angles (blue) of the directional angles that define the z -axis (in the GSE coordinate system) of the SFR structures identified from the GS-based analysis in the solar wind (left panel) and the magnetosheath (right panel).

Chapter 5. Combined analysis results

Figures 5.1 and 5.2 show the distributions of event duration and structure scale size from events identified with wavelet analysis and the GS-based method. The scale sizes of the solar wind events and the magnetosheath events have a large difference, in part because of the differences in duration. The wavelet events in the solar wind are almost twice as large as the events from the GS-based method. In the magnetosheath, the average scale size of the wavelet events is almost three times as large as that of the GS events. Because of the difference in the minimum and maximum limits of calculating the duration of the events between the wavelet analysis and GS-based methods, the ranges in duration are different. The range of duration for the SFRs identified by the wavelet analysis method is dictated by the time cadence of the spacecraft data (Torrence and Compo, 1998); whereas the duration range of the SFRs identified by the GS-based method can be extended arbitrarily toward the upper limit end (though there are computational limits). The scale size is calculated by taking the average speed of the event interval and multiplying it by the duration of the event for the wavelet analysis. For the SFRs identified by the GS-based method, this calculation is done using the projected de Hoffmann-Teller frame velocity on the cross-sectional plane, which takes into account the orientation of the cylindrical structure in relation to the

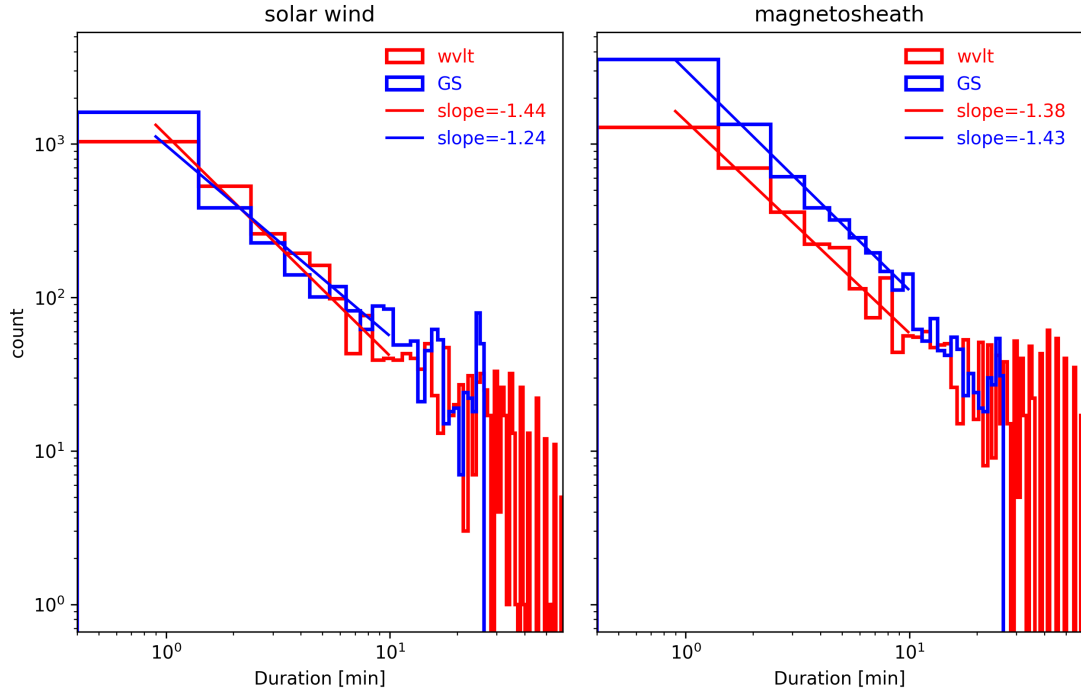


Figure 5.1: Histograms of the duration of events identified by using wavelet analysis (red lines) and the GS-based method (blue lines) in the solar wind (left panel) and magnetosheath (right panel), respectively. The straight lines are the nominal linear fitting to each distribution in a log-log scale with the corresponding slopes denoted in the legend.

spacecraft path thus representing a better cross-sectional size. Whereas such a characterization is not feasible through the wavelet analysis method because like a typical time-series analysis method, it does not characterize structure in dimensions higher than 1D. The scale size calculated in the GS-based method represents a true cross-sectional size for a 2D configuration.

Figure 5.2 shows the corresponding distributions of the scale sizes for the identified events in the magnetosheath and solar wind. They generally follow power laws and the trends indicate that there are more, smaller-size events in the

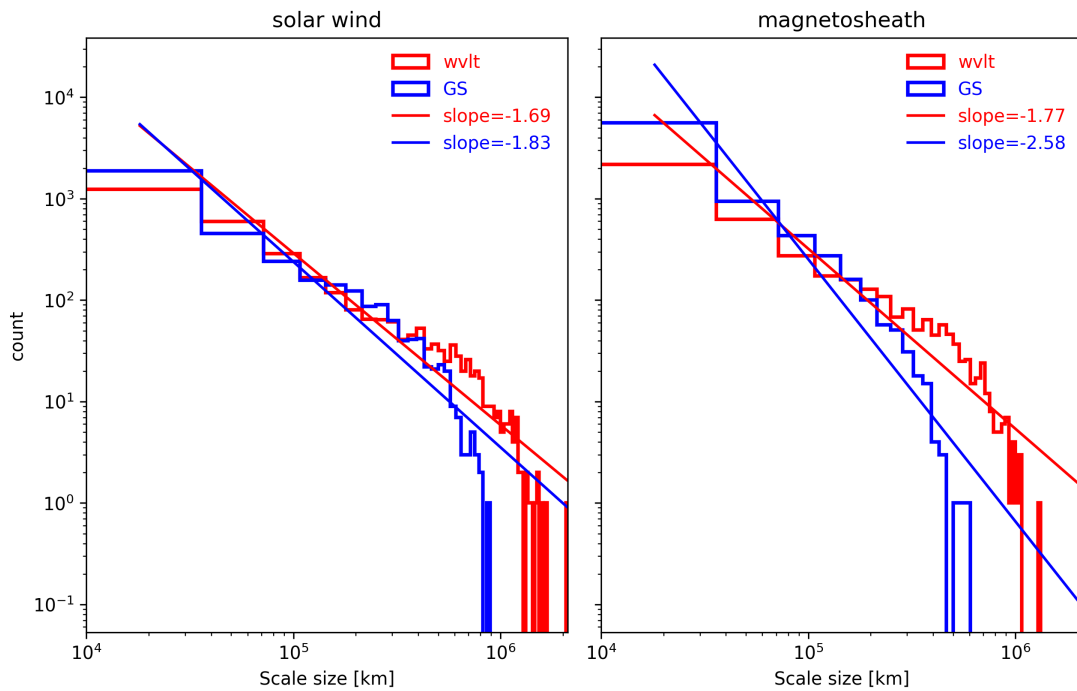


Figure 5.2: Same as Figure 5.1 but for scale size distributions of identified events.

magnetosheath than in the solar wind. This is largely seen through the slope of the scale size distribution of the GS-based method in the magnetosheath, which has a smaller upper limit and a steeper slope than the corresponding distribution in the solar wind. The power-law distributions in Figure 5.2 can indicate anomalous (super- or sub- diffusive) transport. Solar energetic particles (SEPs) can be trapped between the boundaries of two adjacent SFRs (le Roux, 2023), but with power law distributions of SFR scale sizes, the energetic particles can escape to open field lines, i.e., super-diffusive transport. The power law distributions in this work support the theory that when there is energetic particle transport through coherent magnetic structures that create strong, intermittent magnetic fields, the distributions yield a non-Gaussian power law (le Roux and Zank, 2021).

In Figure 5.3, the cumulative distribution functions of the scale sizes further show that there is a larger percentage of smaller structures in the magnetosheath than in the solar wind. For instance in the magnetosheath, the percentage of events with scale sizes smaller than the mean value (marked by the dashed line in both panels) is greater than 70% which is significantly larger than the corresponding percentage in the solar wind. The structures generally seem to be compressed across the bow shock: the scale sizes are smaller, and the magnetic field becomes stronger. Furthermore, the maximum scale size of the SFRs in the solar wind is found to be approximately 2 million km, which is on the same order as the turbulence correlation length (Horbury et al., 1996). The power-law distributions are also in agreement with (Nakanotani et al., 2022a,b) which simulated the generation and interaction of smaller scale structures across a shock wave and

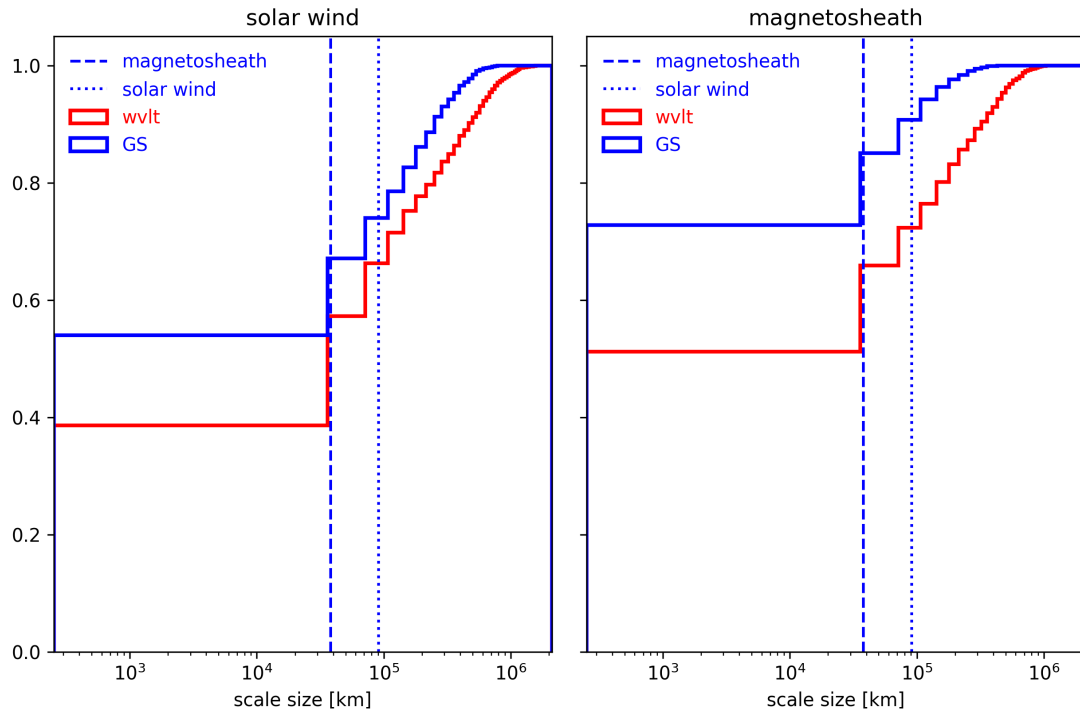


Figure 5.3: Cumulative distribution function of scale sizes for the identified events (see legend) in the solar wind (left panel) and magnetosheath (right panel). The vertical lines mark the corresponding mean values of the scale sizes for the GS-based method for the solar wind (dotted blue lines) and the magnetosheath (dashed blue lines) in both panels.

compared with the turbulence theory (Zank et al., 2021a, 2017). Based on our analysis result, since the solar wind is dominated by quasi-2D structures, such as SFRs, the power laws are generally in agreement with the 2D-slab model of turbulence (Zank et al., 2021a, 2017).

Chapter 6. Coordinated analysis of simultaneous observations

A coordinated analysis between the magnetosheath and solar wind over ~ 250 hours was performed in order to compare simultaneous observations. 18 time intervals were identified during these phases for which there were simultaneous measurements by two THEMIS probes, where at least one probe was in the solar wind and another in the magnetosheath. The dayside science and radiation belt science phases of the THEMIS mission offer optimal configuration for direct comparison of the near-Earth solar wind and magnetosphere, specifically the phases in 2008, 2009, 2018, and 2022. MMS was also used in conjunction with the THEMIS probes for the observation intervals identified in 2022. Table A.3 in Appendix A shows the subsection of observation intervals for this coordinated analysis. Figure 6.1 displays the orbits of THEMIS and MMS during these observation intervals. It should be noted that the data came from simultaneous measurement in two regions during the same interval, *not* a measurement *across* the bow shock.

Figure 2.6 is an example of one observation such period in the magnetosheath during the coordinated analysis. These measurements were taken in the magnetosheath with THM-C, while the measurements in the solar wind were

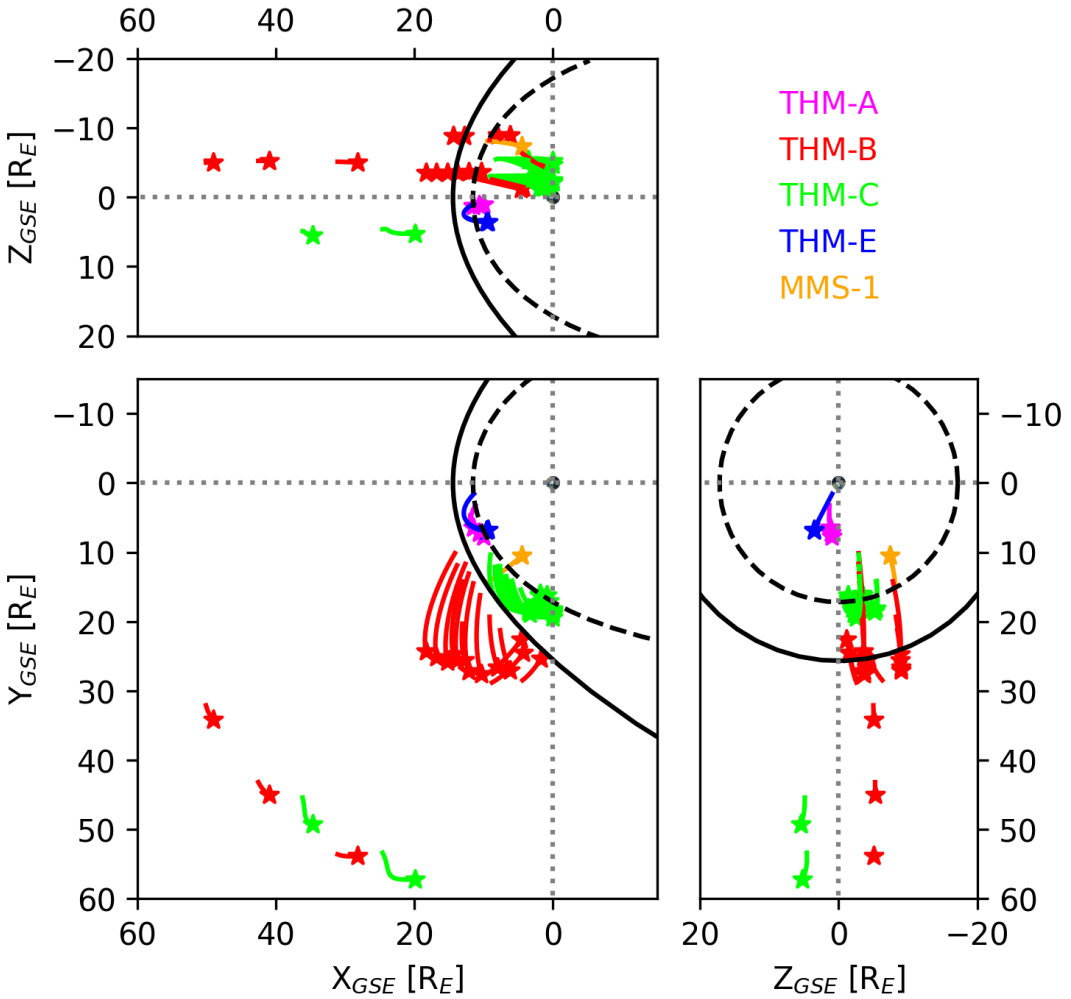


Figure 6.1: Orbits for coordinated analysis time periods are shown in the Geocentric Solar Ecliptic (GSE) coordinates for THEMIS probes A, B, C, and E (THM-A, THM-B, THM-C, THM-E) and MMS-1 probe (see legend), with the stars marking the end of each orbit period. The approximate nominal locations of the magnetopause (dashed black line) modeled using the Shue et al. (1997) model and bow shock (solid black line) modeled using Slavin et al. (1984) are shown, based on the IMF data obtained for one period in 2008 only.

Table 6.1: Summary table for events identified via wavelet analysis and the GS reconstruction algorithm during the simultaneous observation intervals.

Region	Method	# Events	Avg. duration	Avg. B	Avg. scale
			[mins]	[nT]	size [km]
<i>Solar wind</i>	Wavelet	1407	6.43	3.93	1.4×10^5
	GS	1901	3.46	3.90	6.0×10^4
	Total	3308	4.72	3.91	9.3×10^4
<i>Magnetosheath</i>	Wavelet	1152	6.76	14.03	8.8×10^4
	GS	2168	2.64	14.38	2.8×10^4
	Total	3320	4.07	14.26	4.9×10^4

taken with THM-B (Figure 2.7). Following the same procedures as outlined in Section 3.3, 3308 structures were identified in the solar wind, and 3320 structures were identified in the magnetosheath during the coordinated intervals. Table 6.1 displays the results for the number of events identified with each method. Table 6.2 shows the characterization of the events for each method according to MHD criteria (wavelet analysis) and Walén slope criteria (GS reconstruction).

It can be seen from Table 6.2 that there were more events characterized as static flux rope structures in the magnetosheath for the coordinated analysis periods. Approximately 80% of the 1152 structures identified in the magnetosheath using wavelet analysis had a reduced cross helicity magnitude less than 0.3. While there were only incrementally more static structures identified in the

Table 6.2: Events meeting certain MHD quantity (top) and Walén test slope (bottom) criteria.

		Solar Wind	Magnetosheath
	$ \sigma_m \geq 0.75$	1407	1152
<i>Wavelet</i>	$ \sigma_m \geq 0.75, \sigma_c \leq 0.3$	931	921
	$ \sigma_m \geq 0.75, \sigma_r < 0$	1263	962
	$ \sigma_m \geq 0.75, \sigma_c \leq 0.3, \sigma_r < 0$	853	833
	Total	1901	2168
<i>GS</i>	$ w \leq 0.3$	1777	2106
	$ w > 0.3$	124	62

magnetosheath than in the solar wind; however, the number of static structures represents a higher percentage of the total number of structures in the magnetosheath versus 66% in the solar wind. Approximately 97% of the structures identified in the magnetosheath with the GS reconstruction have a Walén test slope value less than or equal to 0.3 for the coordinated event lists. In the solar wind, the percentage is slightly lower at 93%, despite the number of structures identified with $|w| \leq 0.3$ being over 400 less than the number of structures in the magnetosheath.

The wavelet analysis results for the coordinated periods are complementary to the extended analysis periods, with a larger percentage of structures being identified as static structures in the magnetosheath than in the solar wind. How-

ever, in the extended analysis, there was a much smaller difference ($\sim 1\%$) between the two regions. Additionally, there were more structures with $|w| \leq 0.3$ in the solar wind than in the magnetosheath for the extended analysis, which differs from the coordinated analysis.

Figure 6.2 shows the distribution of duration of the SFRs identified from the simultaneous observations. Like Figure 5.1, there is a power law trend. The power law indices (for each region/method) seem to be slightly steeper when only the SFRs from the coordinated analysis are included. Figure 6.3 shows the same power law trend in the distributions of scale size of the SFRs. However, the indices appear to not be much different than those in Figure 5.2.

Figure 6.4 shows the distribution the poloidal flux per unit length $|A_m|$ of the SFRs identified during the coordinated intervals. The distribution of $|A_m|$ seen here is very similar to the distribution seen in the the results from the comprehensive observations.

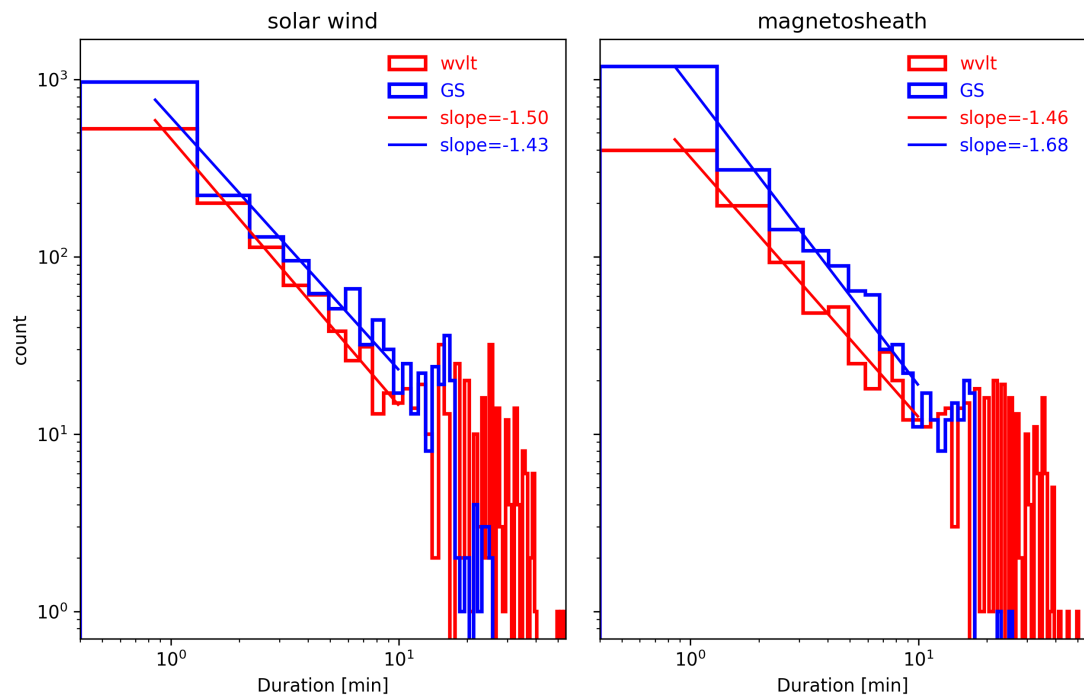


Figure 6.2: Histogram of the duration of events identified (during the coordinated orbit intervals) by using wavelet analysis (red lines) and the GS reconstruction method (blue lines).

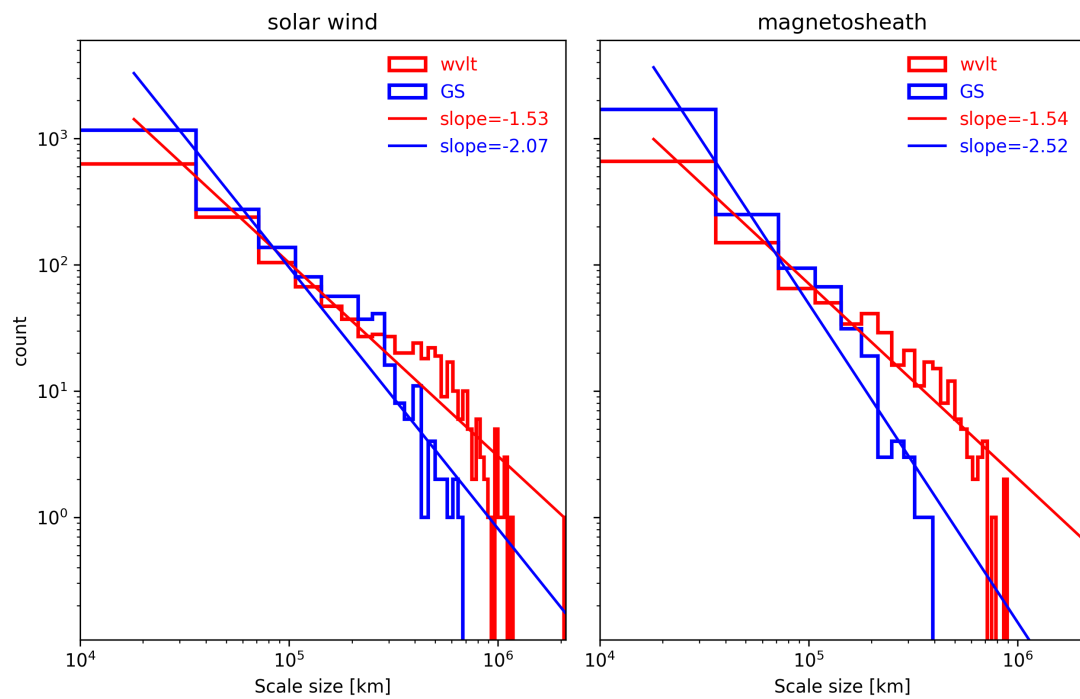


Figure 6.3: Same as Figure 6.2 but for scale size of events identified during the coordinated orbit intervals.

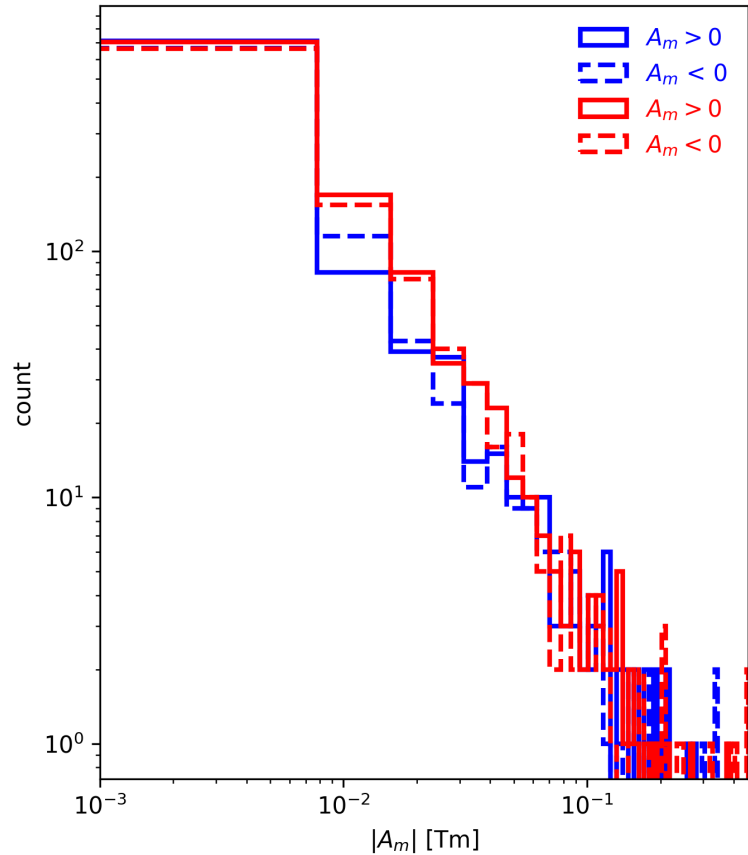


Figure 6.4: Histograms of the local maximum magnetic flux, $|A_m|$, of events identified via GS analysis during the coordinated orbit intervals. Blue (red) lines indicate solar wind (magnetosheath) events. The dashed (solid) lines represent events with negative (positive) A_m .

Chapter 7. Conclusions and Future Work

In summary, a comprehensive analysis of SFR structures in the regions immediately upstream and downstream of the Earth’s bow shock was carried out. There were 11949 events identified in the magnetosheath across 1051 hours, with 7689 events being identified from the GS-based algorithm and 4260 from the wavelet analysis. For the solar wind, there were 6669 events identified across 676 hours, with 3476 being attributed to identification via the GS-based algorithm and 3193 via wavelet analysis. In situ observations of MMS-1, THM-A, THM-B, THM-C, and THM-E spacecraft were utilized. The extended GS-based analysis was used to identify structures with significant remaining plasma flow aligned with the local magnetic field. Wavelet analysis also performed for 77 time periods in the solar wind and 130 time periods in the magnetosheath, corresponding to 676 hours and 1051 hours, respectively. The average magnetic field, velocity, duration, scale size, etc., of these structures were recorded for comparison. In addition to the general parameters, the GS-based method also yielded a unique set of additional parameters that allowed us to evaluate the distributions of the Walén test slope, magnetic helicity density, magnetic flux, and the orientation of the z -axes of the structures.

The distributions of a wide variety of parameters generally follow power laws. The magnetic structures identified by the wavelet analysis were also characterized based on MHD quantities (σ_m , σ_c , σ_r). The different criteria assisted us to distinguish different types of events in terms of dynamic and quasi-static structures in the two regions. This work examined the differences in the properties primarily obtained from the GS-based characterization of the identified SFR structures in the solar wind and magnetosheath. The additional findings of this study are summarized as follows.

1. The magnitudes of the Walén slope $|w|$ and cross helicity σ_c parameters indicate the effect of the remaining plasma flow of the identified structures. Results from both regions indicate that about one-third of structures possess modest (e.g., $|w| > 0.3$) remaining flow relative to the total number of structures identified.
2. SFR structures are generally compressed downstream of the bow shock in the magnetosheath: the scale sizes are smaller while magnetic field strength increases in the magnetosheath. The distributions of the scale sizes and durations of the events shows a power-law trend with more, shorter (in duration and size) events in the magnetosheath than in the solar wind.
3. Magnetic helicity density per unit volume is about one order of magnitude larger than the corresponding value in the solar wind, implying an overall decrease in volume for the SFRs in the magnetosheath. In addition, the

poloidal flux had greater magnitude in the magnetosheath, which indicates more compact, twisted structures.

4. A significant rotation in the polar angle of the z -axis in the magnetosheath is seen when compared to the angle in the solar wind, while the distributions of the azimuthal angle maintain two broad peaks separated by approximately 180 degrees.
5. Identified structures in the magnetosheath (broadly defined as flux ropes with vortical flows) are likely elongated in the downstream flow direction.

Since this study only used data from the quasi-perpendicular region of the Earth's bow shock, future work would be to perform the identification algorithms and statistical analysis on observations from MMS and THEMIS in the quasi-parallel region. As a complement to the coordinated analysis, taking observation intervals directly upstream and downstream of the bow shock could be used to investigate the SFR property changes more directly instead of using an ensemble approach. There are, however, very limited observation periods in which the THEMIS probes are in the right configuration for this type of measurement. Furthermore, the relation between turbulence and the SFRs in the solar wind and magnetosheath could be explored further by implementing some of the procedures in Zank et al. (2021b); Adhikari et al. (2022); Zhao et al. (2022). And lastly, including more in situ observations from spacecraft such as the Advanced Composition Explorer (ACE), Wind, and Cluster would be beneficial to

the work on understanding the differences seen in SFRs in the solar wind and magnetosheath.

References

- Adhikari, L., Zank, G. P., Zhao, L.-L., and Telloni, D. (2022). Mhd turbulent power anisotropy in the inner heliosphere. *The Astrophysical Journal*, 933(1):56.
- Alfvén, H. (1942). Existence of Electromagnetic-Hydrodynamic Waves. *Nature*, 150(3805):405–406.
- Andersen, H. (2018). *Design and Simulation of Pixel Layout and Data Processing Algorithms for the DEEP Instrument*. PhD thesis, University of Bergen.
- Artemyev, A. V., Angelopoulos, V., and Vasko, I. Y. (2019). Kinetic properties of solar wind discontinuities at 1 AU observed by ARTEMIS. *Journal of Geophysical Research: Space Physics*, 124(6):3858–3870.
- Auster, H., Glassmeier, K., Magnes, W., Aydogar, O., Baumjohann, W., Constantinescu, D., Fischer, D., Fornacon, K. H., Georgescu, E., Harvey, P., Hillemeyer, O., Kroth, R., Ludlam, M., Narita, Y., Nakamura, R., Okrafska, K., Plaschke, F., Richter, I., Schwarzl, H., Stoll, B., Valavanoglou, A., and Wiedemann, M. (2008). The themis fluxgate magnetometer. *Space Science Reviews*, 141:235–264.
- Borovsky, J. E. and Valdivia, J. A. (2018). The earth’s magnetosphere: A systems science overview and assessment. *Surveys in Geophysics*, 39.
- Bruno, R. and Carbone, V. (2013). The Solar Wind as a Turbulence Laboratory. *Living Reviews in Solar Physics*, 10(1):2.
- Burch, J. L., Giles, B. L., Ahmadi, N., Argall, M. R., Baker, D. N., Blake, J. B., Bromund, K. R., Cohen, I. J., Ergun, R. E., Fennell, J. F., Fischer, D., Fuselier, S. A., Gabrielse, C. E., Gershman, D. J., Gomez, R. G., Graham, D. B., Hans, U., Henderson, M. G., Huang, B., Jeszenszky, H., Eichelberger, H. U., Le, G., Le Contel, O., Leinweber, H. K., and Lindqvist, P.-A. (2024). Magnetospheric multiscale (MMS) – calibration and measurement algorithms document (cmad). document, NASA.
- Cartwright, M. and Moldwin, M. (2010). Heliospheric evolution of solar wind small-scale magnetic flux ropes. *Journal of Geophysical Research*, 115.

Cartwright, M. L. and Moldwin, M. B. (2008). Comparison of small-scale flux rope magnetic properties to large-scale magnetic clouds: Evidence for reconnection across the HCS? *Journal of Geophysical Research: Space Physics*, 113(A9).

Chapman, J. F. and Cairns, I. H. (2003). Three-dimensional modeling of Earth's bow shock: Shock shape as a function of Alfvén Mach number. *Journal of Geophysical Research: Space Physics*, 108(A5). eprint: <https://onlinelibrary.wiley.com/doi/10.1029/2002JA009569>.

Chen, Y. and Hu, Q. (2020). Effects of radial distances on small-scale magnetic flux ropes in the solar wind. *The Astrophysical Journal*, 894:25.

Chen, Y. and Hu, Q. (2022). Small-scale magnetic flux ropes and their properties based on in situ measurements from the Parker Solar Probe. *The Astrophysical Journal*, 924(2):43.

Chen, Y., Hu, Q., Zhao, L., Kasper, J., Bale, S., Korreck, K., Case, A., Stevens, M., Bonnell, J., Goetz, K., Harvey, P., Klein, K., Larson, D., Livi, R., MacDowall, R., Malaspina, D., Pulupa, M., and Whittlesey, P. (2020). Small-scale magnetic flux ropes in the first two Parker Solar Probe encounters. *The Astrophysical Journal*, 903:76.

Chen, Y., Hu, Q., Zhao, L., Kasper, J., and Huang, J. (2021). Small-scale magnetic flux ropes with field-aligned flows via the psp in-situ observations. *The Astrophysical Journal*.

Collado-Vega, Y. M., Dredger, P., Lopez, R. E., Khurana, S., Rastaetter, L., Sibeck, D., and Anastopoulos, M. (2023). Magnetopause standoff position changes and geosynchronous orbit crossings: Models and observations. *Space Weather*, 21(6):e2022SW003212. e2022SW003212 2022SW003212.

de Hoffmann, F. and Teller, E. (1950). Magnetohydrodynamic shocks. *Phys. Rev.*, 80:692–703.

Dimmock, A. P. and Nykyri, K. (2013). The statistical mapping of magnetosheath plasma properties based on THEMIS measurements in the magnetosheath interplanetary medium reference frame. *Journal of Geophysical Research: Space Physics*, 118(8):4963–4976.

- Farge, M. (1992). Wavelet transforms and their applications to turbulence. *Annual Review of Fluid Mechanics*, pages 395–457.
- Feng, H., Zhao, G., and Wang, J. (2020). Small interplanetary magnetic flux rope. *Science in China E: Technological Sciences*, 63(2):183–194.
- Feng, H. Q., Wu, D., and Chao, J. (2007). Size and energy distributions of interplanetary magnetic flux ropes. *Journal of Geophysical Research*, 112.
- Greco, A., Matthaeus, W. H., Perri, S., Osman, K. T., Servidio, S., Wan, M., and Dmitruk, P. (2018). Partial Variance of Increments Method in Solar Wind Observations and Plasma Simulations. *Space Science Reviews*, 214(1):1.
- Gurchumelia, A., Sorriso-Valvo, L., Burgess, D., Yordanova, E., Elbakidze, K., Kharshiladze, O., and Kvaratskhelia, D. (2022). Comparing quasi-parallel and quasi-perpendicular configuration in the terrestrial magnetosheath: Multifractal analysis. *Frontiers in Physics*, 10.
- Hadid, L. Z., Sahraoui, F., Galtier, S., and Huang, S. Y. (2018). Compressible magnetohydrodynamic turbulence in the earth’s magnetosheath: Estimation of the energy cascade rate using in situ spacecraft data. *Phys. Rev. Lett.*, 120:055102.
- Hau, L.-N. and Sonnerup, B. U. O. (1999). Two-dimensional coherent structures in the magnetopause: Recovery of static equilibria from single-spacecraft data. *Journal of Geophysical Research: Space Physics*, 104(A4):6899–6917.
- Horbury, T. S., Balogh, A., Forsyth, R. J., and Smith, E. J. (1996). The rate of turbulent evolution over the Sun’s poles. *Astronomy and Astrophysics*, 316:333–341.
- Horbury, T. S., Forman, M., and Oughton, S. (2008). Anisotropic Scaling of Magnetohydrodynamic Turbulence. *Physical Review Letters*, 101(17):175005.
- Hu, Q. (2017). The grad-shafranov reconstruction in twenty years: 1996–2016. *Science China Earth Sciences*.
- Hu, Q., Qiu, J., Dasgupta, B., Khare, A., and Webb, G. M. (2014). Structures of interplanetary magnetic flux ropes and comparison with their solar sources. *The Astrophysical Journal*, 793(1):53.

- Hu, Q., Qiu, J., and Krucker, S. (2015). Magnetic field line lengths inside interplanetary magnetic flux ropes. *Journal of Geophysical Research: Space Physics*, 120(7):5266–5283.
- Hu, Q. and Sonnerup, B. U. O. (2002). Reconstruction of magnetic clouds in the solar wind: Orientations and configurations. *Journal of Geophysical Research: Space Physics*, 107(A7):SSH 10–1–SSH 10–15.
- Hu, Q., Zheng, J., Chen, Y., le Roux, J., and Zhao, L. (2018). Automated detection of small-scale magnetic flux ropes in the solar wind: First results from the Wind spacecraft measurements. *The Astrophysical Journal Supplement Series*, 239:12.
- Karimabadi, H., Roytershteyn, V., Vu, H. X., Omelchenko, Y. A., Scudder, J., Daughton, W., Dimmock, A., Nykyri, K., Wan, M., Sibeck, D., Tatineni, M., Majumdar, A., Loring, B., and Geveci, B. (2014). The link between shocks, turbulence, and magnetic reconnection in collisionless plasmas. *Physics of Plasmas*, 21(6):062308.
- Kruparova, O., Krupar, V., Šafránková, J., Němeček, Z., Maksimovic, M., Santolík, O., Soucek, J., Němec, F., and Merka, J. (2019). Statistical survey of the terrestrial bow shock observed by the Cluster spacecraft. *Journal of Geophysical Research: Space Physics*, 124(3):1539–1547.
- Lalti, A., Khotyaintsev, Y. V., Dimmock, A. P., Johlander, A., Graham, D. B., and Olshevsky, V. (2022). A database of MMS bow shock crossings compiled using machine learning. *Journal of Geophysical Research: Space Physics*, 127(8):e2022JA030454. e2022JA030454 2022JA030454.
- le Roux, J. A. (2023). Parallel and momentum superdiffusion of energetic particles interacting with small-scale magnetic flux ropes in the large-scale solar wind. *The Astrophysical Journal*, 945(1):60.
- le Roux, J. A. and Zank, G. P. (2021). A focused transport-based kinetic fractional diffusion-advection equation for energetic particle trapping and reconnection-related acceleration by small-scale magnetic flux ropes in the solar wind. *The Astrophysical Journal*, 913(2):84.

- Matthaeus, W. and Goldstein, M. (1982). Measurement of the rugged invariants of magnetohydrodynamic turbulence. *Journal of Geophysical Research*, 87.
- Matthaeus, W. H., Wan, M., Servidio, S., Greco, A., Osman, K. T., Oughton, S., and Dmitruk, P. (2015). Intermittency, nonlinear dynamics and dissipation in the solar wind and astrophysical plasmas. *Philosophical Transactions of the Royal Society A: Mathematical, Physical and Engineering Sciences*, 373(2041):20140154.
- McCracken, K. G. (1967). Particles and fields in the interplanetary medium. *Proceedings of the National Academy of Sciences of the United States of America*, 58 6:2149–53.
- McFadden, J., Carlson, C., Larson, D., Ludlam, M., Abiad, R., Elliott, B., Turin, P., Marckwardt, M., and Angelopoulos, V. (2008). The THEMIS ESA plasma instrument and in-flight calibration. *Space Science Reviews*, 141:277–302.
- Nakanotani, M., Zank, G. P., and Zhao, L. (2022a). Particle acceleration in an mhd-scale system of multiple current sheets. *Frontiers in Astronomy and Space Sciences*, Volume 9 - 2022.
- Nakanotani, M., Zank, G. P., and Zhao, L.-L. (2022b). Turbulence-dominated shock waves: 2d hybrid kinetic simulations. *The Astrophysical Journal*, 926(2):109.
- Nykyri, K. and Otto, A. (2001). Plasma transport at the magnetospheric boundary due to reconnection in Kelvin-Helmholtz vortices. *Geophysical Research Letters*, 28(18):3565–3568.
- Parker, E. (1958). Dynamics of the interplanetary gas and magnetic fields. *The Astrophysical Journal*, 128:664.
- Pecora, F., Greco, A., Hu, Q., Servidio, S., Chasapis, A., and Matthaeus, W. (2019). Single-spacecraft identification of flux tubes and current sheets in the solar wind. *The Astrophysical Journal*, 881:L11.
- Pollock, C., Moore, T., Jacques, A., Burch, J., Gliese, U., Saito, Y., Omoto, T., Avanov, L., Barrie, A., Coffey, V., Dorelli, J., Gershman, D., Giles, B., Rosnack, T., Salo, C., Yokota, S., Adrian, M., Aouston, C., Auletta, C., Aung, S., Bigio, V., Cao, N., Chandler, M., Chornay, D., Christian, K., Clark, G.,

Collinson, G., Corris, T., De Los Santos, A., Devlin, R., Diaz, T., Dickerson, T., Dickson, C., Diekmann, A., Diggs, F., Duncan, C., Figueroa-Vinas, A., Firman, C., Freeman, M., Galassi, N., Garcia, K., Goodhart, G., Guererro, D., Hageman, J., Hanley, J., Hemminger, E., Holland, M., Hutchins, M., James, T., Jones, W., Kreisler, S., Kujawski, J., Lavu, V., Lobell, J., LeCompte, E., Lukemire, A., MacDonald, E., Mariano, A., Mukai, T., Narayanan, K., Nguyan, Q., Onizuka, M., Paterson, W., Persyn, S., Piepgrass, B., Cheney, F., Rager, A., Raghuram, T., Ramil, A., Reichenthal, L., Rodriguez, H., Rouzaud, J., Rucker, A., Saito, Y., Samara, M., Sauvaud, J.-A., Schuster, D., Shappirio, M., Shelton, K., Sher, D., Smith, D., Smith, K., Smith, S., Steinfeld, D., Szymkiewicz, R., Tanimoto, K., Taylor, J., Tucker, C., Tull, K., Uhl, A., Vloet, J., Walpole, P., Weidner, S., White, D., Winkert, G., Yeh, P.-S., and Zeuch, M. (2016). Fast plasma investigation for magnetospheric multiscale. *Space Science Reviews*, 199:331–406.

Shaikh, Z. I. and Raghav, A. N. (2022). Evolution of Earth’s magnetosheath as a planar magnetic structure. *Monthly Notices of the Royal Astronomical Society*, 511(4):4963–4970.

Shue, J.-H., Chao, J. K., Fu, H. C., Russell, C. T., Song, P., Khurana, K. K., and Singer, H. J. (1997). A new functional form to study the solar wind control of the magnetopause size and shape. *Journal of Geophysical Research: Space Physics*, 102(A5):9497–9511.

Slavin, J. A., Holzer, R. E., Spreiter, J. R., and Stahara, S. S. (1984). Planetary mach cones: Theory and observation. *Journal of Geophysical Research: Space Physics*, 89(A5):2708–2714.

Sonnerup, B., Hasegawa, H., Teh, W.-L., and Hau, L.-N. (2006). Grad-shafranov reconstruction: An overview. *Journal of Geophysical Research*, 111.

Sonnerup, B. U. O. and Guo, M. (1996). Magnetopause transects. *Geophysical Research Letters*, 23(25):3679–3682.

Taylor, G. (1938). The spectrum of turbulence. *Proceedings of the Royal Society of London. Series A - Mathematical and Physical Sciences*, 164(919):476–490.

- Teh, W.-L. (2018). Grad–shafranov reconstruction of magnetohydrostatic equilibria with nonisotropic plasma pressure: the theory. *Earth, Planets and Space*, 70.
- Telloni, D., Bruno, R., D’Amicis, R., Pietropaolo, E., and Carbone, V. (2012). Wavelet analysis as a tool to localize magnetic and cross-helicity events in the solar wind. *The Astrophysical Journal*, 751:19.
- Telloni, D., Perri, S., Bruno, R., Carbone, V., and D’Amicis, R. (2013). An analysis of magnetohydrodynamic invariants of magnetic fluctuations within interplanetary flux ropes. *The Astrophysical Journal*, 776.
- Torbert, R., Russell, C., Magnes, W., Ergun, R., Lindqvist, P.-A., LeContel, O., Vaith, H., Macri, J., Myers, S., Rau, D., Needell, J., King, B., Granoff, M., Chutter, M., Dors, I., Olsson, G., Khotyaintsev, Y., Eriksson, A., Kletzing, C. A., Bounds, S., Anderson, B., Baumjohann, W., Steller, M., Bromund, K., Le, G., Nakamura, R., Strangeway, R., Leinweber, H., Tucker, S., Westfall, J., Fischer, D., Plaschke, F., Porter, J., and Lappalainen, K. (2016). The FIELDS instrument suite on MMS: Scientific objectives, measurements, and data products. *Space Science Reviews*, 199:105–135.
- Torrence, C. and Compo, G. P. (1998). A practical guide to wavelet analysis. *Bulletin of the American Meteorological society*, 79(1):61–78.
- Toy-Edens, V., Mo, W., Raptis, S., and Turner, D. L. (2024a). 8 years of day-side Magnetospheric Multiscale (MMS) unsupervised clustering plasma regions classifications.
- Toy-Edens, V., Mo, W., Raptis, S., and Turner, D. L. (2024b). Classifying 8 years of MMS day-side plasma regions via unsupervised machine learning. *Journal of Geophysical Research: Space Physics*, 129(6):e2024JA032431. e2024JA032431 2024JA032431.
- Trotta, D., Pecora, F., Settino, A., Perrone, D., Hietala, H., Horbury, T., Matthaeus, W., Burgess, D., Servidio, S., and Valentini, F. (2022). On the transmission of turbulent structures across the earth’s bow shock. *The Astrophysical Journal*, 933(2):167.

- Tsurutani, B. T., Goldstein, B. E., Smith, E. J., Gonzalez, W. D., Tang, F., Akasofu, S. I., and Anderson, R. R. (1990). The interplanetary and solar causes of geomagnetic activity. *Planetary and Space Science*, 38(1):109–126.
- University of California, Berkeley; NASA (2012). THEMIS (time history of events and macroscale interactions during substorms). <https://www.eoportal.org/satellite-missions/themis#eop-quick-facts-section>.
- Williams, D. (1981). Ring current composition and sources: An update. *Planetary and Space Science*, 29(11):1195–1203.
- Yordanova, E., Vörös, Z., Raptis, S., and Karlsson, T. (2020). Current sheet statistics in the magnetosheath. *Frontiers in Astronomy and Space Sciences*, 7.
- Zank, G., Adhikari, L., Hunana, P., Shiota, D., Bruno, R., and Telloni, D. (2017). Theory and transport of nearly incompressible magnetohydrodynamic turbulence. *The Astrophysical Journal*, 835:147.
- Zank, G., Nakanotani, M., Zhao, L., Du, S., Adhikari, L., Che, H., and le Roux, J. (2021a). Flux ropes, turbulence, and collisionless perpendicular shock waves: High plasma beta case. *The Astrophysical Journal*, 913:127.
- Zank, G. P., Zhao, L.-L., Adhikari, L., Telloni, D., Kasper, J. C., and Bale, S. D. (2021b). Turbulence transport in the solar corona: Theory, modeling, and Parker Solar Probe. *Physics of Plasmas*, 28(8):080501.
- Zhao, L., Zank, G., Adhikari, L., Hu, Q., Kasper, J., Bale, S., Korreck, K., Case, A., Bonnell, J., Dudok de Wit, T., Goetz, K., Harvey, P., Macdowall, R., Malaspina, D., Pulupa, M., Larson, D., Livi, R., Whittlesey, P., and Klein, K. (2020). Identification of magnetic flux ropes from Parker Solar Probe observations during the first encounter. *The Astrophysical Journal Supplement Series*, 246:26.
- Zhao, L.-L., Zank, G. P., Adhikari, L., and Nakanotani, M. (2022). Inertial-range magnetic-fluctuation anisotropy observed from Parker Solar Probe's first seven orbits. *The Astrophysical Journal Letters*, 924(1):L5.
- Zhao, L.-L., Zank, G. P., Hu, Q., Telloni, D., Chen, Y., Adhikari, L., Nakanotani, M., Kasper, J. C., Huang, J., Bale, S. D., Korreck, K. E., Case, A. W., Stevens, M., Bonnell, J. W., Dudok de Wit, T., Goetz, K., Harvey, P. R., MacDowall,

R. J., Malaspina, D. M., Pulupa, M., Larson, D. E., Livi, R., Whittlesey, P., Klein, K. G., and Raouafi, N. E. (2021). Detection of small magnetic flux ropes from the third and fourth Parker Solar Probe encounters. *Astronomy & Astrophysics*, 650:A12.

Zheng, J. and Hu, Q. (2018). Observational evidence for self-generation of small-scale magnetic flux ropes from intermittent solar wind turbulence. *The Astrophysical Journal*, 852(2):L23.

Appendix A: Summary of observation intervals

Table A.1: Periods of data across 1051 hours in the magnetosheath from THEMIS and MMS probes

		Start	End	Probe	# Hours	Events
13 May 2008	2008-05-13 00:04:18.0946	2008-05-13 05:24:58.1467	THM-C	5.344	86	
16-17 May 2008	2008-05-16 20:00:40.8048	2008-05-17 06:27:58.8540	THM-C	10.455	210	
22 May 2008	2008-05-22 12:02:32.3340	2008-05-22 21:59:55.6656	THM-C	9.956	159	
28-29 May 2008	2008-05-28 12:05:27.8539	2008-05-29 05:59:58.7792	THM-C	17.908	246	
1-2 Jun 2008	2008-06-01 08:03:03.5541	2008-06-02 03:59:58.6605	THM-C	19.949	260	
31 May 2009	2009-05-31 02:04:31.7145	2009-05-31 16:12:58.5210	THM-C	14.141	295	
4 Jun 2009	2009-06-04 02:03:56.0925	2009-06-04 20:46:58.0740	THM-C	18.717	233	
8 Jun 2009	2009-06-08 02:01:11.6000	2009-06-08 21:59:58.1120	THM-C	19.979	396	
10 Jun 2009	2009-06-10 02:00:06.7896	2009-06-10 15:59:57.9210	THM-C	13.998	190	
12 Jun 2009	2009-06-12 00:06:08.0568	2009-06-12 23:59:58.3656	THM-C	23.897	304	
14 Jun 2009	2009-06-14 00:02:43.2510	2009-06-14 17:59:58.7742	THM-C	17.954	140	
16 Jun 2009	2009-06-16 00:07:40.0400	2009-06-16 23:59:58.4800	THM-C	23.872	184	
19-20 Jun 2009	2009-06-19 22:00:39.0672	2009-06-20 23:59:56.7312	THM-C	25.988	233	
8 Sep 2015	2015-09-08 10:43:03.0000	2015-09-08 17:59:55.5000	MMS-1	7.281	97	
1 Oct 2015	2015-10-01 06:53:01.5000	2015-10-01 17:23:55.5000	MMS-1	10.515	79	
7 Oct 2015	2015-10-07 06:02:01.5000	2015-10-07 11:19:57.0000	MMS-1	5.299	53	
12 Oct 2015	2015-10-12 06:21:58.5000	2015-10-12 17:12:58.5000	MMS-1	10.850	68	
13 Oct 2015	2015-10-13 05:39:00.0000	2015-10-13 11:09:58.5000	MMS-1	5.516	91	
15 Oct 2015	2015-10-15 06:48:00.0000	2015-10-15 13:30:58.5000	MMS-1	6.716	60	
17 Oct 2015	2015-10-17 04:55:57.0000	2015-10-17 16:01:57.0000	MMS-1	11.100	83	
18 Oct 2015	2015-10-18 04:49:25.5000	2015-10-18 15:06:58.5000	MMS-1	10.293	69	
20 Oct 2015	2015-10-20 05:55:57.0000	2015-10-20 17:10:57.0000	MMS-1	11.250	99	
22 Oct 2015	2015-10-22 06:06:00.0000	2015-10-22 14:53:55.5000	MMS-1	8.799	83	
23 Oct 2015	2015-10-23 08:21:00.0000	2015-10-23 15:39:58.5000	MMS-1	7.316	70	
29 Oct 2015	2015-10-29 04:39:58.5000	2015-10-29 14:59:55.5000	MMS-1	10.332	75	
30 Oct 2015	2015-10-30 05:15:58.5000	2015-10-30 16:04:57.0000	MMS-1	10.816	75	

31 Oct	2015	2015-10-31	07:17:01.5000	2015-10-31	15:53:55.5000	MMS-1	8.615	91
1 Nov	2015	2015-11-01	03:24:00.0000	2015-11-01	15:06:58.5000	MMS-1	11.716	119
2 Nov	2015	2015-11-02	04:00:00.0000	2015-11-02	11:59:55.5000	MMS-1	7.999	57
4 Nov	2015	2015-11-04	08:06:00.0000	2015-11-04	15:30:58.5000	MMS-1	7.416	59
5 Nov	2015	2015-11-05	07:06:00.0000	2015-11-05	14:21:58.5000	MMS-1	7.266	72
10 Nov	2015	2015-11-10	02:48:58.5000	2015-11-10	08:36:58.5000	MMS-1	5.800	60
13 Nov	2015	2015-11-13	04:54:00.0000	2015-11-13	10:21:58.5000	MMS-1	5.466	60
14 Nov	2015	2015-11-14	03:13:57.0000	2015-11-14	12:35:55.5000	MMS-1	9.366	74
6 Dec	2015	2015-12-06	08:14:01.5000	2015-12-06	13:30:58.5000	MMS-1	5.282	157
25 Oct	2016	2016-10-25	09:44:28.5000	2016-10-25	18:24:58.5000	MMS-1	8.675	79
3 Nov	2016	2016-11-03	08:39:18.0000	2016-11-03	15:03:58.5000	MMS-1	6.411	96
8 Nov	2016	2016-11-08	09:35:01.5000	2016-11-08	14:39:58.5000	MMS-1	5.082	58
10 Nov	2016	2016-11-10	08:16:57.0000	2016-11-10	16:59:55.5000	MMS-1	8.716	71
11 Nov	2016	2016-11-11	09:11:01.5000	2016-11-11	18:27:58.5000	MMS-1	9.283	69
12 Nov	2016	2016-11-12	07:42:58.5000	2016-11-12	17:48:58.5000	MMS-1	10.100	89
19 Nov	2016	2016-11-19	08:00:00.0000	2016-11-19	17:50:55.5000	MMS-1	9.849	62
20 Nov	2016	2016-11-20	11:27:58.5000	2016-11-20	17:20:55.5000	MMS-1	5.883	51
21 Nov	2016	2016-11-21	11:56:01.5000	2016-11-21	19:20:55.5000	MMS-1	7.415	74
22 Nov	2016	2016-11-22	06:43:57.0000	2016-11-22	18:20:55.5000	MMS-1	11.616	85
23 Nov	2016	2016-11-23	10:33:00.0000	2016-11-23	16:47:55.5000	MMS-1	6.249	71
24 Nov	2016	2016-11-24	06:14:10.5000	2016-11-24	18:35:55.5000	MMS-1	12.363	88
27 Nov	2016	2016-11-27	06:58:03.0000	2016-11-27	12:47:55.5000	MMS-1	5.831	61
1 Dec	2016	2016-12-01	06:32:01.5000	2016-12-01	16:53:55.5000	MMS-1	10.365	65
3 Dec	2016	2016-12-03	07:15:00.0000	2016-12-03	16:14:55.5000	MMS-1	8.999	106
4 Dec	2016	2016-12-04	06:15:59.0013	2016-12-04	17:35:56.9079	MMS-1	11.332	111
5 Dec	2016	2016-12-05	04:54:22.5000	2016-12-05	12:47:55.5000	MMS-1	7.893	68
7 Dec	2016	2016-12-07	05:12:58.5000	2016-12-07	14:36:58.5000	MMS-1	9.400	79
8 Dec	2016	2016-12-08	10:03:58.5000	2016-12-08	15:58:57.0000	MMS-1	5.916	65

9 Dec 2016	2016-12-09 11:48:58.5000	2016-12-09 17:56:55.5000	MMS-1	6.133	37
11 Dec 2016	2016-12-11 09:46:57.0000	2016-12-11 15:42:58.5000	MMS-1	5.934	40
18 Dec 2016	2016-12-18 07:51:00.0000	2016-12-18 14:36:58.5000	MMS-1	6.766	74
24 Dec 2016	2016-12-24 07:36:00.0000	2016-12-24 14:51:58.5000	MMS-1	7.266	59
3 Oct 2017	2017-10-03 12:00:00.0000	2017-10-03 18:59:55.5000	MMS-1	6.999	188
6 Oct 2017	2017-10-06 14:10:07.5000	2017-10-06 17:59:55.5000	MMS-1	3.830	720
5 Nov 2017	2017-11-05 03:30:00.0000	2017-11-05 11:59:55.5000	MMS-1	8.499	113
8 Nov 2017	2017-11-08 01:30:00.0000	2017-11-08 05:59:55.5000	MMS-1	4.499	56
14 Nov 2017	2017-11-14 15:00:00.0000	2017-11-14 19:57:58.5000	MMS-1	4.966	36
22 Nov 2017	2017-11-22 05:38:01.5000	2017-11-22 10:55:57.0000	MMS-1	5.299	58
25 Nov 2017	2017-11-25 01:26:01.5000	2017-11-25 07:09:58.5000	MMS-1	5.732	67
30 Nov 2017	2017-11-30 16:23:01.5000	2017-11-30 23:01:57.0000	MMS-1	6.649	57
3 Dec 2017	2017-12-03 11:16:30.0000	2017-12-03 18:47:55.5000	MMS-1	7.524	80
9 Dec 2017	2017-12-09 03:15:27.0000	2017-12-09 08:28:57.0000	MMS-1	5.225	55
13 Sep 2018	2018-09-13 17:02:03.1612	2018-09-13 21:59:55.9729	THM-E	4.964	51
14-15 Sep 2018	2018-09-14 14:00:01.5774	2018-09-15 03:52:27.7438	THM-E	13.874	86
21 Oct 2018	2018-10-21 10:00:58.5000	2018-10-21 19:23:55.5000	MMS-1	9.383	83
24 Oct 2018	2018-10-24 07:59:01.5000	2018-10-24 16:01:57.0000	MMS-1	8.049	74
27 Oct 2018	2018-10-27 04:19:57.0000	2018-10-27 23:56:55.5000	MMS-1	19.616	166
30 Oct 2018	2018-10-30 00:24:00.0000	2018-10-30 05:24:58.5000	MMS-1	5.016	50
1 Nov 2018	2018-11-01 16:53:01.5000	2018-11-01 23:59:55.5000	MMS-1	7.115	72
4 Nov 2018	2018-11-04 11:50:01.5000	2018-11-04 17:29:55.5000	MMS-1	5.665	32
10 Nov 2018	2018-11-10 16:35:01.5000	2018-11-10 23:57:58.5000	MMS-1	7.383	33
13 Nov 2018	2018-11-13 12:24:00.0000	2018-11-13 19:29:55.5000	MMS-1	7.099	68
14 Nov 2018	2018-11-14 17:42:58.5000	2018-11-14 23:06:58.5000	MMS-1	5.400	74
17 Nov 2018	2018-11-17 12:23:01.5000	2018-11-17 19:36:58.5000	MMS-1	7.232	65
21 Nov 2018	2018-11-21 08:48:58.5000	2018-11-21 17:17:55.5000	MMS-1	8.482	96
23 Nov 2018	2018-11-23 09:15:00.0000	2018-11-23 15:03:58.5000	MMS-1	5.816	59

26 Nov 2018	2018-11-26 00:29:01.5000	2018-11-26 09:08:55.5000	MMS-1	8.665	79
29 Nov 2018	2018-11-29 00:09:00.0000	2018-11-29 06:06:58.5000	MMS-1	5.966	66
21 Dec 2018	2018-12-21 13:57:00.0000	2018-12-21 19:10:57.0000	MMS-1	5.232	72
26 Oct 2019	2019-10-26 06:39:00.0000	2019-10-26 12:27:58.5000	MMS-1	5.816	53
2 Nov 2019	2019-11-02 08:48:00.0000	2019-11-02 18:04:57.0000	MMS-1	9.283	118
6 Nov 2019	2019-11-06 11:36:00.0000	2019-11-06 23:26:55.5000	MMS-1	11.849	61
9 Nov 2019	2019-11-09 08:50:01.5000	2019-11-09 15:17:55.5000	MMS-1	6.465	82
13 Nov 2019	2019-11-13 00:00:04.5000	2019-11-13 07:52:57.0000	MMS-1	7.881	53
19 Nov 2019	2019-11-19 18:15:00.0000	2019-11-19 23:59:55.5000	MMS-1	5.749	47
23 Nov 2019	2019-11-23 07:32:01.5000	2019-11-23 13:23:55.5000	MMS-1	5.865	50
6 Dec 2019	2019-12-06 07:05:01.5000	2019-12-06 16:02:55.5000	MMS-1	8.965	123
10 Dec 2019	2019-12-10 00:00:04.5000	2019-12-10 05:25:57.0000	MMS-1	5.431	72
13 Dec 2019	2019-12-13 09:42:58.5000	2019-12-13 15:18:58.5000	MMS-1	5.600	54
17 Dec 2019	2019-12-17 00:00:04.5000	2019-12-17 03:59:55.5000	MMS-1	3.998	63
24 Dec 2019	2019-12-24 00:00:04.5000	2019-12-24 05:44:55.5000	MMS-1	5.747	46
31 Oct 2020	2020-10-31 10:47:01.5000	2020-10-31 15:04:57.0000	MMS-1	4.299	38
14 Nov 2020	2020-11-14 08:37:03.0000	2020-11-14 17:21:58.5000	MMS-1	8.749	80
2 Dec 2020	2020-12-02 00:00:04.5000	2020-12-02 08:59:55.5000	MMS-1	8.998	63
7 Dec 2020	2020-12-07 16:30:00.0000	2020-12-07 23:59:55.5000	MMS-1	7.499	63
11 Dec 2020	2020-12-11 07:12:00.0000	2020-12-11 14:09:58.5000	MMS-1	6.966	73
7 Nov 2021	2021-11-07 04:12:00.0000	2021-11-07 14:05:55.5000	MMS-1	9.899	157
14 Nov 2021	2021-11-14 03:30:00.0000	2021-11-14 10:24:58.5000	MMS-1	6.916	47
28 Nov 2021	2021-11-28 12:17:02.4827	2021-11-28 19:15:55.5412	MMS-1	6.981	54
1 Dec 2021	2021-12-01 16:48:58.5000	2021-12-01 22:19:57.0000	MMS-1	5.516	64
18 Dec 2021	2021-12-18 06:48:58.5000	2021-12-18 14:42:58.5000	MMS-1	7.900	88
22 Dec 2021	2021-12-22 18:36:58.5000	2021-12-22 23:59:55.5000	MMS-1	5.383	48
1 Jan 2022	2022-01-01 04:02:01.5000	2022-01-01 17:37:57.0000	MMS-1	13.599	116
5 Jan 2022	2022-01-05 00:00:04.5000	2022-01-05 05:59:55.5000	MMS-1	5.997	59

5 Jan 2022	2022-01-05 00:01:49.6800	2022-01-05 05:59:58.7340	THM-A	5.969	43
6 Jan 2022	2022-01-06 00:05:40.0080	2022-01-06 05:59:58.7340	THM-A	5.905	91
7 Jan 2022	2022-01-07 06:05:33.2580	2022-01-07 11:59:57.4680	THM-A	5.907	68
12 Jan 2022	2022-01-12 03:15:00.0000	2022-01-12 07:59:55.5000	MMS-1	4.749	41
8 Nov 2022	2022-11-08 00:00:04.5000	2022-11-08 07:51:58.5000	MMS-1	7.865	90
11 Nov 2022	2022-11-11 11:30:00.0000	2022-11-11 19:46:57.0000	MMS-1	8.283	40
18 Nov 2022	2022-11-18 10:44:01.5000	2022-11-18 16:59:55.5000	MMS-1	6.265	51
22 Nov 2022	2022-11-22 01:15:00.0000	2022-11-22 05:24:58.5000	MMS-1	4.166	71
25 Nov 2022	2022-11-25 09:45:58.5000	2022-11-25 17:54:58.5000	MMS-1	8.150	72
2 Dec 2022	2022-12-02 12:48:00.0000	2022-12-02 18:16:57.0000	MMS-1	5.482	74
13 Dec 2022	2022-12-13 08:30:00.0000	2022-12-13 13:40:57.0000	MMS-1	5.183	55
15 Dec 2022	2022-12-15 08:07:57.0000	2022-12-15 20:17:55.5000	MMS-1	12.166	86
20 Dec 2022	2022-12-20 07:12:58.5000	2022-12-20 16:43:57.0000	MMS-1	9.516	51
22 Dec 2022	2022-12-22 15:01:57.0000	2022-12-22 21:29:55.5000	MMS-1	6.466	46
27 Dec 2022	2022-12-27 00:00:04.5000	2022-12-27 06:00:58.5000	MMS-1	6.015	49
29 Dec 2022	2022-12-29 18:06:01.4480	2022-12-29 23:59:57.4199	MMS-1	5.899	80
2 Jan 2023	2023-01-02 02:48:00.0000	2023-01-02 09:40:57.0000	MMS-1	6.883	82
5 Jan 2023	2023-01-05 16:25:03.0000	2023-01-05 22:54:58.5000	MMS-1	6.499	69
6 Jan 2023	2023-01-06 12:24:00.0000	2023-01-06 19:54:58.5000	MMS-1	7.516	47
9 Jan 2023	2023-01-09 04:19:03.0000	2023-01-09 10:59:55.5000	MMS-1	6.681	58
23 Jan 2023	2023-01-23 08:10:03.6534	2023-01-23 12:19:57.9866	MMS-1	4.165	38

Table A.2: Periods of data across 676 hours in the solar wind from THEMIS and MMS probes

		Start	End	Probe	# Hours	Events
13 May 2008		2008-05-13 00:05:12.0000	2008-05-13 11:59:57.0000	THM-B	11.912	157
16-17 May 2008		2008-05-16 20:00:39.0000	2008-05-17 09:59:57.0000	THM-B	13.988	298
22 May 2008		2008-05-22 12:02:31.4450	2008-05-22 21:59:56.6398	THM-B	9.957	132
28-29 May 2008		2008-05-28 18:02:26.1648	2008-05-29 05:59:57.5998	THM-B	11.959	182
1-2 Jun 2008		2008-06-01 08:01:30.9630	2008-06-02 03:59:57.3598	THM-B	19.974	256
31 May 2009		2009-05-31 02:01:56.8480	2009-05-31 20:59:57.5310	THM-B	18.967	295
4 Jun 2009		2009-06-04 02:01:24.1835	2009-06-04 22:59:58.5685	THM-B	20.976	220
8 Jun 2009		2009-06-08 02:02:19.8640	2009-06-08 21:59:58.1120	THM-B	19.961	262
10 Jun 2009		2009-06-10 02:02:57.7022	2009-06-10 15:59:57.1216	THM-B	13.950	155
12 Jun 2009		2009-06-12 00:06:05.0271	2009-06-12 23:59:58.6501	THM-B	23.898	309
14 Jun 2009		2009-06-14 00:05:05.6731	2009-06-14 17:59:59.7295	THM-B	17.915	140
16 Jun 2009		2009-06-16 00:06:11.0000	2009-06-16 23:59:58.4800	THM-B	23.896	280
19-20 Jun 2009		2009-06-19 22:00:46.1956	2009-06-20 23:59:57.1872	THM-B	25.986	269
24 Oct 2017		2017-10-24 08:14:01.5000	2017-10-24 13:42:58.5000	MMS-1	5.482	57
1 Nov 2017		2017-11-01 03:24:58.5000	2017-11-01 22:32:55.5000	MMS-1	19.133	111
7 Nov 2017		2017-11-07 00:00:00.0000	2017-11-07 10:24:58.5000	MMS-1	10.416	63
4 Dec 2017		2017-12-04 09:27:00.0000	2017-12-04 14:43:57.0000	MMS-1	5.282	51
22 Dec 2017		2017-12-22 05:40:25.5000	2017-12-22 10:45:58.5000	MMS-1	5.093	35
30 Dec 2017		2017-12-30 13:24:22.5000	2017-12-30 19:01:57.0000	MMS-1	5.626	50
2 Jan 2018		2018-01-02 08:30:27.0000	2018-01-02 14:14:55.5000	MMS-1	5.741	77
8 Jan 2018		2018-01-08 03:23:28.5000	2018-01-08 06:39:58.5000	MMS-1	3.275	20
13 Sep 2018		2018-09-13 17:05:39.0000	2018-09-13 21:59:56.5904	THM-C	4.905	38
14-15 Sep 2018		2018-09-14 19:24:10.8676	2018-09-15 03:59:56.7794	THM-C	8.596	90
27 Nov 2018		2018-11-27 06:07:03.0000	2018-11-27 11:49:57.0000	MMS-1	5.715	63
16 Nov 2019		2019-11-16 14:06:00.0000	2019-11-16 21:14:55.5000	MMS-1	7.149	44
26 Jan 2020		2020-01-26 02:16:03.0000	2020-01-26 08:57:58.5000	MMS-1	6.699	59

27 Jan 2020	2020-01-27 01:22:03.0000	2020-01-27 12:25:57.0000	MMS-1	11.065	68
30 Jan 2020	2020-01-30 13:02:01.5000	2020-01-30 18:43:57.0000	MMS-1	5.699	65
3 Feb 2020	2020-02-03 09:06:58.5000	2020-02-03 16:29:55.5000	MMS-1	7.383	81
25 Nov 2020	2020-11-25 03:17:01.5000	2020-11-25 10:07:57.0000	MMS-1	6.849	59
12 Dec 2020	2020-12-12 11:48:58.5000	2020-12-12 18:51:58.5000	MMS-1	7.050	48
17 Dec 2020	2020-12-17 00:51:09.0000	2020-12-17 07:37:57.0000	MMS-1	6.780	56
19 Dec 2020	2020-12-19 08:51:58.5000	2020-12-19 14:03:58.5000	MMS-1	5.200	50
27 Dec 2020	2020-12-27 13:26:19.5000	2020-12-27 21:39:58.5000	MMS-1	8.227	69
31 Dec 2020	2020-12-31 04:01:03.0000	2020-12-31 09:49:57.0000	MMS-1	5.815	44
10 Jan 2021	2021-01-10 14:11:10.5000	2021-01-10 23:19:57.0000	MMS-1	9.146	61
17 Jan 2021	2021-01-17 00:00:04.5000	2021-01-17 23:59:55.5000	MMS-1	23.997	177
18 Jan 2021	2021-01-18 00:00:04.5000	2021-01-18 15:14:55.5000	MMS-1	15.248	99
20 Jan 2021	2021-01-20 11:51:04.5000	2021-01-20 23:59:55.5000	MMS-1	12.148	75
21 Jan 2021	2021-01-21 02:51:58.5000	2021-01-21 15:25:57.0000	MMS-1	12.566	99
24 Jan 2021	2021-01-24 09:51:00.0000	2021-01-24 23:59:55.5000	MMS-1	14.149	106
25 Jan 2021	2021-01-25 00:00:00.0000	2021-01-25 15:44:55.5000	MMS-1	15.749	117
28 Jan 2021	2021-01-28 06:28:57.5186	2021-01-28 11:51:59.4493	MMS-1	5.384	44
4 Feb 2021	2021-02-04 06:39:00.0000	2021-02-04 12:25:57.0000	MMS-1	5.782	58
28 Nov 2021	2021-11-28 12:17:02.4827	2021-11-28 19:15:55.5412	MMS-1	6.981	44
12 Dec 2021	2021-12-12 10:26:02.3347	2021-12-12 19:00:55.5212	MMS-1	8.581	47
19 Dec 2021	2021-12-19 10:33:59.3453	2021-12-19 18:14:56.9599	MMS-1	7.683	66
20 Dec 2021	2021-12-20 11:46:07.5000	2021-12-20 17:44:55.5000	MMS-1	5.980	44
26 Dec 2021	2021-12-26 10:39:00.8520	2021-12-26 17:26:56.8959	MMS-1	6.799	59
3 Jan 2022	2022-01-03 15:42:00.0000	2022-01-03 20:44:55.5000	MMS-1	5.049	36
4 Jan 2022	2022-01-04 13:26:10.5000	2022-01-04 19:34:57.0000	MMS-1	6.146	41
5 Jan 2022	2022-01-05 00:06:17.9600	2022-01-05 05:59:55.2600	THM-B	5.894	25
6 Jan 2022	2022-01-06 00:06:35.1400	2022-01-06 05:59:55.2600	THM-B	5.889	44
6 Jan 2022	2022-01-06 03:08:24.0000	2022-01-06 11:59:55.5000	MMS-1	8.859	65

7 Jan 2022	2022-01-07 06:00:00.0000	2022-01-07 11:59:55.5000	MMS-1	5.999	39
7 Jan 2022	2022-01-07 06:00:08.1450	2022-01-07 11:59:54.8150	THM-B	5.996	52
11 Jan 2022	2022-01-11 14:51:09.0000	2022-01-11 20:21:58.5000	MMS-1	5.514	38
13 Jan 2022	2022-01-13 04:00:00.0000	2022-01-13 09:16:57.0000	MMS-1	5.282	48
4 Feb 2022	2022-02-04 08:51:04.5000	2022-02-04 14:49:57.0000	MMS-1	5.981	28
5 Feb 2022	2022-02-05 07:26:10.5000	2022-02-05 15:39:58.5000	MMS-1	8.230	63
11 Feb 2022	2022-02-11 10:06:09.0000	2022-02-11 16:04:57.0000	MMS-1	5.980	32
19 Feb 2022	2022-02-19 09:33:00.0000	2022-02-19 15:48:58.5000	MMS-1	6.266	40
30 Nov 2022	2022-11-30 02:36:04.5000	2022-11-30 08:34:57.0000	MMS-1	5.981	75
7 Dec 2022	2022-12-07 03:31:03.0000	2022-12-07 09:29:55.5000	MMS-1	5.981	37
13 Dec 2022	2022-12-13 08:30:00.0000	2022-12-13 13:40:57.0000	MMS-1	5.183	42
14 Dec 2022	2022-12-14 06:45:58.5000	2022-12-14 12:40:57.0000	MMS-1	5.916	38
18 Dec 2022	2022-12-18 15:26:01.5000	2022-12-18 23:36:58.5000	MMS-1	8.182	41
20 Dec 2022	2022-12-20 07:12:58.5000	2022-12-20 16:43:57.0000	MMS-1	9.516	52
5 Jan 2023	2023-01-05 16:25:03.0000	2023-01-05 22:54:58.5000	MMS-1	6.499	24
12 Jan 2023	2023-01-12 06:48:00.0000	2023-01-12 11:55:57.0000	MMS-1	5.133	37
13 Jan 2023	2023-01-13 16:00:58.5000	2023-01-13 22:32:55.5000	MMS-1	6.532	55
20 Jan 2023	2023-01-20 17:15:01.3800	2023-01-20 23:06:55.8492	MMS-1	5.865	41
31 Jan 2023	2023-01-31 13:49:57.0000	2023-01-31 18:57:58.5000	MMS-1	5.134	28
2 Feb 2023	2023-02-02 08:26:06.0000	2023-02-02 17:14:55.5000	MMS-1	8.814	69
6 Feb 2023	2023-02-06 00:00:04.5000	2023-02-06 09:40:57.0000	MMS-1	9.681	58
9 Feb 2023	2023-02-09 13:47:01.5000	2023-02-09 21:52:57.0000	MMS-1	8.099	65
20 Feb 2023	2023-02-20 03:30:00.0000	2023-02-20 08:57:58.5000	MMS-1	5.466	53
2 Mar 2023	2023-03-02 14:27:00.0000	2023-03-02 19:55:57.0000	MMS-1	5.482	57

Table A.3: Observations intervals across 260 hours of simultaneous measurements from THEMIS and MMS probes in the magnetosheath and solar wind.

		Start	End	MSH Probe(s)	SW Probe(s)	# Hours
13 May 2008		2008-05-13 00:05:12.0000	2008-05-13 11:59:57.0000	THM-C	THM-B	11.912
16-17 May 2008		2008-05-16 20:00:39.0000	2008-05-17 09:59:57.0000	THM-C	THM-B	13.988
22 May 2008		2008-05-22 12:02:31.4450	2008-05-22 21:59:56.6398	THM-C	THM-B	9.957
28-29 May 2008		2008-05-28 12:05:27.8539	2008-05-29 05:59:57.5998	THM-C	THM-B	17.908
1-2 Jun 2008		2008-06-01 08:03:03.5541	2008-06-02 03:59:58.6605	THM-C	THM-C	19.949
31 May 2009		2009-05-31 02:01:56.8480	2009-05-31 20:59:57.5310	THM-C	THM-B	18.967
4 Jun 2009		2009-06-04 02:01:24.1835	2009-06-04 22:59:58.5685	THM-C	THM-B	20.976
8 Jun 2009		2009-06-08 02:02:19.8000	2009-06-08 21:59:58.1000	THM-C	THM-B	19.961
10 Jun 2009		2009-06-10 02:02:57.7022	2009-06-10 15:59:57.1216	THM-C	THM-B	13.950
12 Jun 2009		2009-06-12 00:06:08.0568	2009-06-12 23:59:58.3656	THM-C	THM-C	23.897
14 Jun 2009		2009-06-14 00:05:05.6731	2009-06-14 17:59:59.7295	THM-C	THM-B	17.915
16 Jun 2009		2009-06-16 00:06:11.0000	2009-06-16 23:59:58.4000	THM-C	THM-B	23.896
19-20 Jun 2009		2009-06-19 22:00:46.1956	2009-06-20 23:59:57.1872	THM-C	THM-B	25.986
13 Sep 2018		2018-09-13 18:24:34.2000	2018-09-13 21:59:58.2000	THM-E	THM-B	3.590
14-15 Sep 2018		2018-09-14 19:24:09.4020	2018-09-15 03:59:57.3575	THM-E	THM-B	8.596
5 Jan 2022		2022-01-05 00:06:17.9000	2022-01-05 05:59:55.2000	THM-A, MMS-1	THM-B	5.894
6 Jan 2022		2022-01-06 00:06:35.1000	2022-01-06 05:59:55.2000	THM-A	THM-B, MMS-1	5.889
7 Jan 2022		2022-01-07 06:00:08.1000	2022-01-07 11:59:54.8000	THM-A	THM-B, MMS-1	5.996

**Appendix B: Flow chart of the GS-based automated
detection algorithm**

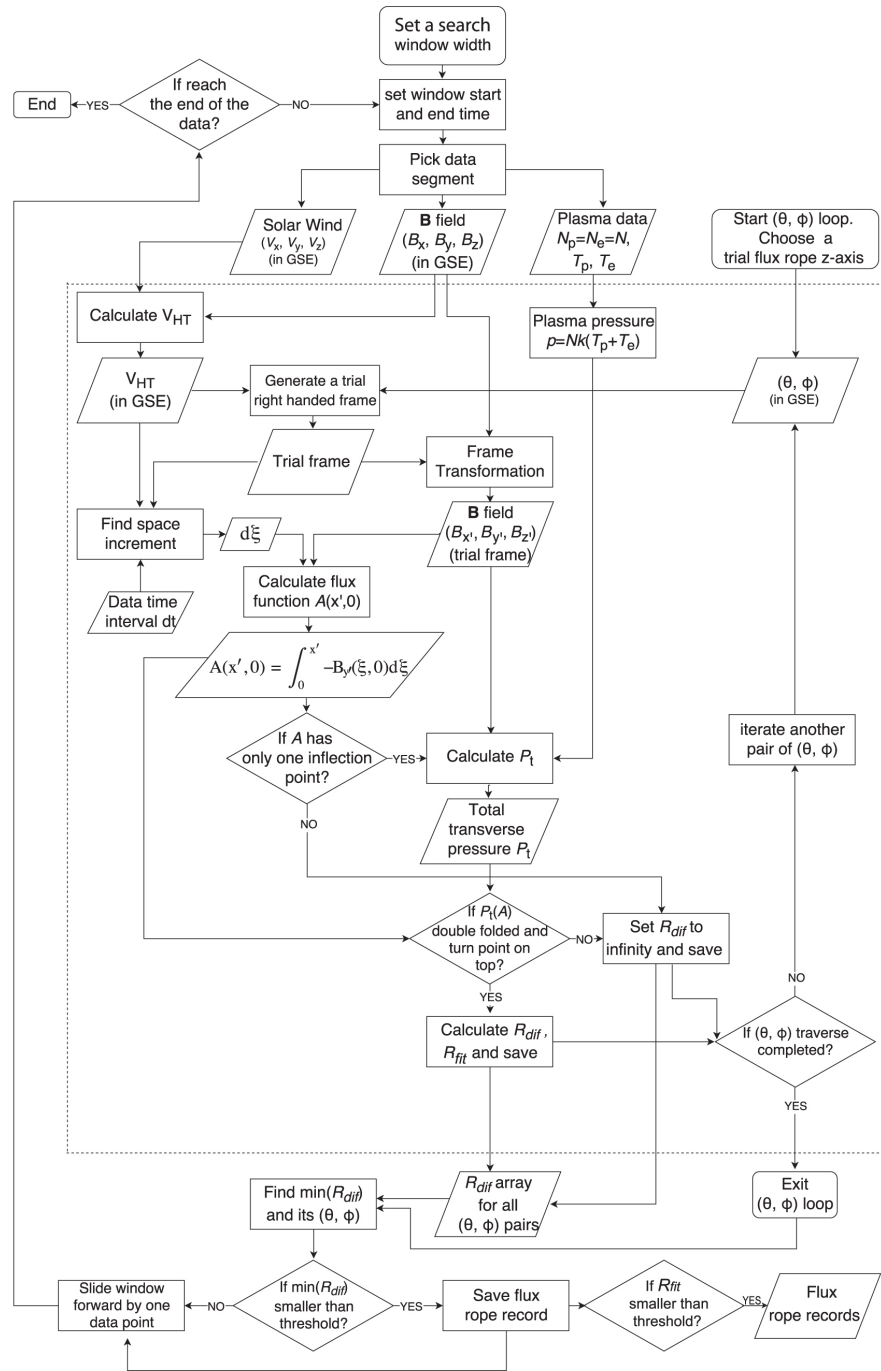


Figure B.1: Flowchart schematic of the automated detection algorithm of small-scale magnetic flux ropes, as implemented by Hu et al. (2018) and Zheng and Hu (2018).

Appendix C: Supplemental results

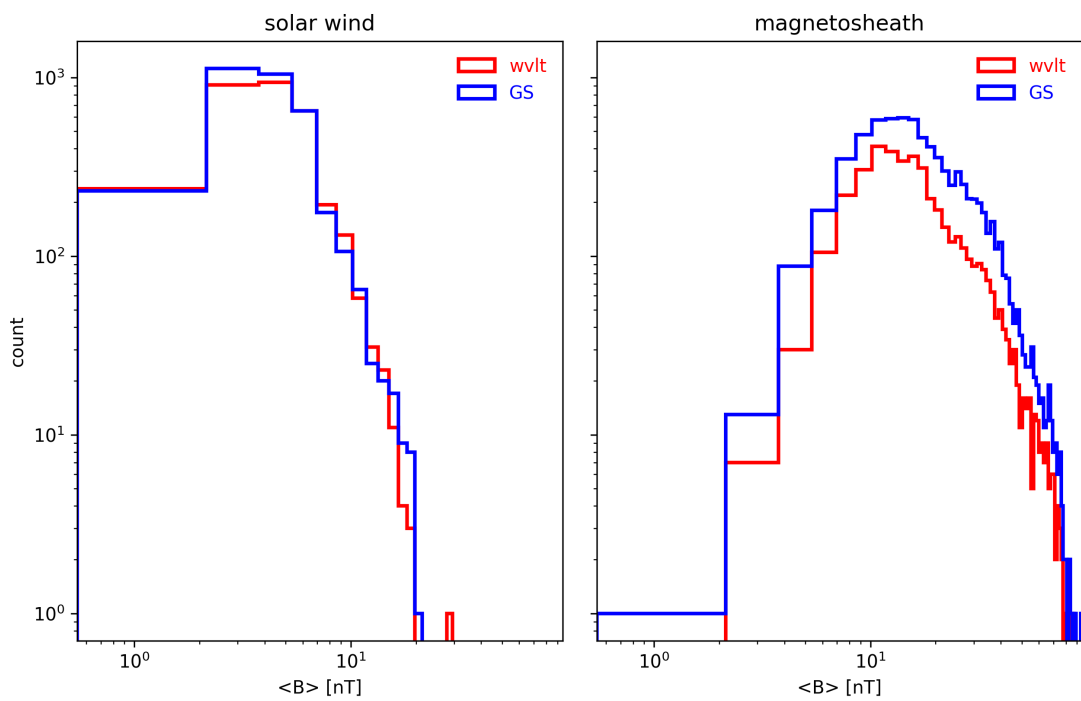


Figure C.1: Same as Figure 5.1 but for magnetic field distributions of identified events

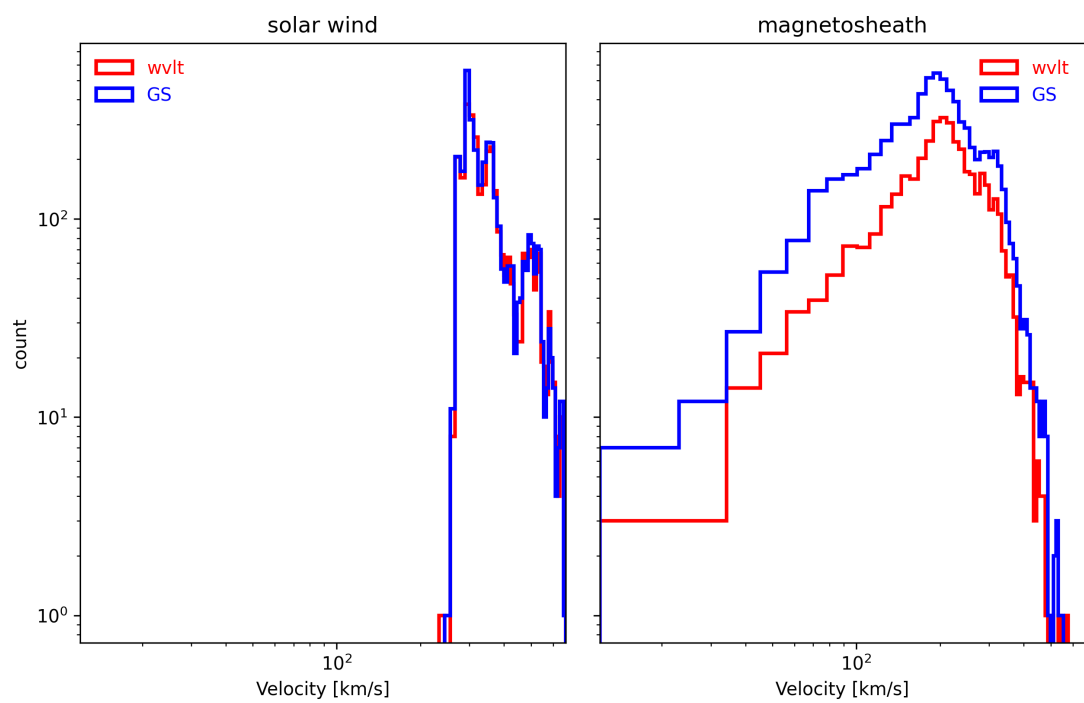


Figure C.2: Same as Figure 5.1 but for velocity distributions of identified events

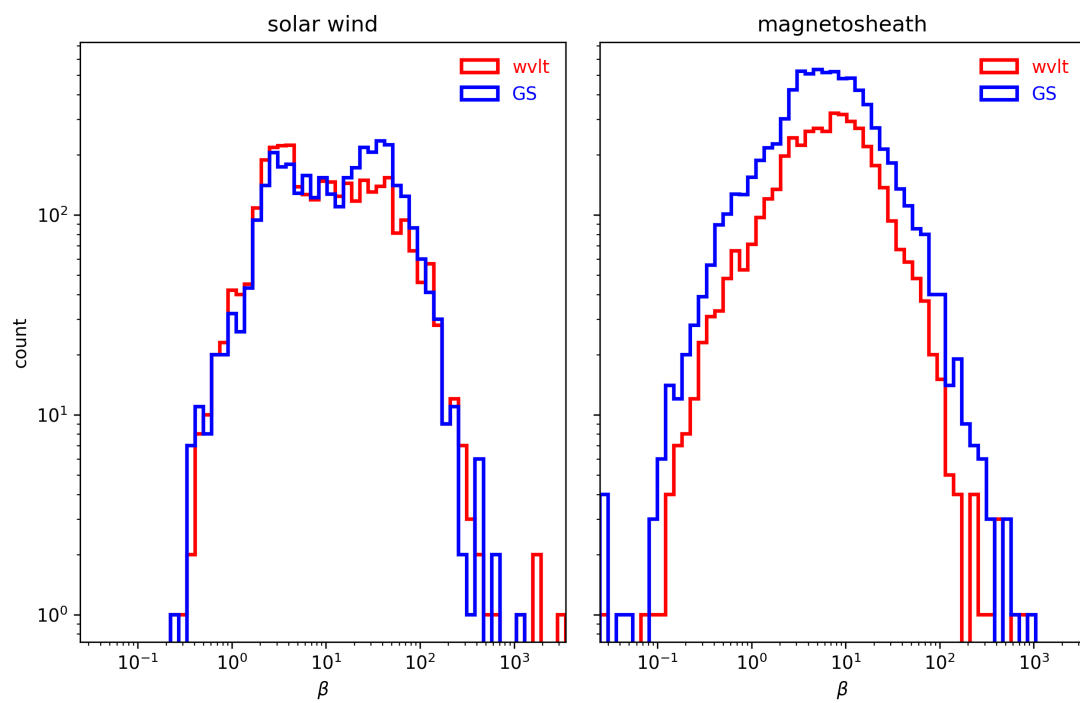


Figure C.3: Same as Figure 5.1 but for plasma β distributions of identified events

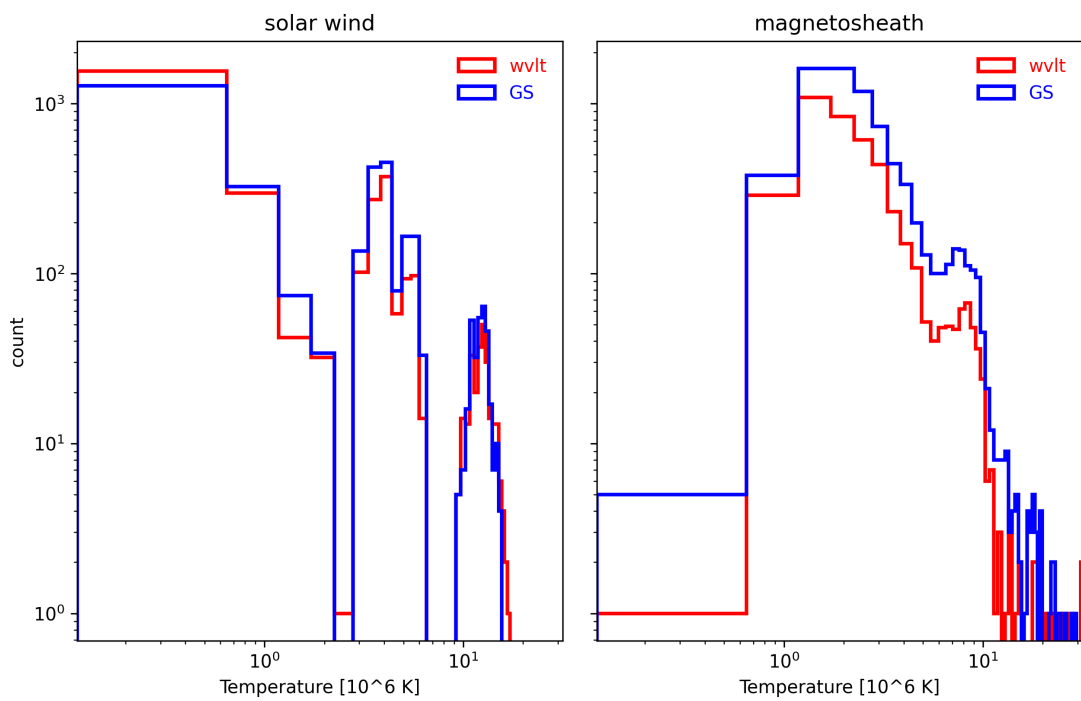


Figure C.4: Same as Figure 5.1 but for temperature distributions of identified events